Cell type-specific barcoding reveals the projectional architecture of the mouse midbrain dopaminergic system

Hyopil Kim[1], Cheng Xu[1], Craig Washington[1], Maggie Lowman[1], Justus M. Kebschull[1,2,3,4,5*]
[1]Department of Biomedical Engineering, Johns Hopkins University, Baltimore, MD 21205, USA
[2]Kavli Neuroscience Discovery Institute, Johns Hopkins University, Baltimore, MD 21205, USA
[3]Department of Neuroscience, Johns Hopkins University, Baltimore, MD 21205, USA
[4]Center for Functional Anatomy and Evolution, Johns Hopkins University, Baltimore, MD 21205, USA
[5]Lead contact
*Correspondence: kebschull@jhu.edu

HIGHLIGHTS

- We develop POINTseq, which uses pseudotyped Sindbis virus and cell type-specific expression of a viral receptor for cell type-specific barcoding.
- POINTseq enables massively multiplexed single-cell projection mapping of cell types of interest.
- We map the brain-wide projections of 3,813 individual VTA and SNc dopaminergic neurons.
- VTA and SNc dopaminergic neurons form over 30 connectomic cell types.
- Projections organize into stereotyped motifs that may mediate parallel dopamine signalling.

ABSTRACT

Brain-wide neural circuits are formed by the diverse axonal branching patterns of many individual neurons. Here we introduce POINTseq (projections of interest by sequencing), a high-throughput and user-friendly barcoded connectomics method that uses cell type specific barcoding and sequencing to rapidly map single-cell projections of a cell type of interest for thousands of neurons per animal. POINTseq leverages pseudotyping of Sindbis virus and a specific alphavirus-cellular receptor pair to make Sindbis infections cell type specific. It thus integrates MAPseq-style high-throughput barcoded projection mapping with the established viral-genetic neural circuit analysis toolbox. We validated POINTseq by mapping genetically and projection-defined cell populations in the mouse motor cortex. We then applied POINTseq to midbrain dopaminergic neurons and reconstructed the brain-wide single-cell projections of 3,813 dopaminergic neurons in ventral tegmental area (VTA) and substantia nigra pars compacta (SNc). We define over 30 connectomic cell types, vastly exceeding the known diversity of dopaminergic cell types, and identify stereotyped projection motifs that may mediate parallel dopamine signaling. This data constitutes the anatomical substrate on which the diverse functions of dopamine in the brain are built.

INTRODUCTION

Distant brain regions communicate and collaborate through long range axonal projections to perform computations.[1–4] Axons of individual neurons often branch to innervate several and sometimes dozens

of downstream brain regions.[5,6] As all the target regions innervated by one neuron, to a first approximation, receive highly correlated signals, groups of neurons that have similar projection patterns naturally define the anatomical output pathways of a source region and can be considered connectomic cell types. Defining these output pathways, understanding how they intersect with other cellular modalities, and how they function in behavior has been a central goal in systems neuroscience.[3,7,8]

Retrograde tracing offers an efficient approach for defining such output pathways.[9–16] However, the definition of output pathways by retrograde tracing is limited, as it implicitly assumes that the target region injected with the retrograde tracer is innervated by a homogeneous population of neurons. It also does not capture the brain-wide collateralization patterns or projection strength of individual neurons (Figure 1A). Although collateralization information can be partially revealed using additional retrograde tracers[14,16–18] or by combining retrograde tracing with bulk anterograde mapping to visualize brain-wide collateralization patterns[13,15,19], the ground truth anatomical structure remains unknown.[5,20]

The gold standard method for defining connectomic cell types is brain-wide anterograde single-neuron projection mapping, which does not average over individual neurons and measures projection strength. As a result, it is guaranteed to reveal all output pathways of a brain region and does not suffer the limitations of retrograde approaches. Such tracing, however, is traditionally very time intensive[21,22] limiting the number of reconstructed cells[21,22] and therefore the statistical power in defining connectomic cell types[23]. Recent technological developments in volumetric imaging such as fMOST[24,25], 2-photon serial tomography[26,27], and expansion assisted light-sheet microscopy[28–30] have enabled more efficient brain-wide tracing, allowing the reconstruction of hundreds to thousands of single neurons. This increase in throughput, however, comes at the cost of highly specialized equipment and computational problems in handling vast amounts of imaging data and reconstructing individual cells from images. Moreover, the number of neurons traced per animal and region is generally still limited to <100 cells.[27,31]

To enable rapid anterograde single neuron tracing at scale and democratically in any laboratory, we previously developed the barcoded connectomics method MAPseq (multiplexed analysis of projections by sequencing), which offers a high-throughput, imaging-free approach for mapping brain-wide single-neuron projections.[5] In MAPseq, thousands of neurons per animal are uniquely labelled with RNA barcodes by infection with a barcoded library of Sindbis virus, a positive sense RNA virus from the alphavirus family.[32] Rapid replication of Sindbis virus genomic RNA inside each cell ensures robust expression of a single barcode per cell, a feature critical to barcoded connectomics. The barcodes are then trafficked to axon terminals, where they are detected and quantified by Illumina sequencing as proxies for axonal projection strength. By analyzing the sequencing data, thousands of single-neuron projections are reconstructed from a single animal within a week.[5,6,23,33–38]

Despite these advantages, MAPseq has a major limitation for its use in the viral-genetic dissection of neuronal circuits[9–11] (Figure 1B). As it is based on an RNA virus, genetic cell type information cannot be directly incorporated into the tracing experiments using conventional DNA-based tools such as Cre-driver mouse lines.[4,39] It is therefore impossible to restrict MAPseq tracing to a cell type of interest. MAPseq has been combined with single-cell RNAseq[40] and *in situ* sequencing[33,37] of barcoded neurons to directly bridge barcode identity and hence projections and endogenous gene expression in single neurons. However, these methods require specialized hardware and increase work time and cost per animal. This

compromises the throughput advantages of MAPseq, reduces that number of replicate animals that can feasibly be run, and has overall limited the application of these methods across laboratories. As a result of these technical limitations of all existing retrograde and anterograde tracing technologies, the output pathways and connectomic cell types of many neural systems remain poorly defined.

In particular, the output pathways of midbrain dopaminergic (DA) neurons have been challenging to decipher. In the mouse midbrain, approximately 10,000 DA neurons per hemisphere[41] are located in the ventral tegmental area (VTA) and substantia nigra pars compacta (SNc). These neurons project to many regions including the limbic system, cerebral cortex, striatum, and olfactory system to mediate critical and diverse functions including reward processing, reinforcement, aggression, and movement.[15,42–48] Classically, DA neurons have been divided into populations defined by a single projection target on using retrograde tracing[49–51]. This approach has provided a fruitful anatomical basis for functional studies, revealing, for example, that DA neurons projecting to the nucleus accumbens (NAc) or the caudate putamen (CP) preferentially respond to reward and movement, respectively.[47,52,53] However, these simple definitions can hide a lot of functionally relevant heterogeneity. Multiplexed retrograde tracing and methods that anterogradely trace the entire axonal arbor of a retrogradely defined population of neurons have demonstrated significant axonal branching of individual DA neurons and revealed additional diversity in DA output pathways[14–16,20,54]. Importantly, the discovered DA subcircuits have specific functions. For example, DA subpopulations defined by their projection to medial CP and lateral CP form subcircuits with limited overlap in their brain-wide target regions and respond differently to aversive stimuli.[14] Similarly, a subset of DA neurons selectively projects to the tail CP, with minimal projections to other regions including other parts of the CP and the globus pallidus (GP), and specifically regulates aversive learning related to threatening stimuli.[45] Additional, functionally specific DA output pathways likely exist, but are inaccessible to dissection by retrograde tracing (Figure 1A).[5,20]

In a parallel effort to dissect DA output pathways, recent studies have revealed distinct projection patterns of several genetically defined subpopulations of DA neurons, providing valuable insights and genetic handles to perturb specific populations.[44,55,56] However, these subpopulations are traced in bulk, potentially averaging heterogeneous connectomic cell types within homogenous transcriptomic types[6,7,57]. Recently, a pioneering anterograde single cell tracing study showed diverse brain-wide single-cell projections of mouse VTA DA neurons classifying them into 5 types.[22] However, only 30 DA neurons were traced in the study, which limited its statistical power to define the architecture of the DA system. Despite all these new insights, and because of the inherent limitations of the tracing technologies, the ground truth anatomical structure of the midbrain DA output pathways remains unknown.

Here, we introduce POINTseq (projections of interest by sequencing), a cell type-specific barcoded connectomics tool, that uses cell type-specific infection by a pseudotyped barcoded Sindbis virus and DNA sequencing for rapid single-cell projection mapping of cell types of interest (Figure 1C). Importantly, POINTseq readily integrates with the standard genetic neuroscience toolkit and requires no specialized equipment. We first validated POINTseq for mapping genetically and projection-defined cell populations in the mouse primary motor cortex (MOp). We then applied POINTseq to mapping the brain-wide projection of midbrain DA neurons in the VTA and SNc, where we reconstructed projections of 3,813 neurons to establish the ground truth anatomical structure of DA output pathways. We defined over 30 connectomic cell types, that agree with previously proposed DA neuron type definitions, but significantly

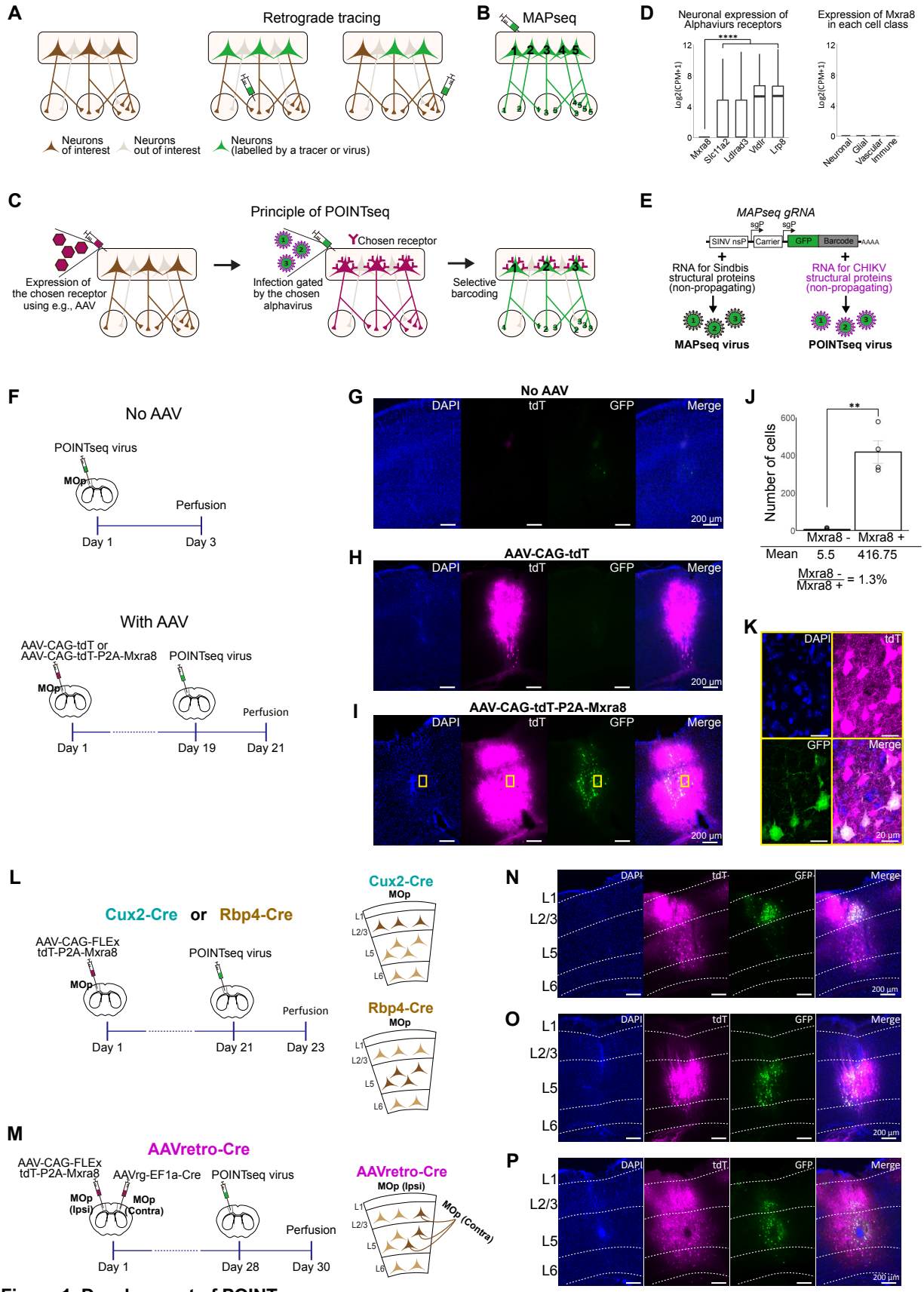

Figure 1. Development of POINTseq

(A) Neurons have diverse projection patterns (left). Although retrograde tracing can be used to label specific neurons of interest, it cannot distinguish between different connectomic cell types when their projections overlap at the injection site in terms of

different target sites (left) and different projection strength (right).
(B) MAPseq efficiently maps single-cell projections but lacks specificity for neurons of interest.
(C) The principle of POINTseq relies on the exogenous expression of a specific alphavirus receptor that is not endogenously expressed in the mouse brain. Infection is restricted to receptor-expressing cells through receptor–virus interactions, enabling cell type–specific delivery of barcodes.
(D) Expression of Mxra8 in the mouse brain compared to other known alphavirus receptors (left) and according to cell types (right). Receptors of Sindbis virus (*Slc11a2)*[156], Venezuelan equine encephalitis virus (*Ldlrad3)*[157], Semliki Forest virus (*Vldlr* and *Lrp8)*[158] were included. Counts per million mapped reads (CPM) values were adapted from Allen Brain Cell Atlas scRNAseq datasets for the entire mouse brain. The plots display a central line, box, and whiskers representing the median, interquartile range (IQR), and data points within ±1.5× IQR. The level of *Mxra8* in all cells is close to zero and significantly lower than that of other well-known neuronal genes (one-way ANOVA with Bonferroni post-hoc test $****p < 0.0001$).
(E) Generation of POINTseq virus by pseudotyping genomic RNA of Sindbis virus used in MAPseq (MAPseq gRNA) with structural proteins of CHIKV. The helper RNA encoding structural proteins of CHIKV was designed to be propagation-incompetent as previously described.[32]
(F) Three different viral injection conditions in MOp (without AAV, with AAV only expressing tdT, with AAV expressing Mxra8 with tdT) to confirm the Mxra8-dependent infection of POINTseq virus.
(G-I) POINTseq virus infections (GFP-positive) were rare without Mxra8 regardless of AAV (Mxra8-), but highly increased with Mxra8 (Mxra8+).
(J) The number of infections was significantly higher with Mxra8 indicating that approximately 98.7% of POINTseq virus infections are dependent on exogenous Mxra8 (Mxra8-: 6 mice, Mxra8+: 4 mice, Student's t test, $**p < 0.01$).
(K) High-resolution images from Figure 2G demonstrated that POINTseq virus infected cells shows typical morphology of cortical neurons.
(L, M) Schematics of experimental designs for Cux2-Cre, Rbp4-Cre, and AAVretro-Cre (left), with descriptions of the targeted neurons (right).
(N-P) Specific POINTseq virus infection of Mxra8-positive cells defined by three different Cre expression strategies.

expand on the appreciated extent of projectional diversity. Importantly, we identified a number of motifs and co-innervation patterns that are overrepresented over a null model of independent target choice, indicating that the anatomical diversity revealed by POINTseq is important for the function of the DA system.[23]

RESULTS

POINTseq enables selective barcoding of cell types of interest by cell type-specific infection

POINTseq relies on the recent discovery of alphavirus host cell receptors that interact with viral structural proteins and are sufficient and necessary for viral infection[58,59]. We reasoned that if one of these receptors is not normally expressed in the mouse brain, we could overexpress this receptor specifically in neurons of interest using, e.g., AAV and standard recombinase-based expression gating systems, rendering those cells selectively susceptible to infection by the alphavirus that uses the receptor (Figure 1C). This strategy of cell type-specific infection of RNA viruses rather than cell type-specific expression from DNA viruses is familiar to neuroscientists from the EnvA-TVA system used in monosynaptic rabies tracing[60]. To find such a receptor, we assessed the expression levels of known alphavirus receptors in the mouse brain using the Allen Brain Cell Atlas[61]. While many receptors are expressed broadly in neurons, as expected from the large host range of alphaviruses, the receptor for Chikungunya virus (CHIKV)[58], Mxra8, is not expressed in neurons or non-neuronal cells in any brain region (Figure 1D and S1A). CHIKV-Mxra8 is therefore an ideal virus-receptor pair for our cell type-specific infection strategy.

To avoid the need to redevelop barcoded projection tracing with CHIKV, we instead endeavored to pseudotype the well validated Sindbis MAPseq virus[5] with the structural proteins of CHIKV (Figure 1E). This approach keeps the viral payload and thus expression characteristics identical to MAPseq but changes the infective properties of the viral particles to those of CHIKV. Sindbis MAPseq virus is

generated by co-expressing the barcoded genomic RNA with a helper RNA encoding Sindbis structural proteins (DH-BB[5'SIN;TE12ORF]) in packaging cells[32]. Building on this protocol, we created a new helper RNA in which we swapped the Sindbis virus structural protein open reading frame for the CHIKV structural protein open reading frame (DH-BB[5'SIN;181/25ORF]). By expressing this new helper RNA with barcoded genomic RNA from Sindbis in packaging cells, we generated high titers of propagation incompetent CHIKV-pseudotyped, barcoded Sindbis virus (Figure 1E and S2). For simplicity, we will refer to this virus as POINTseq virus throughout this paper.

To validate Mxra8-dependent infection of POINTseq virus in the mouse brain, we first injected POINTseq virus by itself or following injection of a dummy AAV expressing tdTomato (AAV-CAG-tdT) in the primary motor cortex (MOp) of adult C57BL6/J mice (Figure 1F). As expected given the absence of endogenous Mxra8 expression in the mouse brain, almost no cells were infected by the GFP expressing POINTseq virus (Figures 1G and 1H). However, when we preceded POINTseq injection with the injection of an AAV helper virus expressing Mxra8 and tdTomato (AAV-CAG-tdT-P2A-Mxra8), tdTomato positive neurons were efficiently infected by POINTseq virus (Figures 1I). Infection is highly specific to target cells with 98.7% of infections mediated by exogenous Mxra8 (Figures 1J and 1K). We further tested our strategy across a range of brain regions, including the striatum, dentate gyrus, thalamus, and amygdala, and in each case found that POINTseq virus infection is dependent on exogenous Mxra8 overexpression (Figure S1B).

Finally, we tested if cell type-specific Mxra8 expression would support cell type-specific POINTseq infection. Mouse MOp contains distinct classes of long-range projection neurons in different cortical layers: intratelencephalic (IT) cells in layer 2/3 and 5, extratelencephalic (ET) cells in layer 5, and corticothalamic (CT) cells in layer 6.[6] Mouse line Cux2-Cre specifically labels layer 2/3 IT neurons whereas line Rbp4-Cre labels layer 5 IT and ET neurons.[6] We injected Cre-dependent AAV helper virus AAV-CAG-FLEx-tdT-P2A-Mxra8 into the MOp of Cux2-Cre or Rbp4-Cre mice, followed by POINTseq virus injection (Figure 1L). As expected, POINTseq virus specifically infected Mxra8-positive cells in layer 2/3 and layer 5 of Cux2-Cre and Rbp4-Cre mice, respectively (Figures 1N and 1O). To test POINTseq in projection defined cells, we injected retrograde AAV encoding Cre (AAVretro-Cre; AAVrg-EF1a-Cre) into contralateral MOp in wild type mice, and Cre-dependent Mxra8 helper virus in ipsilateral MOp (Figure 1M). After injecting POINTseq virus into ipsilateral MOp infection was observed in Mxra8-positive cells in layers 2/3 and 5, where contralaterally projecting IT (ITc) neurons are located (Figure 1P).

POINTseq accurately maps projections of targeted cortical cell types.

We next evaluated whether POINTseq produced the expected single-cell projection patterns of the targeted cell types in Cux2-Cre, Rbp4-Cre, and AAVretro-Cre experiments (Figure 2). After helper AAV injection into the respective mouse lines (N=2 animals each), we injected barcoded POINTseq virus in MOp and dissected 26 regions including regions in cortex, striatum, thalamus, midbrain, and hindbrain covering the main brain-wide projection targets of MOp neurons (Table S1 and Data S1). Barcode sequencing in these regions with a recently published optimized protocol[62] yielded the projections of 2,544 neurons from Cux2-Cre animals, 5,027 neurons from Rbp4-Cre animals, and 2,829 neurons from AAVretro-Cre animals. We then combined these POINTseq data with previously collected MAPseq data from MOp containing 11,153 neurons[62] to produce a projection matrix of 21,553 MOp neurons. Using agglomerative hierarchical clustering, we classified neurons into the three cardinal projection types (IT,

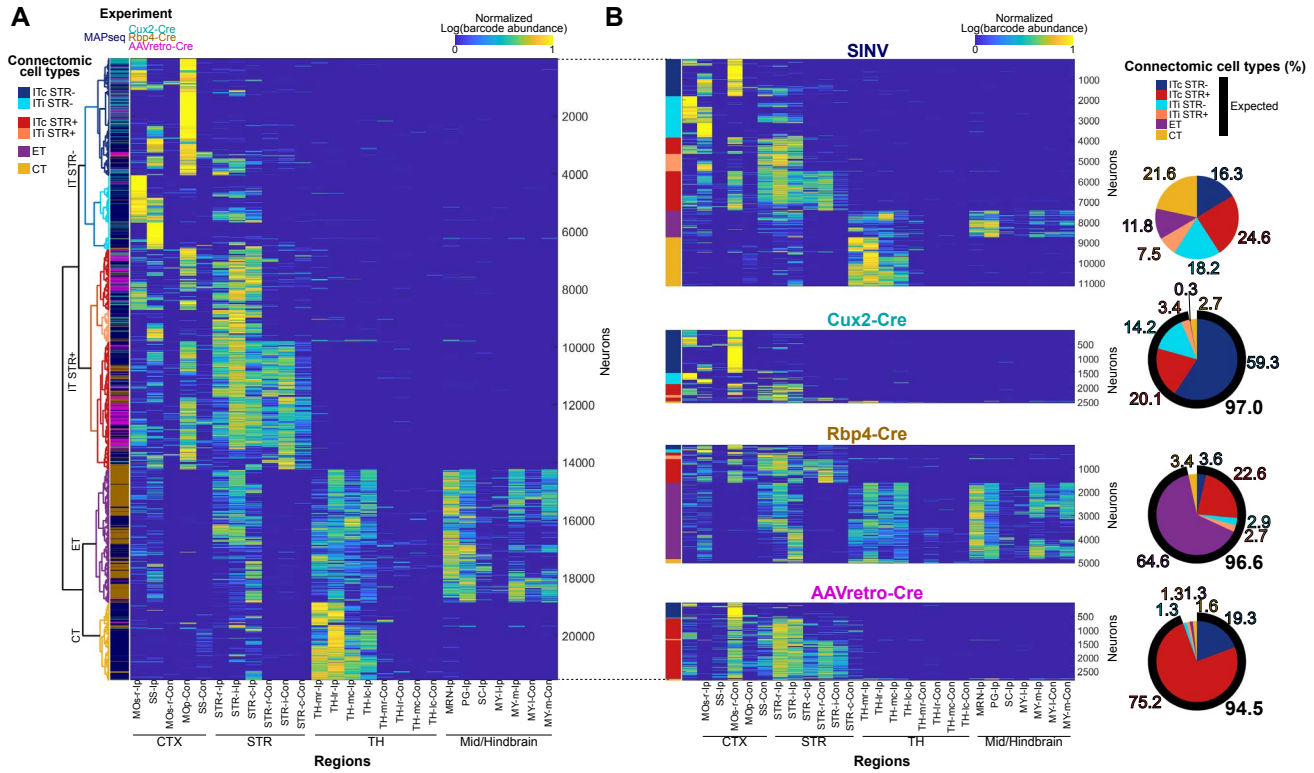

Figure 2. Validation of specific mapping of single-neuron projections by POINTseq.
(A) The combined projection matrix of MAPseq and POINTseq MOp datasets with hierarchical clustering that identified 6 previously reported connectomic types[6] (SINV: 11,153 neurons, Cux2-Cre: 2,544 neurons, Rbp4-Cre: 5,027 neurons, AAVretro-Cre: 2,829 neurons, 2 mice in each). Abbreviations for the targets are provided in Table S1. The color bar represents normalized barcode abundance, which was first normalized by the total barcode abundance across all targets within each neuron, log-transformed, and then normalized by the maximum value of the matrix.
(B) Separated projection matrices of MAPseq and POINTseq datasets from Figure 3A (left) and proportions of expected projection types in each dataset (right).

CT, ET) and further divided IT cells by whether they project to the striatum (STR+/-) or only to ipsi or also contralateral cortical regions (ITi/ITc), as before,[6] yielding a total of 6 projection types (ITc STR-, ITi STR-, ITc STR+, ITi STR+, CT, ET; Figure 2A).

As expected, neurons from the MAPseq experiment belonged to all six projection types with proportions ranging from 11.8% to 24.6%. In contrast, POINTseq neurons predominantly belonged to specific subsets of projection types according to the targeted neuronal population (Figure 2B). Specifically, in Cux2-Cre animals, which target layer 2/3 IT neurons, 97.0% of the neurons were classified as IT. In Rbp4-Cre animals, which target layer 5 IT and ET neurons, 96.6% of the neurons were classified as IT or ET. Consistent with previous findings showing that ITc STR+ neurons are more abundant than ITc STR- neurons in layer 5,[6] Rbp4-Cre mice yielded a higher proportion of ITc STR+ than ITc STR- neurons. The inverse is true for layer 2/3 IT cells in Cux2-Cre animals. In AAVretro-Cre animals, which target neurons with projections to the contralateral MOp, 94.5% of the identified neurons were contralaterally projecting ITc types. Taken together, these results validate POINTseq as a highly specific and straightforward method for mapping single-neuron projections in defined cell populations combined with common Cre-dependent strategies.

POINTseq reveals the architecture of the midbrain dopaminergic system

DA neurons in the midbrain regions VTA and SNc are the primary source of dopamine in the brain.[63,64]

They play vital roles in reward processing[14,42,44,47,52], aversion[14,42,44,45], aggression[46,48], and movement[47,65–67] while serving as key circuit nodes in substance use disorders[68,69], psychiatric diseases[70,71], and neurodegenerative diseases[72–75]. Modulating these many functions, midbrain DA neurons project broadly across the brain. Recent single-cell transcriptomic and bulk anatomical studies have revealed large heterogeneity among dopaminergic neurons that are reflected in different dopaminergic functions[43,55,65,76]. How these distinct functional circuits are formed from different populations of branching DA neurons and what subcircuits target the same target regions, however, remains poorly understood.

To address this gap, we set out to map the brain-wide single cell projections of midbrain DA neurons. DA and non-DA cells are intermingled in the VTA and SNc,[77] preventing the use of MAPseq to map DA neurons only. We therefore applied POINTseq in the DA specific Cre driver mouse line DAT-Cre. We injected Cre-dependent Mxra8 helper AAV into the VTA and SNc of DAT-Cre mice, followed by barcoded POINTseq virus (Figure 3A). As expected, POINTseq virus specifically infected tdT- and TH-positive cells in the VTA and SNc (Figure 3B and S3).

In three animals, we then dissected the two injected source regions VTA and SNc, and a total of 81 target regions ipsi and contralateral to the injection site. These regions include all major targets of VTA and SNc DA neurons, including medial prefrontal cortex (mPFC), nucleus accumbens (NAc), lateral septal nucleus (LS), olfactory tubercle (OT), ventral pallidum (VP), globus pallidus (GP), caudate putamen (CP), and lateral and basolateral amygdala (AMY), as well as regions such as olfactory bulb (OB), entorhinal cortex (EC) and lateral habenula (LHb) (Figure 3C, Table S1, and Data S1).[15,22,46,54,78–82]

Accounting for the distinct bulk projections and functional differences between subregions of NAc,[15,44,55,79,83] we further subdivided NAc into NAc lateral core (NAcLatC), NAc medial core (NAcMedC), NAc lateral shell (NAcLatS), NAc medial shell (NAcMedS), and posterior NAc (NAc-p). Similarly, based on the distinct bulk projections and functional roles of VTA/SNc DA neurons[14,15,47,54,55,83] and distinct cortical inputs in the CP[84–86], we divided the CP into four subdomains: lateral CP (LatCP), dorsomedial CP (dMedCP), ventromedial CP (vMedCP), and CP tail (CPt). We further split these domains across the rostral-caudal axis where appropriate [CPr(rostral), CPi(intermediate), and CPc(caudal)], resulting in the following 9 dissected CP subregions: LatCPr, LatCPi, LatCPc, dMedCPr, dMedCPi, dMedCPc, vMedCPr, vMedCPi, and CPt. Each subregion is further segmented from rostral to caudal with 300 μm resolution as indicated by alphabetical labeling (e.g. LatCPc-a). To ensure maximum accuracy in the dissection, we optimized tissue handling and staining[34,36], resulting in a protocol that uses laser capture microdissection of Nissl stained brain sections comparable in quality to that achieved with conventional Nissl staining (Figure 3C). We then sequenced barcodes in the dissected regions[62], and reconstructed projection matrices as done previously[5,62]. Importantly, we assigned each barcoded neuron to reside either in the VTA or SNc based on barcode abundance[36] (see STAR methods) and thus map VTA and SNc neurons in parallel in the same animal.

Midbrain dopaminergic neurons are diverse and form many connectomic cell types

Our experiments yielded a total of 3,813 high quality DA neurons, with 3,563 located in the VTA and 250 in the SNc (Figure 3D). The comparatively lower yield of SNc vs VTA neurons is likely due to imperfect injection targeting of the SNc (Figure S3A). DA neurons branch widely, with 82% of neurons innervating

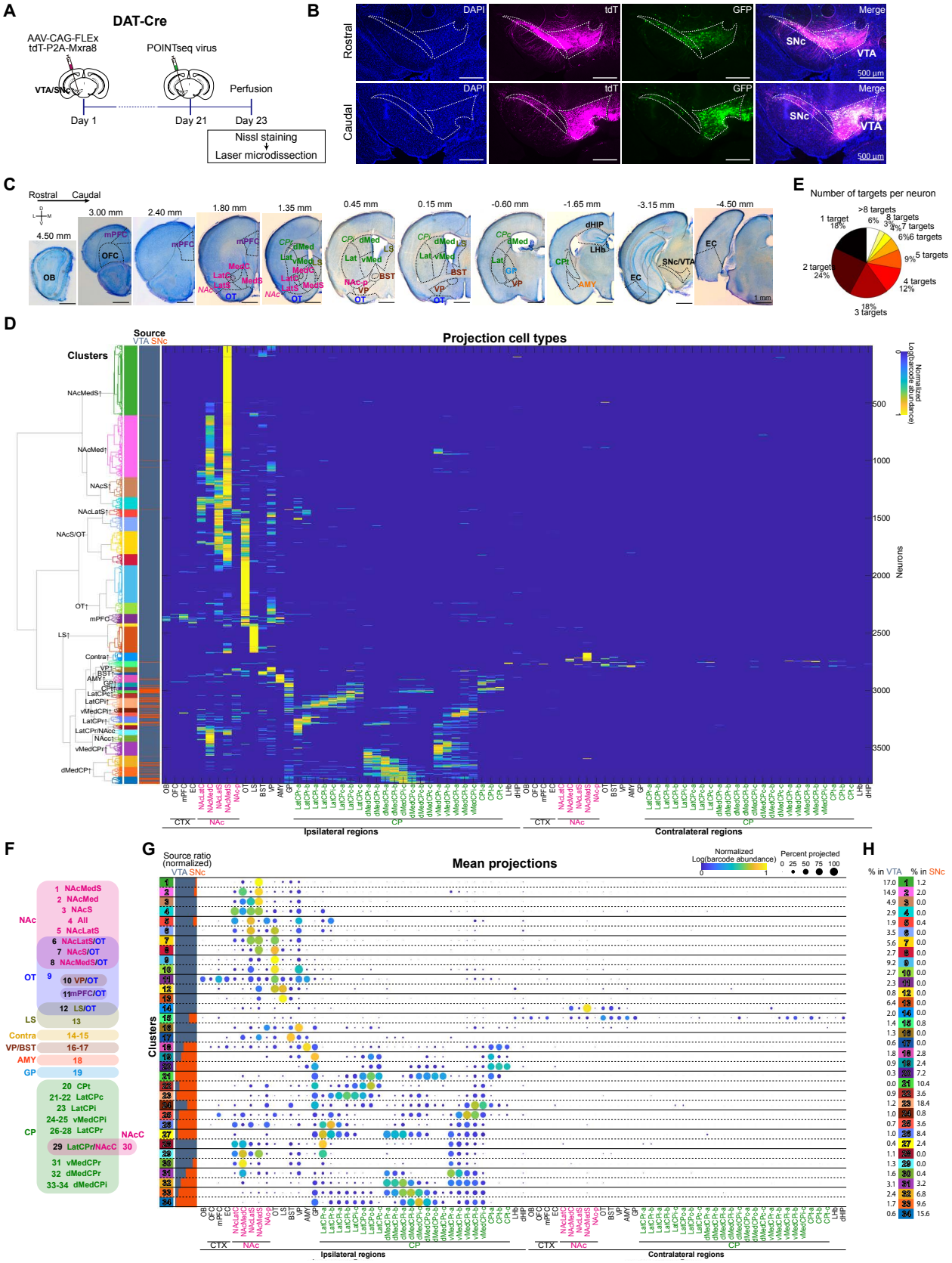

Figure 3. POINTseq in DAT-Cre mice provides a comprehensive classification of VTA and SNc dopaminergic output pathways

(A) Schematic of the experimental design for applying POINTseq to map DA neurons in VTA and SNc, involving DAT-Cre mice,

Nissl staining, and laser capture microdissection.
(B) Confirmation of the specific infection of POINTseq virus in DAT-cre+ cells in the VTA and SNc.
(C) Representative images of target regions from Nissl-stained coronal sections for laser capture microdissection along the rostral-caudal axis. The regions were determined based on Allen Brain reference atlas and previous literature.[15,55,85,86]
(D) Projection matrix reconstructed from POINTseq data (3,813 neurons from 3 mice; 3,563 VTA neurons and 250 SNc neurons; 519, 362, and 2,932 neurons per mouse). Hierarchical clustering identified 34 clusters, each characterized by distinct primary projection targets. Target region abbreviations are listed in Table S2. The color bar represents normalized barcode abundance, which was first normalized by the total barcode abundance across all targets within each neuron, log-transformed, and then normalized by the maximum barcode abundance value of the matrix.
(E) Proportion of the number of targets per neuron.
(F, G) Characterization of each cluster by primary projection targets (F) and a dot plot showing mean projection patterns for each type (G). Source ratios were normalized to the total number of traced VTA and SNc neurons.
(H) Percentage of VTA and SNc neurons in each cluster.

more than 1 and up to 17 regions (Figure 3E). To understand the overall structure of the DA neuron projections, we performed agglomerative hierarchical clustering of the dataset (see STAR methods). Cell types, including connectomic types, are hierarchically organized, with different clustering resolutions providing different insights into the data structure[57,87]. Therefore, we first chose a coarse and a finer clustering resolution based on the Silhouette criterion (Figure S4A), yielding 6 and 25 clusters respectively. While both clustering resolutions yielded stable clusters[33,88] (Figures S4B-S4E), the lower resolution averaged over a lot of heterogeneity at the single neuron level (Figures S4H and S4I). In contrast, the 25-cluster resolution yielded a more reasonable result, preserving clearly distinct projection architectures (Figures S4J and S4K). However, on closer inspection, even at this resolution, previously described distinct DA projection populations were not separated. We therefore increased our clustering resolution until the clustering results respected described divisions of DA neurons[14,15,44–46,54,55,79,83,89,90], such as preferentially CPt-projecting neurons with low projections to GP. At this resolution, we identified 34 clusters of DA neurons (Figures 3D and 3F) that appeared to largely reflect the diversity of DA connectomic cell types, and had comparably high Silhouette score and cluster stability as the 25 cluster resolution (Figures S4A, S4F, and S4G). Interestingly, both 25 and 34 clusters far exceed the number of known molecular DA neuron subtypes.[43,76]

96.7% of DA neurons project predominantly ipsilaterally, consistent with previous reports[22,91], and form 32 out of the 34 total clusters. These clusters can be roughly grouped by their strongest projection targets (Figure 3F and 3G). Several clusters preferentially target NAc (clusters 1–8, 30), OT (clusters 6–12), and CP (clusters 20–29, 31–34), while other regions are a primary target for only one or two clusters, such as mPFC (cluster 11), LS (clusters 12–13), VP (cluster 16), BST (cluster 17), AMY (cluster 18), and GP (cluster 19). Interestingly, whereas many clusters display some innervation of NAc, clusters that have their strongest projects in LS, GP, CPt, or dMedCP (clusters 13, 19, 20, 32–34) rarely project to NAc. CP-projecting neurons show preferences for different CP subregions and positions along the rostral-caudal axis, reflecting the functional organization of this region. Notably, cluster 11 neurons uniquely project to cortical regions with substantial projections to multiple regions including OT, VP, and AMY, presenting hub-like neurons that project to cortical and subcortical regions in parallel. Only 3.3% of all traced neurons primarily project to contralateral regions consistent with previous reports of weak contralateral DA projections[22,92]. Contralaterally projecting neurons form 2 clusters (clusters 14 and 15), with cluster 14 preferentially projecting to the contralateral NAcMedS.

Molecular DA cell types are distributed continuously but spatially biased across the VTA and SNc.[43,76] We

therefore investigated the contribution of VTA and SNc to our connectomic clusters and observed big differences in projection patterns between VTA and SNc neurons (Figure 3G, 3H, and S5). For example, 92.4% of SNc neurons belong to clusters preferentially projecting to the GP/CP (clusters 19–28, 31–34), whereas only 15.3% of VTA neurons belong to these clusters. In contrast, 56.3% of VTA neurons belong to clusters that have substantial projections to NAc (clusters 1-8, 29, 30), whereas only 4.0% of SNc neurons belong to these clusters. Consistent with previous reports, we find that VTA DA neurons tend to project to rostral and ventromedial areas of CP while SNc DA neurons tend to project across all CP areas.[47,55,70,93] SNc neurons are abundant in all CP-projecting clusters (clusters 20-28, 31-34), except for cluster 28 which preferentially projects to LatCPr-a. In contrast, VTA neurons are abundant in cluster 28 and clusters preferentially projecting to vMedCPr or vMedCPi (clusters 24, 31).

Taken together, our clustering results align well with reported bulk projection patterns of DA neurons, but add important granularity. We find that most previously investigated projection-defined populations likely consist of multiple connectomic cell types (Figure S6), suggesting so far unappreciated additional functional specificity of DA neuronal types. For example, while we identify previously reported distinct populations that project to the NAcLatS or NAcC and to the CP,[79] we further split each group into multiple clusters based on their projection patterns to other regions: NAcLatS- or NAcC-projecting neurons divide into clusters 2-4, 6, and 29, and CP-projecting neurons split across clusters 18-27, 32-34. Similarly, population previously defined by its projection to NAcMed and collateralizing the NAcC, MedCP, VP, and LS,[15] can be further separated into multiple populations such as clusters 1, 2, 8, and 12, depending on whether individual neurons preferentially project to the NAcMedS or additionally innervate other regions such as the VP, OT, and LS. Importantly, these clusters also exhibit different projection strength to NAcMedS, information which would lost in previous retrograde tracing experiments.[15]

Stereotyped co-innervation patterns by VTA dopaminergic neurons suggest functional importance of information sharing

Neurons that co-innervate different regions, to a first approximation, transduce shared signals to these target regions. Understanding the nature of such co-innervations will therefore yield important insights into information routing and shared functions of these regions. Co-innervation, or lack thereof, might be established by a simple model during develop where neurons choose their target regions statistically independently by a random draw. Alternatively, co-innervations might be hard-coded developmentally by some active process.[23] Information carried by individual neurons is shared between co-innervated regions and segregated between not co-innervated regions under either model. However, deviations from the independent-choice model suggest that sharing or not sharing information is functionally significant as energy was spent to set up stereotyped wiring patterns. Although the functions of DA signaling in individual regions have been extensively studied, the importance of shared or segregated DA signaling across regions remains poorly understood. We therefore set out to understand the statistics underlying DA neuronal projection patterns (Figure 4).

We constrained our analysis to VTA DA neurons, given the restricted projections of SNc DA neurons to GP and CP only. We also focused on a subset of target regions (mPFC, EC, NAc, OT, LS, VP, AMY, CP*: CP excluding CPt, and CPt), where DA function has been studied and which are targeted by at least 10 neurons (Figure 4A). We note that we divided CP into CP* and CPt, reflecting the specific anatomy and function of the CPt compared to the other regions.[45,54,94] While CPt-projecting neurons primarily reside in

the SNc,[45] they are also found in the VTA (Figures 3D and 3F), consistent with previous reports.[54]

To describe the frequency and relationship of co-innervations between pairs of target regions, we calculated three complementary measures: First, we calculated the conditional projection probability P(B|A) to assess the likelihood that a neuron projects to region B given that it projects to region A (Figure 4B). Second, we calculated the Dice score[95] $\frac{2N_{A\cap B}}{N_A+N_B}$ to assess the overlap between projections to the two regions (Figures 4C and 4D), where N_A denotes the number of neurons projection to region A, N_B the number of neurons projecting to region B, and $N_{A\cap B}$ the number projecting to both. The Dice score ranges from 0 to 1, where 0 indicates complete exclusivity and 1 indicates complete overlap. Finally, we introduced the rarity score $\frac{1}{2}\left(\frac{N_t}{N_A}+\frac{N_t}{N_B}\right)$ (Figures 4C and 4E; STAR Methods), where N_t is the total number of neurons. The rarity score represents the abundance of projections belonging to the co-innervated regions relative to the total neuron population. Similar and low rarity scores across regions indicate a relatively even distribution of projections, whereas diverse and high rarity scores indicate inconsistent proportions of projections to the regions. Importantly, the rarity score is equal to the inverse of the Dice score if projections to the different regions are independent. The product of the Dice score and the rarity score thus indicates whether the frequency of a given co-innervation conforms to the independent target choice model, or is over- or under-represented relative to this model (Figures 4C and 4F; STAR Methods). Results are consistent across individual animals (Figure S7).

Our analyses revealed a close association between NAc, OT, and VP, regions in which DA signaling is involved in encoding reward and reward prediction error.[16,44,52,80,96–101] Specifically, NAc is likely to be innervated by neurons that projection to OT and VP (Figure 4B). Additionally, NAc has high a high Dice score with OT and VP (Figure 4D), and these co-innervations are over-represented over what would be expected from the independent target choice model (Figure 4F).

The hub-like cell cluster 11 (Figure 3F) projects to a number of regions involved in associative and aversive learning.[45,80,81,94,96–100,102–107] Analysing the co-innervation statistics of these regions, we note the high and overrepresented co-innervation of mPFC and EC by VTA DA neurons (Figures 4D and 4F). This bifurcation matches to the reported co-dependence of mPFC and EC in associative learning[102]. If a neuron projects to the mPFC or EC, the OT, VP, and AMY are highly likely to be innervated (Figure 4B), and co-innervations of the mPFC or EC with the OT, VP, AMY, or CPt are over-represented (Figure 4F) over the random model of target choice, all indicating functionally specific DA subnetworks involving cortical regions.

In addition to co-innervations that are more abundant than expected, we also observed co-innervations that are significantly less frequent than expected under the independent target choice model, indicating that distinct functions are carried out by neurons innervating these regions (Figure 4F). The co-innervation between NAc and CPt is under-represented, consistent with the observation that DA neurons projecting to the NAc are primarily located in the medial VTA, whereas those projecting to the CPt are laterally located.[54] The NAc-LS co-innervation is also under-represented, consistent with previous reports.[46] Interestingly, many other co-innervations that involve LS are also under-represented, such as LS-VP, LS-CP*, and LS-CPt (Figure 4F). In contrast, LS has over-represented co-innervations with mPFC and EC,

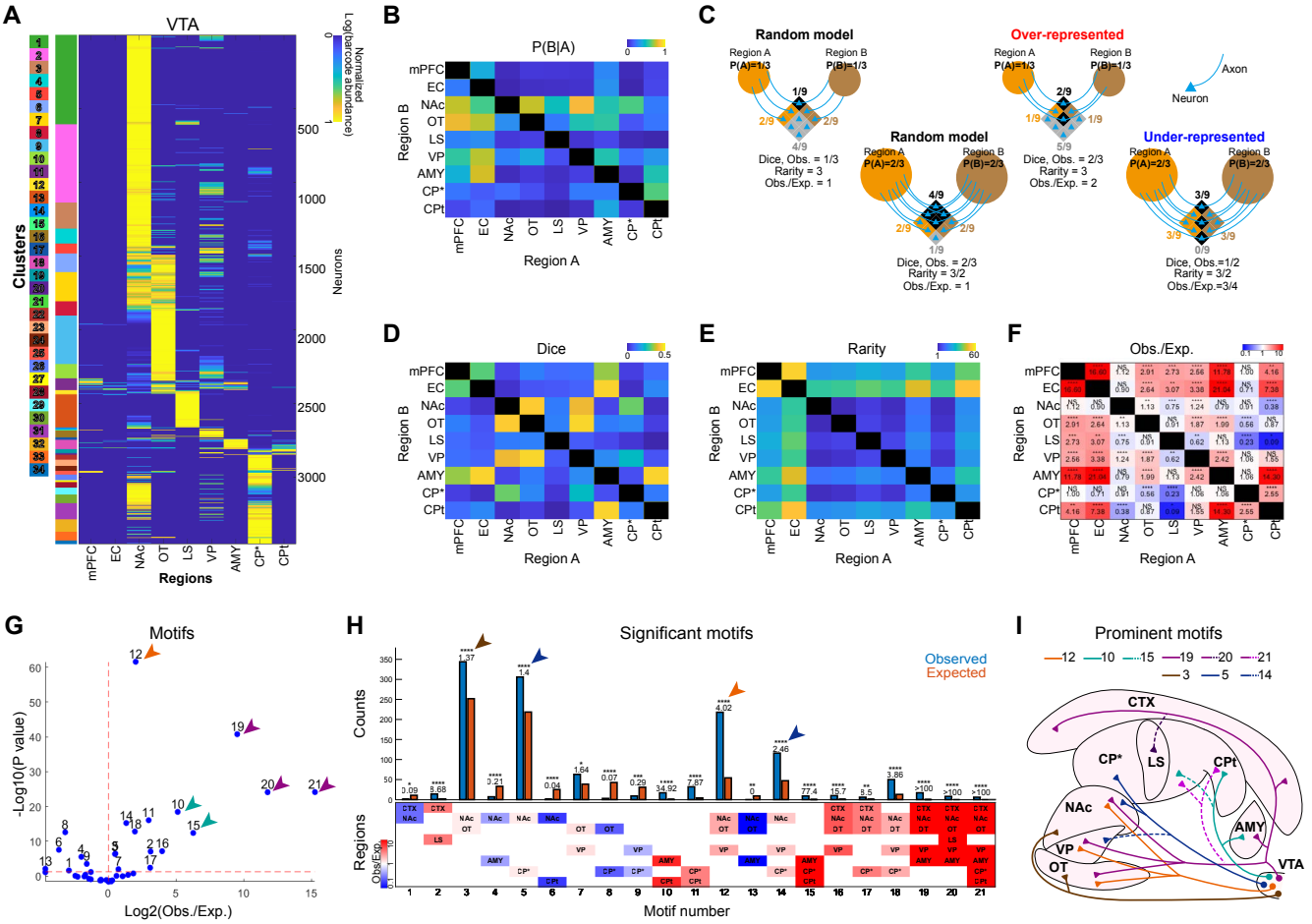

Figure 4. VTA DA neurons display stereotyped co-innervation patterns and projection motifs.

(A) Reduced projection matrix of 3,452 VTA DA neurons across 9 functionally characterized target regions, each receiving input from more than 10 neurons. Barcode abundance was re-normalized by the total barcode count across the reduced set of targets within each neuron, log-transformed, and then normalized to the maximum barcode value in the matrix.

(B) Conditional probability of projecting to region B given projections to region A.

(C–F) Co-innervation analysis. (C) Schematic examples of Dice and rarity scores and how they influence over- and under-representation relative to a random binomial model. Orange rhombus: projecting to region A, Beige rhombus: projecting to region B, Black rhombus: projecting to both regions, Gray rhombus: projecting to no regions. Observed Dice scores (D), rarity scores (E), and deviation of observed Dice scores from those estimated by the random binomial model (binomial test with Bonferroni correction, $*p < 0.05$, $**p < 0.01$, $**p < 0.001$, $****p < 0.0001$) (F).

(G–I) Motif analysis. Arrows indicate prominent motifs showing low p values, high Observed/Expected ratios, or high number of neuron counts. Volcano plot of projection motifs with more than 5 observed or estimated neurons with allocated numbers (G), and counts of significantly over- or under-represented motifs (binomial test with Bonferroni correction, $*p < 0.05$, $**p < 0.01$, $**p < 0.001$, $****p < 0.0001$) (H).

(I) Schematic representation for prominent motifs. Dashed lines in motifs 15, 14, and 20/21 indicate specific projections of each motif, while solid lines are shared with 10, 5, and 19, respectively.

suggesting potential role of shared DA signalling between LS and cortical regions which is segregated from other regions. Finally, the CP*-OT co-innervation is under-represented. As CP* receives inputs related to auditory, visual, and sensorymotor functions,[84–86], and OT deals with olfactory information, this underrepresentation suggests that DA signalling may modulate these modalities independently.

VTA dopaminergic neurons form stereotyped projection motifs

To obtain a comprehensive view of all the projections of individual DA neurons, we assessed over- and under-represented projection motifs, defined as innervation patterns across all possible combinations of target regions (Figure 4G-4I).[23] For this analysis, we grouped the mPFC and EC into “cortex” (CTX),

based on their highly similar co-innervation patterns, and only included motifs for which the observed or expected number of contributing neurons exceeded 5. We identified 21 motifs that were significantly over- or under-represented relative to the independent target choice model, providing the substrate for parallel dopaminergic signal transduction pathways across multiple regions.

NAc-OT, OT-VP, and NAc-OT-VP, motifs (motifs 3, 7, 12) are over-represented, consistent with over-represented pair-wise co-innervations between the three regions. Strikingly, motifs containing NAc and CP* with or without OT and VP (motif 5, 14, 18) are also over-represented and abundant, although co-innervations between CP* and NAc, OT, and VP is not over-represented. This indicates that innervations to NAc and CP* are specifically enriched when not involving other regions, except for OT and VP. Furthermore, motifs containing CP* and OT or VP are over-represented only when NAc is also included (motif 14, 17, 18, 21), but under-represented without NAc (motifs 8, 9), suggesting that innervation to NAc may facilitate co-innervations between OT and CP*, and between VP and CP*.

Motifs containing CTX–NAc–OT–VP–AMY (motifs 19–21) are highly over-represented, consistent with the over-represented co-innervations between pairs of CTX, OT, VP, and AMY (Figure 4F), and the high probability of NAc projection given projections to other regions (Figure 4B). While DA signaling is involved in diverse functions in each region, interestingly, a common feature across all the regions is associative learning of aversive stimuli,[80,81,96–100,102–107] in which these motifs may play critical roles. Furthermore, motif 21 contains CPt, which is also implicated in the learning of aversive or threatening stimuli.[45,94,107] Motifs 10 and 15 containing CPt and AMY without CTX, NAc, OT, and VP, suggesting more specific roles related to aversive or threatening stimuli. Additionally, the CTX-LS motif (motif 2) does not involve other regions and is over-represented, consistent with the over-represented co-innervations of the LS with cortical regions and the under-represented co-innervations with regions such as the NAc, VP, and CP*.

We also observed under-represented motifs (motifs 1, 4, 6, 8, 9, and 13). Notably, many of these motifs occur between regions of the NAc, OT, and VP and regions of the AMY, CP*, and CPt (motifs 4, 6, 8, 9, and 13), whereas over-represented motifs (motifs 12 and 15) are observed within each group separately. This suggests that overall signals may be largely separately shared within the NAc, OT, and VP group and the AMY, CP*, and CPt group. Interestingly, when the cells also project to CTX, we observe over-represented motifs between these two groups (motifs 17 and 19–21), suggesting that DA projections to the CTX may facilitate co-innervations between the NAc, OT, and VP group and the AMY, CP*, and CPt group.

To complement the analysis of binarized projection motifs, we sought to investigate the projection strengths of individual neurons in each motif (Figure S8). Intriguingly, neurons from under-represented motifs tended to strongly project to a single region, whereas neurons from over-represented motifs projected more evenly across multiple regions. This suggests that shared signal transduction within over-represented motifs is relatively balanced, while signal transduction within under-represented motifs is more biased towards single regions.

SNc dopaminergic neurons have broader projections to GP and CP than VTA neurons

CP is one of the major projection targets of midbrain DA neurons. CP projecting neurons are primarily found in the SNc but are also present in the VTA.[15,47,54,93] CP targeting DA neurons have been shown to

innervate different CP subregions and to be selectively processing rewarding stimuli, aversive stimuli, or locomotion.[14,15,47,55] However, it is unknown how many subregions individual DA neurons innervate and whether there is structure in the co-innervation patterns of different subregions. Moreover, it is unclear how these statistics differ between VTA and SNc neurons. Although SNc DA neurons are known for their wide and dense axonal arborizations compared to VTA neurons in general, their projection patterns within CP have not been compared.[108–110]

To answer these questions, we compared projection patterns of VTA and SNc DA neurons across 9 functionally distinct CP subregions (LatCPr, LatCPi, LatCPc, dMedCPr, dMedCPi, dMedCPc, vMedCPr, vMedCPi, CPt).[84–86] Given the close coordination of CP and GP in regulating movement, and that GP and CP projecting DA neurons share a similar spatial distribution in VTA and SNc[54], we also included GP in our analysis. We first selected neurons whose projections to CP and GP account for at least 10% of their total projections (Figure 5A). As expected from our clustering analysis of VTA and SNc neurons (Figures 3F and S5), VTA and SNc neurons differently contributed to clusters with distinct projection patterns. For example, VTA neurons rarely belong to cluster 21, which primarily projects to LatCPc and dMedCPc, whereas SNc neurons were rarely found in clusters 28, 29, and 30, which mainly project to LatCPr or vMedCPr. Additionally, many types of SNc neurons project to the GP, whereas VTA neurons show GP projections only in a few specific types. Overall, many VTA DA neurons preferentially project to specific subregions, particularly to LatCPr and vMedCPr, while SNc DA neurons have broader and more even projections across CP subregions.

Consistently, the number of target regions per VTA and SNc neuron is strikingly different (Figure 5B and 6C). 22% of VTA neurons vs. only 4% of SNc neurons project exclusively to 1 target, while 62% of SNc neurons vs. only 32% of VTA neurons project to more than 3 targets. The distribution of those proportions per mouse was significantly different between VTA and SNc neurons (Figure 5C). To examine if these differences are specific to certain target regions, we grouped neurons based on their maximum projection target. We found that SNc neurons project to more targets than VTA neurons when their main target project is LatCP, dMedCP, vMedCP, CPr, CPi, or CPc. The difference was biggest in neurons with maximum projection to LatCP, vMedCP, and CPr. In contrast, we observed no significant difference in target numbers for neurons that have their strongest projection to GP or CPt (Figure 5D).

As the analysis of target regions is based on binarized projection patterns only, we next assessed how their projection strengths varied across target regions (Figure S9). To do this, we calculated projection densities (projection strength divided by region size; Figure S9A). We then analyzed the standard deviation of projection densities for each neuron. SNc neurons had smaller standard deviations than VTA neurons (Figure S9B), indicating that individual SNc neurons project more evenly to GP and CP subregions. When we plotted projection densities of neurons classified by their main target region, SNc neuron projections gradually decreased around the main target, in particular in the caudal direction, whereas of VTA neurons dropped sharply, especially when the main target was in the CPr subregions (Figure S9C). Importantly, these results were not driven by the higher number of dedicated projection neurons in the VTA, as they are preserved when we required neurons to innervate at least two regions (Figure S10).

SNc dopaminergic neurons have more indiscriminately broadcasting projections than VTA

neurons in GP and CP

To understand the projection statistics of VTA and SNc neurons, we assessed the frequency of pairwise co-innervations using the Dice and rarity scores and assessed over- or under-representation relative to the independent target choice model (Figures 5E-5J). SNc neurons exhibit higher co-innervations than VTA neurons especially between GP and CP, within LatCP, and between LatCP and MedCP (Figures 5E and 5H). For example, while VTA neurons show high co-innervation of GP only with spatially close regions such as LatCPc and vMedCPi, SNc neurons exhibit high co-innervation also with more distal regions including LatCPi, dMedCPi, and dMedCPc. Similarly, SNc neurons are more likely to co-innervate LatCP and dMedCP as well as LatCP and vMedCP than VTA neurons. Within LatCP, the lower co-innervations of VTA neurons can be attributed to their preferential projections to LatCPr compared to LatCPi and LatCPc (Figure 5A). In contrast, within MedCP the co-innervation rates are comparable between SNc and VTA.

The rarity scores for SNc neurons are more similar and lower than the scores for VTA neurons, indicating that SNc neurons project more evenly to GP and CP subregions than VTA neurons (Figure 5F and 5I). In particular, CPt and other caudal areas including LatCPi, LatCPc, and dMedCPc are rarely targeted by VTA neurons, consistent with their preferential projections to the rostral regions (Figure 5A).

Intriguingly, the frequency of most co-innervations by SNc neurons is consistent with the independent target choice model, whereas the frequency of co-innervations by VTA neurons are often significantly different from what would be expected (Figure 5G and 5J), driven by both the Dice and rarity scores. Specifically, VTA neurons exhibit many over-represented co-innervations within MedCP or involving caudal regions, while co-innervations between rostral regions and caudal regions tend to be more under-represented. Notably, DA signaling in MedCP[111] and VTA DA neuron activity[112] promote compulsive reward seeking, suggesting that the strongly over-represented co-innervations of VTA DA neurons within MedCP may play an important role in this behavior.

To test whether the different projection patterns of VTA and SNc neurons in GP and CP are driven by VTA neurons projecting other third regions, we repeated our analysis focusing on neurons whose projections are confined exclusively to the GP and CP (Figure S11). Most of the neurons eliminated by this filter are VTA neurons that project to the CPr within GP/CP and NAc outside of it (Figure 3F). In the CP/GP exclusive set, the number of targets per neuron and abundance of co-innervations remained lower for VTA than SNc neurons, albeit to a lesser degree than in the previous analysis. This consistency indicates fundamental differences in projection patters of VTA and SNc neurons in GP and CP regardless of whether they innervate other regions or not (Figures S11B, C, F, G). However, the rarity score of VTA neuron co-innervations decreased for all except co-innervations involving CPt (Figure S11D, H), such that most co-innervations of VTA and SNc neurons are now explained by the independent target choice model (Figure S11E and S11I). This suggests two distinct classes of VTA projections to CP and GP, where neurons restricted to these regions co-innervate subregions by independent choosing projection targets, and neurons that project outside CP/GP as well as inside, have stereotyped co-innervation patterns.

Taken together, individual SNc neurons innervate more regions in GP and CP more evenly than VTA neurons, and their projections are well described by an independent target choice model. In contrast, VTA neurons are biased to innervate rostral regions of the CP, and co-innervations deviate from the

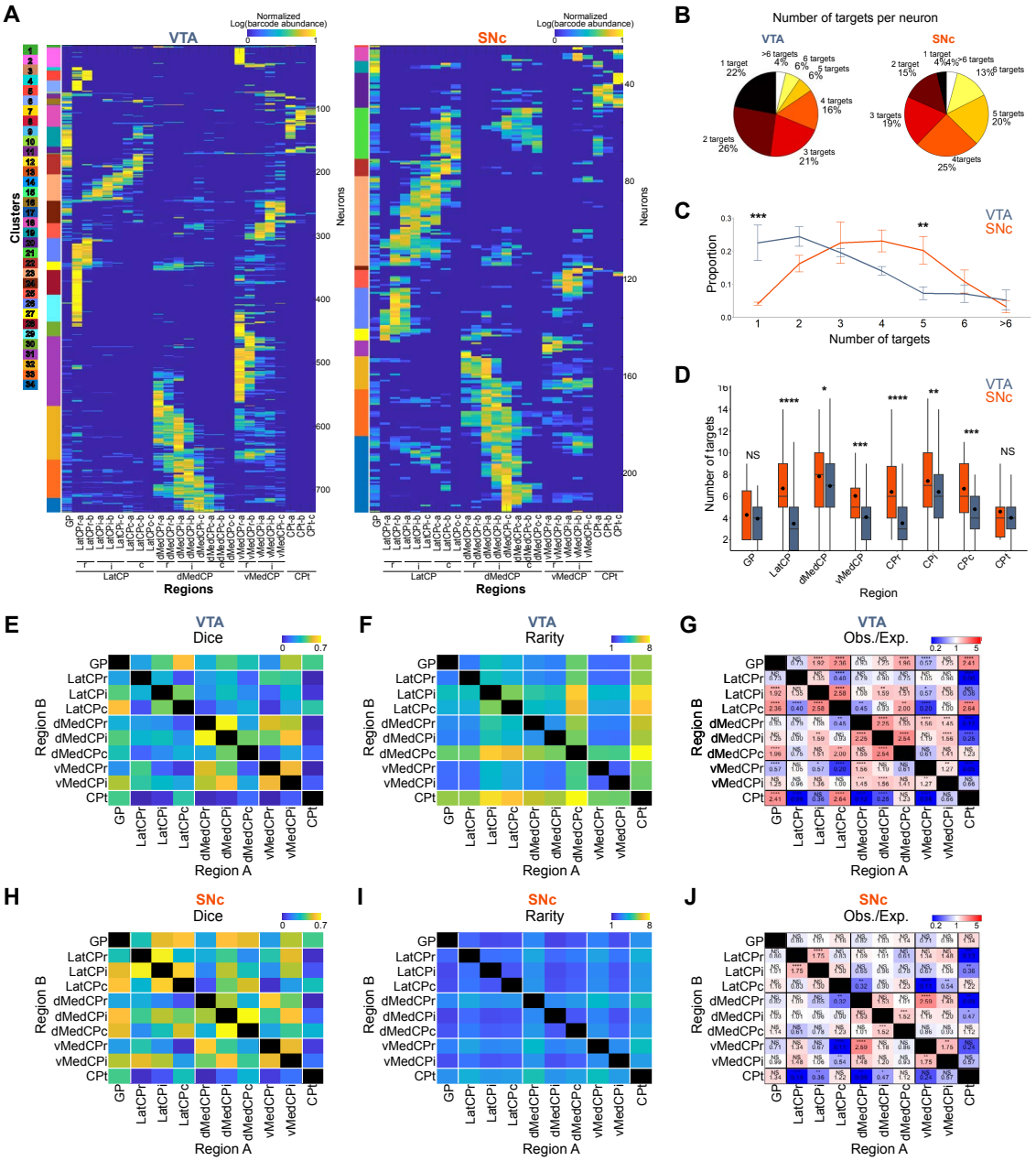

Figure 5. SNc neurons have broader, more independent projections than VTA neurons in GP and CP.
(A) GP/CP focused projection matrix of 735 VTA neurons and 239 SNc neurons that have more than 10% of their projections in GP and CP. Barcode abundance was re-normalized by the total barcode count across the reduced set of targets within each neuron, log-transformed, and then normalized to the maximum barcode value in the matrix.
(B-D) Number of targets per neuron. Total proportion of neurons according to number of targets (B), distribution of the number of targets from the three mice (two-way ANOVA, source x target number, Bonferroni post-hoc test, $**p < 0.01$, $***p < 0.001$) (C), distribution of the number of targets according to the main target region (Student's t test with Bonferroni adjustment, $**p < 0.01$, $****p < 0.0001$) (D).
(E-J) Co-innervation analysis of VTA and SNc neurons across the 10 subregions of GP and CP. Observed Dice scores of VTA and SNc neurons (E, H), rarity scores of VTA and SNc neurons (F, I), and deviation of observed Dice scores from those estimated by the random binomial model in VTA and SNc (binomial test with Bonferroni correction, $*p < 0.05$, $**p < 0.01$, $**p < 0.001$, $****p < 0.0001$, NS: non-significant.) (G, J)

independent model with over-represented co-innervations within MedCP and between regions involving caudal regions, and under-represented co-innervations between rostral and caudal regions. These results remain robust when subsampling VTA neurons to match SNc neuron numbers (Figure S12) and

similar trends are observed across individual animals (Figure S13).

Co-innervation analyses at maximum region resolution reveal the detailed architecture of shared and segregated dopaminergic signal transduction

Finally, we sought to analyse the brain-wide co-innervation patterns of VTA and SNc DA neurons for all dissected regions at maximum resolution (Figures S14 and S15), including all sub-divisions of NAc and CP, and target regions such lateral habenula (LHb) and contralateral regions. For each co-innervation we measured the Dice score and whether the frequency of these co-innervations is explained by an independent model of target choice. To ensure robustness, we only included regions targeted by at least 10 neurons, resulting in a dataset that included all 41 ipsilateral regions and 13 contralateral regions for VTA projections and 32 ipsilateral regions for SNc projections.

Ipsi- and contralateral regions were rarely co-innervated by VTA neurons, as expected from the exclusive contralaterally projecting cell clusters 14 and 15 (Figure 3F). Co-innervations among contralateral regions were high and more abundant than expected from the independent target choice model. Among ipsilateral regions, there was a tendency that co-innervations of OB, cortical regions, or AMY are over-represented over the independent model; NAc and limbic regions are highly co-innervated; and GP and CP subregions are highly co-innvervated and over-represented. Also, consistent with Figure 3F, LatCPr and vMedCPr exhibited high co-innvervations with NAc. Within NAc, co-innervations of NAcLatS-NAcLatC and NAcMedS-NAcMedC were abundant and over-represented suggesting shared signal transductions according to lateral and medial divisions. Additionally, the NAcLatS-NAcMedS Dice score was high, but not over-represented, while the NAcLatC-NAcMedC co-innervation was relatively low but over-represented, suggesting important shared signal transduction all over NAc subregions. NAc-p generally showed similar patterns to NAcLatS. Within GP and CP, SNc neuron co-innervations tended to be higher across subregions, and were less over-represented compared to VTA neurons, consistent with Figure 5.

DISCUSSION

Here we present POINTseq, which allows massively multiplexed single neuron projection mapping of genetically defined cell populations, and applied it to understand the brain-wide projectional architecture of VTA and SNc dopaminergic neurons. POINTseq is a user-friendly technology that exploits MAPseq and a specific alphavirus-cellular receptor pairing to limit Sindbis virus based barcode delivery to cells of interest. It thus introduces barcoded connectomics into the established viral-genetic neural circuit dissection toolkit[9,10]. We validated POINTseq in motor cortex using both Cre-driver mouse lines and projection-specific Cre expression. We then mapped the brain-wide projections 3,813 individual DA neurons in the VTA and SNc. We identified a large diversity of connectomic cell types that align with expected bulk projection patterns, but also highlight widespread heterogeneity within previously defined DA subpopulations. We show that co-innervation patterns are often not explained by independent target choice, suggesting functional specificity and importance of these projection motifs. Furthermore, we find that SNc neurons broadcast their information more broadly and indiscriminately across the GP and CP than VTA neurons.

Simple cell type specificity for barcoded connectomics

Barcoded connectomics methods, such as MAPseq, convert neuroanatomy into a format amenable to high-throughput sequencing yielding high multiplexing and single-cell resolution. However, cell type

specific mapping was not possible so far, limiting the uptake of these methods. Barcoded connectomics can directly bridge connectomics and transcriptomics for individual cells[33,40] thus circumventing the need for cell type specific tracing. While those combined approaches are powerful, they rely on single cell sequencing or specialized in situ sequencing equipment. As a result, these tools have a high barrier of entry and are costly on a per neuron and animal level and are relatively slow. Their use is currently restricted to expert labs, with only limited application to behavioral or disease studies that require a large number of animals to overcome inter animal variability.

We developed POINTseq to fall into a well-known middle ground to systems neuroscientists by mapping circuits with cell type specificity while maintaining the single cell resolution and mapping efficiency and requiring no specialized equipment. POINTseq specificity is fully determined by Mxra8 expression, which can be controlled using any established tools for the genetic dissection of neuronal circuits[9,10], including but not limited to Cre-driver lines[4,6,39,113] (Figures 1L, 1N, and 1O), viral delivery of Cre in the retrograde[114–116] (Figures 1M and 1P) or anterograde direction[117,118], cell type specific promoters[119,120], intersectional strategies[121–123], and activity dependent labeling[124–129]. Furthermore, as cells of interest are defined prior to barcoding in POINTseq, virally induced changes to the transcriptome do not affect specificity or decrease cellular yield.[130] Importantly, the viral genome delivered in POINTseq and MAPseq is identical, such that the abundant validation of MAPseq tracing[5,23,33–36,40,131] in various circuits and species equally and immediately applies to POINTseq. Combined with the recently improved MAPseq2 protocol[62], POINTseq empowers neuroscience labs around the world to rapidly map the projections of their neurons of interest at single cell resolution for ~$10 per target region.

Alphavirus pseudotyping to control Sindbis virus tropism

Pseudotyping of viruses is a well-established method to change viral tropism. In neuroscience, however, its application has so far primarily focused on Lenti[132,133] and Rabies virus[60,134]. Our work now expands this toolkit to propagation-incompetent Sindbis virus[32]. While POINTseq exploits the lack of CHIKV receptor expression in the mouse brain to drive cell type specific barcoding, we expect that similar strategies using CHIKV or other alphaviruses will also allow addressing difficulties in infecting cells of interest more broadly in mice and other species.

Single-cell projection mapping defines diverse and overlapping dopaminergic pathways

Previous studies demonstrate functionally diverse subpopulations of midbrain DA neurons.[14,42,44,46,47,65] These populations are generally defined by a single projection target through retrograde tracing, by bulk anterograde collateralization mapping conditioned on projections to a particular target region[14,15,135], multiplexed retrograde tracing,[15,46,79] or by genetically defined adult subtypes of DA neurons[43,55,56,65,76,136,137]. While these methods provide powerful tools to dissect the dopaminergic system, they are not guaranteed to yield pure projectional populations based on first principles: Retrograde tracing and associated bulk collateralization mapping treat all cells projecting to the region injected with retrograde label as equal. They therefore struggle especially with resolving (partially) overlapping populations[5,20]. Moreover, multiplexed retrograde tracing is limited in the number of target regions that can be assessed, due to the exponential decrease of co-labeling efficiency caused by to the independent nature of each tracer injection, overall resulting in an underestimation of collateralization and a coarse classification of connectomic types. Additionally, in retrograde tracing, target regions are determined by the (unknown) diffusion of injected tracers, resulting in difficulty resolving adjacent structures and the

blurring of projection patterns. Finally, retrograde tracing only provides binary information of projections (project or not) without quantifying projection strength, fundamentally limiting its ability to define connectomic cell types.

While genetic types are defined at single cell resolution in transcriptomic space, these molecularly homogeneous cell populations are often composed of cells with heterogeneous projection patterns[7,138]. As a result, functional measurements will reflect the aggregate activity of distinct neuronal populations, obscuring true functional segregation. Single neuron reconstructions are necessary to define projectomically homogeneous DA output pathways. In a first step, a pioneering study reconstructed the single-cell projections of 30 VTA DA neurons, revealing remarkable heterogeneity and as a result defining 5 cell classes.[22] Our POINTseq data now increase cell numbers over 100x and also include the SNc, thus allowing a comprehensive overview of the diverse single-cell projection patterns of midbrain DA neurons.

Based on our data, we define over 25-34 connectomic cell types, far exceeding the number of cannonical subdivisions of DA neurons despite a conservative clustering approach (STAR Methods). Interestingly, this large diversity aligns with a recent high resolution single-cell transcriptomic study that identified 20 clusters of DA neurons[142]. Our classification recapitulates previously reported projection patterns but suggests further heterogeneity within them (Figures 3D, 3F, and S6). For example, we identified neurons corresponding to a known population that project to CP but not NAc or mPFC.[79] However, in our data this population is further split into a total of 13 clusters (cluster 18-27, 32-34), which innervate CP with different preferential target subregions across LatCP, dMedCP, and vMedCP along with rostral-caudal axis. Similarly, a previously identified population which project to NAcMed while showing bulk projections to LS and MedCP,[15] can be divided into NAcMed and LS projecting types (clusters 11-13), and NAcMed and vMedCP projecting types (clusters 28-31), respectively. Our data also suggests heterogeneity of molecular subtypes. For example, VTA Sox6^{+} neurons that project to the NAcLatS or NAcC, but not to the NAcMedS,[55] may comprise four distinct connectomic types (clusters 5, 6, 28, and 30), while SNc Aldh1a1+ neurons that project in aggregate to CPr, LatCPi, dMedCPi, and LatCPc,[55] may consist of 5 different types (clusters 23, 24, 26, 27, 32).

Branching patterns deviate from an independent target choice model, suggesting functional importance

This large diversity of cell types seems to be encoded at least in part by an active process, as the frequencies of many co-innervations and projection motifs are only poorly explained by a model independent target choice per neuron (Figures 4 and 5). It thus stands to reason that some, if not all, projection motifs carry functional implications. For example, the abundant over-represented NAc-CP* motif might be important for parallel processing of reward and related movements. Similarly, we discovered over-represented co-innervations and motifs between NAc, OT, and VP. Given the known functions of NAc[16,44,52,101], OT[80,99,100], and VP[96–98] in the associative learning involving rewarding or aversive stimuli, and related approach or avoidance behavioural outcomes, it is tempting to speculate that these regions may collaborate on the processing of stimuli and learning through shared DA signalling.

Intriguingly we also found over-represented co-innervations and motifs of mPFC, EC, AMY, and CPt. DA signalling in mPFC, AMY, and CPt are implicated in negative valence, avoidance and aversive learning[16,42,45,94,103,139–141] and EC itself encodes negative valence[142]. DA signalling in EC is also required

for associative learning,[81] and mPFC and EC are co-dependent on each other for this process[102]. Shared DA signalling among these regions may therefore be deeply involved in responses to aversive stimuli and aversive learning. Partially overlapping with but distinct from with this network is the over-represented CTX-LS motif and under-represented co-innervations of LS with regions including NAc, VP, CP*, and CPt, suggesting that shared DA signaling between CTX and LS may serve distinct functions. Interestingly, DA signaling in LS promotes aggressive behaviors[46,48] and DA signalling in mPFC is implicated in aggression[143–146]. LS further exhibits over-represented co-innervations with other aggressive behavior-related regions such as BST[147,148] and LHb[149,150].

CP projections of VTA and SNc DA neurons are fundamentally differently organized

SNc neurons projecting to GP and CP innervate subregions more broadly and more randomly than VTA neurons (Figure 5). This suggests that SNc neurons are functionally relatively homogeneous, broadcasting their signals across the CP. In contrast, VTA neurons participate in overrepresented projection motifs and co-innervations suggesting distinct functional properties of these projectionally defined VTA subpopulations.

Limitations of the study

POINTseq mapping resolution and accuracy is determined by dissection. We maximized dissection accuracy using Nissl staining and Laser Capture Microdissection and repeated our experiments in independent mice. Nevertheless, dissection artefacts cannot be fully excluded. In particular, some dissected brain regions are continuous without clear-cut borders. Variation in dissection in these cases might result in artefactual over-represented co-innervations of the two adjacent regions. While we cannot exclude this possibility, we note that we observed many instances of non-over-represented co-innervations even between neighboring regions, such as VP-GP by VTA neurons and among CP subregions by SNc neurons (Figure S15). This suggest that our observed over-represented co-innervations or motifs are not likely to result from border artifacts. Additionally, we did not include hindbrain regions in our analysis of midbrain DA neuron projections due to the limited evidence of VTA/SNc neuron projections to the hindbrain in the existing literature. Finally, the functional implications of the discovered connectomic types and projection structures remain to be addressed in future studies.

Outlook

In conclusion, we here describe POINTseq and illustrate its utility in cell type specific single neuron tracing of the midbrain dopaminergic system. We expect that application of POINTseq to other brain regions including but not limited to the neuromodulatory centers and other broadly projecting regions will yield important insights into the organization of connectomic cell types and their intersection with genetic cell types. Further we expect its application to investigate the dynamic projection changes in specific populations of neurons after genetic, developmental, or behavioral manipulations, and in dissecting the higher order connectional architecture of the mouse brain in combination with anterograde transsynaptic tracers. Our results on the DA system provide an anatomical basis for future functional dissections of the diverse functions of DA neurons.

STAR METHODS

RESOURCE AVAILABILITY

Lead contact

Any requests for further information or resources should be directed to the lead contact, Justus M. Kebschull (kebschull@jhu.edu).

Materials availability

The new plasmids that we created in this study are available at Addgene: DH-BB[5'SIN;181/25ORF] (Addgene, #242479), pAAV-CAG-tdT-P2A-Mxra8 (Addgene, #242477), pAAV-CAG-FLEx-tdT-P2A-Mxra8 (Addgene, #242478).

Data and code availability

Region dissections of all POINTseq experiments are available in Data S1. All raw sequencing datasets are available in the NCBI Sequence Read Archive (SRA) under accession number PRJNA1285925. Analysis code and processed data files are available on GitHub (https://github.com/HyopilKim/MAPseq2-and-POINTseq). Processed MAPseq and POINTseq data are also provided as Data S2.

EXPERIMENTAL MODEL AND SUBJECT DETAILS

Animals

All mouse procedures were conducted in accordance with the Johns Hopkins University Animal Care and Use Committee (ACUC) protocols MO20M376 and MO23M346. Mice were maintained on a 12-hour light/dark cycle with ad libitum access to food and water. For POINTseq development and validation, we purchased mouse lines from the Jackson Laboratory or MMRRC centers: C57BL/6J wildtype (Jackson Laboratory, C57BL/6J, RRID:IMSR_JAX:000664), Cux2-Cre (MMRRC at University of Missouri, B6(Cg)-Cux2tm2.1(cre)Mull/Mmmh, RRID:MMRRC_032778-MU), Rbp4-Cre (MMRRC at UC Davis, B6.FVB(Cg)-Tg(Rbp4-cre)KL100Gsat/Mmucd, RRID:MMRRC_037128-UCD). The Rbp4-Cre mouse strain used for this research project, B6.FVB(Cg)-Tg(Rbp4-cre)KL100Gsat/Mmucd, RRID:MMRRC_037128-UCD, was obtained from the Mutant Mouse Resource and Research Center (MMRRC) at University of California at Davis, an NIH-funded strain repository, and was donated to the MMRRC by MMRRC at University of California, Davis. Made from the original strain (MMRRC:032115) donated by Nathaniel Heintz, Ph.D., The Rockefeller University, GENSAT and Charles Gerfen, Ph.D., National Institutes of Health, National Institute of Mental Health. We maintained these lines on a C57BL/6J background, and used male offspring for experiments. We either purchased DAT-Cre (Jackson Laboratory, B6.SJL-Slc6a3tm1.1(cre)Bkmn/J, RRID:IMSR_JAX:006660) mice from the Jackson Laboratory or obtained them from Dr. Hyungbae Kwon at Johns Hopkins University. We used both male and female mice for DA projection mapping. For all experiments, we injected AAV in 8-10 weeks old mice, and MAPseq virus or POINTseq virus when mice were 11-13 weeks old.

METHOD DETAILS

Cell culture

We used BHK and HEK293T cell lines to generate MAPseq viruses and AAV, respectively. HEK293T cells were maintained in medium consisting of 10% FBS (Gibco, 16140071 or Cytiva, SH30070.03), DMEM (Gibco, 11995073), and 1x Antibiotic-Antimycotic (Gibco, 15240096), while BHK cells were maintained in medium containing 5% FBS (Gibco, 16140071 or Cytiva, SH30070.03), MEM Alpha (Gibco, 12571063), 1x Antibiotic-Antimycotic (Gibco, 15240096), 1x MEM Vitamin (Gibco, 11120052), and 1x L-Glutamine (Gibco, A2916801). All cells were grown in a humidified incubator at 37°C with 5% CO_2 under sterile conditions.

Constructs

We obtained pAAV-CAG-tdT (Addgene, #59462) and created pAAV-CAG-tdT-P2A-Mxra8 and pAAV-CAG-FLEx-tdT-P2A-Mxra8 using a construct encoding mouse Mxra8 graciously provided by Dr. Michael S. Diamond at Washington University in St. Louis[58], using standard cloning methods. Additionally, we created a POINTseq virus production helper plasmid, DH-BB[5'SIN;181/25ORF], by replacing the open reading frame encoding the structural proteins of the Sindbis virus in the original MAPseq helper plasmid, DH-BB[5'SIN;TE12ORF] (Addgene #72309), with the CHIKV 181/25 structural protein sequence provided by Dr. Diane E. Griffin at Johns Hopkins University.

Viruses

POINTseq virus

We generated POINTseq viral libraries as previously described[5] for MAPseq virus. Briefly, we linearized a MAPseq plasmid library (diversity: 7 x 10^6) previously used[62], which was constructed based on the HZ120 construct[131], and the POINTseq helper plasmid BB[5′SIN;181/25ORF] using Pac I and Xho I, respectively, and produced genomic and helper RNAs by in vitro transcription using the mMessage mMachine SP6 kit (Invitrogen, AM1340). We co-transfected genomic and helper RNAs into BHK cells at 80–90% confluence in 10 cm dishes at a 1:1 molar ratio using Lipofectamine 2000 (Invitrogen, 11668027). After 40–44 hours, we harvested the supernatant and concentrated the virus by ultracentrifugation (160,000 × g, 2 hours). Viral titers were measured by qPCR following RNA extraction from virus and reverse transcription as previously described[5].

We produced two batches of POINTseq viruses (batch 1 and batch 2) using four 10 cm dishes of BHK cells for each batch. For batch 1, Gibco FBS (16140071) was used while for batch 2, Cytiva FBS (SH30070.03) was used for cell culture. All the other conditions were same for batch 1 and batch 2. Our previous experience indicates that a single 10cm plate of virus producing cells typically yields virus libraries with more than 1 x 10^6 diversity if not limited by the plasmid library. Both batches should therefore have a diversity > 1 x 10^6. We assessed the actual diversity and barcode distribution of batch 2 as described previously[5] but using the MAPseq2 protocol for sequencing library preparation[62]. Briefly, we extracted viral RNA from 4 x 10^8 viral particles, produced a sequencing library, and sequenced it, yielding > 2.2 × 10^6 unique barcodes (Figure S16A). We then determined whether the empirically measured barcode distribution in the library was sufficient to uniquely label the number of infected neurons per animal. Briefly, we included only barcodes with at least 3 UMI counts not to overestimate the fraction of uniquely labeled neurons , and calculated it using the following equation,[5]

$$\sum_{i=1}^{N} p_i\left(1-(1-p_i)^{k-1}\right)$$

where k is the number of infected neurons, N is the number of unique barcodes (i.e., barcode diversity), and p_i is the probability of each barcode based on the barcode distribution (Figure S16B). Importantly, even in the animal with the highest number of infected neurons (DAT3; 2,932 neurons), the uniquely labelled fraction was close to 1 (0.9968), demonstrating that our viral libraries are sufficiently diverse to support the reported POINTseq experiments.

MAPseq virus

We produced MAPseq virus as described above for POINTseq virus, but using helper construct BB[5′SIN;181/25ORF] (Addgene #72309).

Plaque assay

We conducted plaque assays as previously described.[32] Briefly, we infected 90% confluent BHK cells with MAPseq or POINTseq virus at low multiplicity of infection for 1 hour in 24-well plates. After infection, we overlaid cells with

0.4% SeaPlaque Agarose (Lonza, 50101) prepared in culture medium. 24 hours post-infection, we imaged 3 to 4 independent regions per well and manually examined the existence of plaques based on previously described shapes[32].

AAVs

We generated AAV2/1 using pAAV genomic plasmids (pAAV-CAG-tdT, pAAV-CAG-tdT-P2A-Mxra8, and pAAV-CAG-FLEx-tdT-P2A-Mxra8), adapting a previously described protocol[151]. Briefly, we transfected one of the genomic plasmids, and helper plasmids p5E18(2/1) (Addgene, #112862) and pAdDeltaF6 (Addgene, #112867) into 80% confluent HEK293T cells in 15 cm dishes using polyethylenimine (PEI) at a 1:1:1 molar ratio. 6 to 8 hours after transfection, we replaced the medium with fresh medium. 80 hours after transfection, we harvested the medium and loaded it onto iodixanol gradients (54% 4 ml, 40% 5 ml, 25% 5 ml, and 15% 5 ml) prepared using OptiPrep (Sigma, D1556). After ultracentrifugation (200,000 × g, 2 hours), we collected the 40% layer. We then concentrated the AAV using an Amicon Ultra-15 Centrifugal Filter, 100 kDa (Sigma, UFC910024). We measured viral titers by qPCR. We used primers binding to WPRE area located in our viral genome (Forward: 5' CAA AAT TTG TGA AAG ATT GAC TGG 3', Reverse: 5' AAT GAA AGC CAT ACG GGA AG 3') and used a corresponding genomic plasmid to each virus to generate a standard curve. Additionally, we purchased retrograde AAV (AAVrg-EF1a-Cre) from Addgene (Addgene, #55636-AAVrg).

Virus injections

We anesthetized mice with isoflurane (4% for induction, 1-1.5% for maintenance) and placed them in a stereotaxic frame. We then administered lidocaine (5 mg/kg) and meloxicam (2 mg/kg) subcutaneously, and made an incision in the skin on the top of the head. After performing a craniotomy at the desired location, we injected a virus via glass micropipettes using a Nanoject III (Drummond Scientific) at a rate of 1 nl/sec. For MOp, we paused the injection for 10 minutes every 100 nl to prevent leaking. After injection, we waited for 10 minutes before removing the needle and sutured the incision. Appropriate post-surgery procedures were followed according to the ACUC protocols.

To evaluate Mxra8-dependent infection of POINTseq virus in MOp, striatum, dentate gyrus, thalamus, and amygdala, we injected each region with AAV-CAG-tdT (5 x 10^{12} vg/ml, 500 nl) or AAV-CAG-tdT-P2A-Mxra8 (5 x 10^{12} vg/ml, 500 nl), followed by POINTseq virus (batch 1, 4 x 10^{11} vg/ml, 200 nl) three weeks later. In other mice, we injected MAPseq virus (4 x 10^{11} vg/ml, 200 nl) into each region as positive controls. We used the following coordinates relative to bregma. MOp, AP: +0.5 mm, ML: ±1.5 mm, DV: -0.6 mm; Striatum, AP: +0.5 mm, ML: ±1.8 mm, DV: -3.5 mm; Dentate gyrus, AP: -1.5 mm, ML: ±1.2 mm, DV: -1.9 mm; Thalamus, AP: -1.5 mm, ML: ±1.2 mm, DV: -3.5 mm; AMY (AP: -1.5 mm, ML: ±3.3 mm, DV: -4.6 mm.

To assess cell type-specific infections in Cux2-Cre and Rbp4-Cre, we injected AAV-CAG-FLEX-tdT-P2A-Mxra8 (5 x 10^{12} vg/ml, 300 nl) at 3 depths in the left MOp (AP: +0.5 mm, ML: +1.5 mm, DV: -0.3, -0.6, -1.0 mm relative to bregma). For AAVretro-Cre, we injected AAV-CAG-FLEX-tdT-P2A-Mxra8 in the same manner in left MOp, and AAVrg-EF1a-Cre (1 x 10^{12} vg/ml, 500 nl) in the right MOp (AP: +0.5 mm, ML: -1.5 mm, DV: -0.6 mm relative to bregma) of C57Bl6/J mice. 20 days (for Cux2-Cre or Rbp4-Cre) or 27 days (for AAVretro-Cre) after AAV injections, we injected POINTseq virus (batch 1, 4 x 10^{11} vg/ml, 200 nl) at 3 depths in the same locations in left MOp.

To map midbrain DA neurons in the VTA and SNc using POINTseq, we injected AAV-CAG-FLEX-tdT-P2A-Mxra8 (5 x 10^{12} vg/ml, 400 nl) at four mediolateral locations in the left hemisphere of DAT-Cre mice (AP: -2.8 mm, ML: +0.4, +0.9, +1.4, +1.8 mm, DV: -4.5 mm relative to bregma). 20 days after the AAV injection, we injected POINTseq virus (batch 1 for DAT1 and DAT2 mice, batch 2 for DAT3 mouse, 4 x 10^{11} vg/ml, 300 nl) at the same locations. We note that our SNc injections targeted a site a little below the SNc (Figure S3A), resulting in more traced VTA neurons than SNc neurons.

Tissue processing

We euthanized the mice 40-44 hours after MAPseq or POINTseq virus injections. To obtain fresh frozen brains, we extracted the fresh brain and immediately froze it on a metal plate at -80°C in OCT (Electron Microscopy Sciences). To obtain fixed brains, we perfused the mice with PBS followed by 4% paraformaldehyde (PFA), extracted the brain, and postfixed it for in 4% PFA at 4°C for 24-hour. After fixation, we stored the brains in a 30% sucrose and 200mM glycine solution prepared in PBS at 4°C for 24 hours, then froze them at -80°C in OCT. We cryosectioned the frozen brains coronally for MAPseq, POINTseq, or imaging. For imaging, we mounted 50 µm thick sections of PFA-fixed brains on slides using Fluoromount-G Mounting Medium with DAPI (Invitrogen, 00-4959-52).

For POINTseq of MOp-injected brains, we mounted 300 µm fresh frozen brain sections on slides and dissected target regions by hand as described before.[23] We added TRIzol (Invitrogen, 15596026) to the dissected samples and homogenized them using the TissueLyser III (Qiagen, 9003240).

For POINTseq of VTA/SNc-injected brains, we performed Nissl staining of 150 µm fixed brain sections on ice. Briefly, we rinsed the sections with RNase-free water (Invitrogen, 10977023) and stained them with 0.05% toluidine blue for 45 seconds, followed by another rinse in RNase-free water. We then incubated the sections in 100% EtOH for 2 minutes before rinsing them with RNase-free water. We then mounted the sections on 4 µm PEN (polyethylene naphthalate) steel frames (Leica, 11600289), pretreated with 2% gelatin to prevent detachment, for laser capture microdissection. We placed the frames in a vacuum desiccator to dry at room temperature overnight. We then dissected the desired regions using a 10x objective on a Leica LMD7 Laser capture microdissection system and collected them in 96-well plates. We observed no RNA degradation within a week of collection when slides are stored in the desiccator, and completed all dissections within 4 days. After dissection, we added 100 µl of digestion solution (50 mM Tris, 10 mM EDTA, 0.5% SDS) and 5 µl of Proteinase K (NEB, P8107S) to each well and incubated the samples at 50°C with 800 rpm shaking (USA Scientific, #8012-0000 and #8012-0018) for 15 minutes. We then incubated the samples at 80°C for an additional 15 minutes without shaking, and finally added 1ml of TRIzol to each digested sample.

Immunohistochemistry

We mounted fixed brain sections on glass slides and drew hydrophobic borders using a PAP pen (Sigma, Z672548). We then permeabilized the sections with 0.2% Triton X-100 at room temperature for 30 minutes. After permeabilization, we incubated the sections in a blocking solution (5% goat serum in PBS) at room temperature for 1 hour. Next, we applied a primary antibody, rabbit anti-TH (Sigma, T8700-1VL, 1:500), in the blocking solution and incubated at 4°C overnight. We then washed the sections three times with PBS for 5 minutes each and incubated them with a secondary antibody, goat anti-rabbit Alexa Fluor 647 (Invitrogen, A55055, 1:1000), in the blocking solution at room temperature for 1 hour. After three additional PBS washes, we mounted the samples with Fluoromount-G Mounting Medium containing DAPI (Invitrogen, 00-4959-52).

Imaging

We captured images of viral infections using a fluorescence microscope (Keyence BZ-X710) with 4x (NA = 0.20) and 10x (NA = 0.45) objectives. For imaging the plaque assay (Figure S1A), we used a 20x objective (NA = 0.45). For high magnification images in Figures 1K and S3, we used a confocal laser scanning microscope (Zeiss LSM 810) with a 40x oil-immersion objective (NA = 1.3). Within each experiment, we applied consistent imaging settings, including excitation power and exposure time.

MAPseq2 procedures

We prepared amplicon sequencing libraries using the MAPseq2 protocol[62]. Briefly, we extracted total RNA from dissected samples using TRIzol (Invitrogen, 15596026) according to manufacturer's instructions. We performed reverse transcription (RT) using MashUp Reverse Transcriptase and sample-specific primers containing unique a

molecular identifier (UMI) and a sample-specific identifier (SSI). We also added a known amount of spike-in RNA (10^5 or 10^7 molecules to the target or source samples, respectively) resembling the viral RNA but distinguishable by an 8 nt identifier (CGTCAGTC) in the barcode sequence. We then treated the samples with Exo I and RNase If immediately after RT, followed by bead clean-up. We then amplified the RT products by two rounds of PCR (PCR1 and PCR2). We used a 5x qPCR master mix prepared with 5x SYBR green I (Invitrogen, S7563), 5x AccuPrime reaction mix, 2.5mM $MgSO_4$, 5μM foward primer, 5μM reverse primer, 10% ROX Reference Dye (Invitrogen,12223012), and 25% DMSO. We monitored the amplification in real time using a LightCycler96 and stopped cycling before saturation. PCR2 primers contain sample-specific identifier pairs, i5 and i7, preventing sample cross-contaminations during sequencing. After PCR2, we gel-extracted the 219bp PCR product with the QIAquick kit (Qiagen, 28704), and verified library size and concentration using a TapeStation (Agilent, G2992AA). Sequencing was performed on the NovaSeq X Plus platform using 2x150 reads. Libraries were demultiplexed by i5/i7 index pairs, with R1 reads covering barcodes (≥32 nt) and R2 covering SSI and UMI (≥20 nt). The following sequences were used for primers.
RT primer : 5' GAC GTG TGC TCT TCC GAT CTN NNN NNN NNN NXX XXX XXX NCA CGA CGG CAA TTA GGT AGC 3'. The N_{12} indicate the random UMI and X_8 the sample specific identifier (sample specific).
PCR1 forward primer: 5' CGA GAA GCG CGA TCA CAT G 3'
PCR1 reverse primer: 5' CTG GAG TTC AGA CGT GTG CTC TTC CGA TCT 3'
PCR2 forward primer: 5' AAT GAT ACG GCG ACC ACC GAG ATC TAC ACX XXX XXX XAC ACT CTT TCC CTA CAC GAC GCT 3'. X_8 indicate the i5 sample index (sample-specific).
PCR2 reverse primer: 5' CAA GCA GAA GAC GGC ATA CGA GAT XXX XXX XXG TGA CTG GAG TTC AGA CGT GTG CTC TTC 3'. X_8 indicate the i7 sample index (sample-specific).

QUANTIFICATION AND STATISTICAL ANALYSIS

Expression of Mxra8 in the mouse brain

We downloaded scRNAseq datasets of the adult mouse whole brain from the Allen Brain Cell Atlas (https://alleninstitute.github.io/abc_atlas_access/descriptions/WMB_dataset.html, WMB-10Xv2 and WMB-10Xv3), which includes log-transformed gene expression data for 3,724,993 cells, accompanied by cell metadata such as cell identity ("cell_label") and cluster annotations ("cluster_annotation_term_label"). For analysis we selected the Division level of annotation, consisting of Pallium glutamatergic, Subpallium GABAergic, PAL-sAMY-TH-HY-MB-HB neuronal, CBX-MOB-other neuronal, Neuroglial, Vascular, and Immune. We combined the first four divisions (Pallium glutamatergic, Subpallium GABAergic, PAL-sAMY-TH-HY-MB-HB neuronal, and CBX-MOB-other neuronal) into a "Neuronal" super-group and renamed the Neuroglial division to "Glial", resulting in four major cell classes of Neuronal, Glial, Vascular, and Immune. We then assessed the mean expression of specific genes across all cells, classes or regions, using the following gene IDs: Mxra8 (ENSMUSG00000029070), Slc11a2 (ENSMUSG00000023030), Ldlrad3 (ENSMUSG00000048058), Vldlr (ENSMUSG00000024924), Lrp8 (ENSMUSG00000028613).

Quantification of Mxra8-dependent infection

To quantify Mxra8 dependent infection of the POINTseq virus, we injected mice with only POINTseq virus in MOp (Mxra8-, N=6, 3mice bilateral) or AAV-CAG-tdT-P2A-Mxra8 followed by POINTseq virus (Mxra8+, N=4, 2 mice bilateral). We captured images of all sections across the injection sites to count GFP-positive cells using imageJ (version 1.54f). We converted each image to 8 bit and applied a threshold to generate binary images of cell bodies. Then, we isolated and counted cells using the "Watershed" and "Analyze Particles" function. Only particles larger than 40 μm² were counted. In cases where cell segmentation was inaccurate, we manually counted these areas.

General sequencing data processing

Producing raw barcode matrices

To produce barcode matrices (barcodes X regions) from FASTQ sequencing files, we followed the MAPseq2 data processing pipeline as described[62]. Briefly, we stripped the 30 nt barcode and 2 nt pyrimidine anchor from Read 1 and the 8 nt SSI and a 12 nt UMI from i5/i7 demultiplexed FASTQ files, and only kept reads with the correct SSI. Since we used specific SSI, i5, and i7 for each sample, most of the demultiplexed files should contain the correct SSI, and we found that 98-99% of our reads had the correct SSI. Next, we removed the SSI, and used the remaining 44 nt sequences (barcode, anchor, UMI) to generate rank plots of each unique sequence and its read abundance using Matlab (MathWorks, R2022a). Rank plots exhibit a plateau and a tail, with the plateau being reliable and the tail being unreliable[152]. We determined minimal read thresholds for all samples to exclude non-reliable reads and quantified the abundance of each 30 nt barcode + 2 nt pyrimidine anchor by the number of different UMIs they were observed with. We then divided the sequences into two groups: viral barcodes and spike-in barcodes, based on whether they contained the spike-in specific sequence (CGTCAGTC). To correct for sequencing and PCR errors, we collapsed any 32 nt sequences within a Hamming distance of 3 or less. To do so, we constructed a connectivity matrix of all 32 nt sequences using Matlab (Mathworks) in sequence space, where connections were determined by Bowtie alignments of the barcodes[153] with up to 3 mismatches allowed. In any connected component of this matrix the most abundant sequence represented the group. Finally, we matched barcodes across samples by perfect identify and constructed a raw barcode matrix (barcode x region) as a Matlab variable, where each element represented the number of UMIs of the barcode in each region.

Producing normalized and filtered projection matrices

The following procedures were conducted using Matlab. First, we confirmed that negative controls from uninjected brains processed in parallel with the sample brain had zero counts for approximately 99.9% of barcodes. We then excluded any barcode that was not present in at least one target region with >10 UMIs to only include reliable barcodes, as false-positive barcodes with up to 8 UMIs were observed (albeit rarely) in negative control samples. To ensure we included only barcodes with well infected cell bodies, we also set a minimal UMI threshold for the source region. To determine an appropriate threshold, we plotted the proportion of number of targets per neuron as a function of UMI threshold and set the source threshold where the measure stabilizes (Figure S17A). The source threshold was 20 UMIs for MOp tracing experiments and 40 UMIs for VTA/SNc experiments. Then, we normalized the UMIs of the filtered barcodes in each region by the abundance of spike-in RNA in that region. We further normalized the resulting values for each barcode by the total of abundance of that barcode across all target regions. Finally, we log-transformed and scaled the values such that the maximal projection value of the matrix was 1.

Validation of the cell type-specific mapping of POINTseq

To evaluate the specific mapping of POINTseq, we produced projection matrices of 6 mice using POINTseq from the Cux2-Cre, Rbp4-Cre, and AAVretro-Cre experiments (Cux2-1: 728 neurons, Cux2-2: 1,816 neurons, Rbp4-1: 2,280 neurons, Rbp4-2: 2,747 neurons, Retro-1: 576 neurons, Retro-2: 2,253 neurons). We then combined them with a previous MAPseq dataset[62] of MOp neurons with the same target regions obtained from 2 mice (MAPseq-1: 7,506 neurons, MAPseq-2: 3,647 neurons), resulting in a projection matrix of 21,553 neurons and 26 targets, without batch corrections.

We performed hierarchical clustering on the combined projection matrix as done previously for cell type clustering[154] using Matlab. Specifically, we clustered barcodes through agglomerative clustering using a Euclidean distance metric and Ward's algorithm, using Matlab's "linkage" and "dendrogram" functions. To identify major clusters, we set the "maxclust" parameter of the dendrogram function to a specific number, which cuts the dendrogram at a position that yields that number of clusters. We aimed to recover 5 major projection-defined clusters previously identified in MOp: intratelencephalic ipsilateral (ITi), intratelencephalic contralateral with or without striatal projections (ITc STR− and ITc STR+), corticothalamic (CT), and extratelencephalic (ET) neurons[6]. Since the ITi group was previously not well resolved in relation to striatal projections, we further subdivided ITi into ITi STR− and ITi STR+, yielding a total of 6 connectomic types.

Mapping midbrain dopaminergic neurons using POINTseq

We first determined the source region of each neuron between VTA and SNc, leveraging the property of the Sindbis genomic RNA, which is much more abundant in the cell body of an infected neuron/in the source regions than in the axons of an infected neuron/the target regions.[36] Therefore, we defined the source ratio as the ratio of UMI counts (lower/higher) of each barcode between VTA and SNc. A source ratio of 0 means that the barcode is detected exclusively in one region, allowing unambiguous source assignment, while source ratio of 1 means equal UMI counts in both regions, making the source indeterminable. We then plotted the distribution of source ratios across barcodes and found that over 90% of neurons exhibited a source ratio below 0.1 (Figure S17B), demonstrating that most barcodes are much more abundant in one region than the other. To determine whether a threshold of a source ration <0.1 could reliably distinguish true source region from strongly innervated target regions, we conducted a simulation. We used a data from two regions in this experiment. One was the UMI counts in the true source region (the higher UMI count between VTA and SNc); the other was the UMI counts of an abundant target region that might be misread as source (the highest UMI count among all target regions other than VTA and SNc). Using these two regions, we calculated the source ration and assessed the accuracy of source determination as a function of source ratio threshold. In the simulations, a source ratio threshold of 0.1 yielded an overall accuracy of more than 96% (Figures S16C and S16D). Based on this result, we included only neurons with a source ratio less than 0.1 in our analyses and assigned them to the VTA and SNc based on their maximal barcode expression.

We then performed agglomerative hierarchical clustering as above, but collapsed “overclustered” nodes posthoc. Specifically, we estimated whether each node of dendrogram is statistically significant using SHC (Significance of Hierarchical Clustering) testing[155] developed to estimate statistical significance of agglomerative hierarchical clustering. In SHC, the null hypothesis assumes that the data points within a given node are drawn from a single Gaussian distribution. A null Gaussian model is then generated based on the mean and standard deviation of the data points of subjected node. For each node, a simulated Ward linkage value is calculated from the null model with matched sample sizes. The observed linkage value is then tested against the distribution of the simulated values. We simulated 500 times and considered $p < 0.05$ significant. To correct for multiple comparisons across the dendrogram, SHC employs a sequential testing procedure that controls the family-wise error rate (FWER). Starting from the root, if a node fails to reject the null hypothesis, its child nodes are considered non-significant. SHC testing was conducted using the R package sigclust2 (version 1.2.4).

To estimate the appropriate clustering resolution for our data, we performed this procedure to produce 2-40 clusters, calculated the Silhouette score for each, and selected 6 and 25 clusters as informative resolutions. We also increased clustering resolution manually to identify previously known distinct projection-defined populations, such as neurons projecting to MedCP but not to LatCP or or vice versa,[15,55] as well as neurons preferentially projecting to CPt[54]. Using these criteria we identified 34 clusters.

For each clustering resolution (6, 25, 34 clusters), we assessed cluster robustness using a machine learning-based random forest classifier.[33,88] The classifier was trained to identify which cluster a cell belongs to between a given pair of clusters using 80% of the total cells. For the remaining 20% of cells, a cluster was assigned between a pair of clusters based on the training. This process was applied to all pairs of clusters and repeated five times leaving mutually exclusive 20% cells, so that every cell was tested once. The entire procedure was repeated 10 times, yielding 10 classification outcomes per cell for each cluster pair. For each cell, we took clusters that were assigned at least once and calculated probabilities of the clusters. We then defined the cluster to which a cell was most frequently assigned as its max cluster, and calculated the distribution of max cluster assignment probabilities across all cells. Finally, we quantified the stability of each cluster by computing the proportion of cells whose original cluster matched their max cluster.

Co-innervation and motif analyses

Estimating the total number of neurons

To compare our observed results against expectations under an independent target choice model for co-innervation and motif analyses, we first estimated the total number of neurons, N_t, which includes not only the observed projecting neurons but also neurons that do not project to any of the dissected target regions, as previously described.[23] Here, projection is defined as the presence of a barcode with nonzero UMI count in a given region.

When a projection matrix consists of k regions in which j-th region receives projections from N_j neurons, the probability that a neuron does not project to any regions is

$$\prod_{j=1}^{k}\left(1-\frac{N_j}{N_t}\right)$$

N_t can be then inferred, as the sum of neurons that do not project to any regions and neurons projecting to at least one region, N_{obs}, is N_t,

$$N_{obs}+N_t\prod_{j=1}^{k}\left(1-\frac{N_j}{N_t}\right)=N_t$$

$$\Leftrightarrow N_{obs}\cdot N_t^{k-1}+\prod_{j=1}^{k}\left(N_t-N_j\right)=N_t^k$$

$$\Leftrightarrow N_{obs}\cdot N_t^{k-1}+\sum_{j=1}^{k}(-1)^j\ e_j\,N_t^{k-j}=0$$

$$\Leftrightarrow (N_{obs}-e_1)\cdot N_t^{k-1}+e_2\cdot N_t^{k-2}-e_3\cdot N_t^{k-3}+\cdots+(-1)^k e_k=0$$

where e_j denotes the j-th elementary symmetric polynomial in the variables $N_1, N_2, \ldots, N_k$. We solved this polynomial using the "roots" function in MATLAB and selected the largest positive real root, rounded to the nearest integer, as the estimated N_t.

Co-innervation analysis

To assess how similarly two regions, A and B, are innervated, we used the dice score ranging from 0 to 1, defined as $\frac{2N_{A\cap B}}{N_A+N_B}$, where $N_{A\cap B}$, N_A, and N_B are number of neurons of projecting to both regions, A, and B, respectively. A dice score of 0 indicates completely separate projections to A and B while 1 indicates that all neurons project to both regions.

Assuming independence,

$$N_{A\cap B}=N_tP(A)P(B)\ =\ \frac{N_AN_B}{N_t}$$

where the probability of projecting to region A is $P(A)$ and projecting to region B is $P(B)$. Therefore, the dice score under a model of independent target choice is equal to $\frac{2N_AN_B}{N_t(N_A+N_B)}$.

The rarity score, defined as the inverse of the Dice score assuming independence, can be calculated by

$$\frac{N_t}{2}\left(\frac{N_A+N_B}{N_AN_B}\right)=\ \frac{1}{2}\left(\frac{N_t}{N_A}+\frac{N_t}{N_B}\right).$$

It indicates how rare each co-innervation is relative to the total number of neurons. The rarity score ranges from 1 to infinity, where a value of 1 indicates that A and B are co-innervated by all neurons. A rarity score of infinity indicates that at least one of the two regions is not innervated by any neuron.

Based on these definitions, the product of the Dice score and rarity score is given by

$$\frac{N_t N_{A\cap B}}{N_A N_B}$$

This product is equal to 1, if projection probabilities are independent from each other. A value of more or less than 1 indicates over- or under-represented co-innervations, respectively.

We assessed a two-tailed *p* value for each co-innervation under the binomial distribution, where the probability of co-innervation was $P(A)P(B) = \frac{N_A N_B}{N_t^2}$, total number of trials was N_t, and observed number of co-innervations was $N_{A\cap B}$. We then adjusted the resulting *p* values using the Bonferroni correction by multiplying each *p* value by the number of comparisons.

Motif analysis

We examined motifs, i.e. binarized co-innervation patterns across all possible region combinations,[23] among 8 regions: CTX, NAc, OT, LS, VP, AMY, CP*, and CPt. For example, the CTX-NAc motif represents neurons that project to CTX and NAc, but do not project to any other region. There are 2^8-1 (excluding the non-projecting "motif") possible motifs with 8 target regions. Under the independent target choice model, the probability of each motif can be calculated by multiplying the probabilities of neurons projecting or not projecting to each region. We then calculated the ratio between the observed and expected neuron counts for each motif. To minimize the sampling artifacts, only motifs with either observed or expected counts higher than 5 were included in the analysis.

We assessed a two-tailed *p* value for each motif under the binomial distribution, where the probability of motif events was as described above, total number of trials was N_t, and the observed number of motif events was given in the dataset. We then adjusted the resulting *p* values using the Bonferroni correction by multiplying each *p* value by the number of comparisons.

Statistical analyses

Student's t test, one-way or two-way ANOVA with Bonferroni post-hoc tests, linear regression analysis, and Pearson correlation test were performed using R functions ("t.test", "aov" and "pairwise.t.test"). The significance of co-innervation and motifs were determined by the binomial test using "binocdf" function of Matlab and p-values were adjusted by Bonferroni correction. All tests were conducted as two-sided, and their significance levels are noted in the text.

ACKNOWLEDGMENTS

We thank Anthony M. Zador, Diane E. Griffin, Michael S. Diamond, and Hyungbae Kwon for generously providing us with plasmid constructs or mice. We also appreciate valuable input on dopaminergic projections from Kevin T. Beier, and feedback on this manuscript by Liqun Luo, Paul Masset, and Kebschull lab members. This work was supported by NIH grants DP1DA056668, R34132027, RF1AG078378, U01NS132161, R01DA054374, and R01DA056599 to JMK; a SFARI pilot award 875575 to JMK; the Packard Fellowship and Klingenstein Simons Fellowship to J.M.K and a postdoctoral fellowship from the Autism Science Foundation to H.K.

AUTHOR CONTRIBUTIONS

H.K. and J.M.K conceptualized the study. H.K. created constructs. H.K. and C.X. generated viruses. H.K. and C.W. generated sequencing libraries. M.L., and H.K. performed mouse crosses. H.K. performed all the other experiments. H.K. and J.M.K prepared the manuscript.

DECLARATION OF INTERESTS

We have applied for a patent related to POINTseq in the USA.

REFERENCES

1. Chklovskii, D.B., and Koulakov, A.A. (2004). Maps in the brain: what can we learn from them? Annu Rev Neurosci *27*, 369–392. https://doi.org/10.1146/annurev.neuro.27.070203.144226.

2. Swanson, L.W., and Bota, M. (2010). Foundational model of structural connectivity in the nervous system with a schema for wiring diagrams, connectome, and basic plan architecture. Proc Natl Acad Sci U S A *107*, 20610–20617. https://doi.org/10.1073/pnas.1015128107.

3. Luo, L. (2021). Architectures of neuronal circuits. Science *373*, eabg7285. https://doi.org/10.1126/science.abg7285.

4. Whitesell, J.D., Liska, A., Coletta, L., Hirokawa, K.E., Bohn, P., Williford, A., Groblewski, P.A., Graddis, N., Kuan, L., Knox, J.E., et al. (2021). Regional, Layer, and Cell-Type-Specific Connectivity of the Mouse Default Mode Network. Neuron *109*, 545-559.e8. https://doi.org/10.1016/j.neuron.2020.11.011.

5. Kebschull, J.M., Garcia da Silva, P., Reid, A.P., Peikon, I.D., Albeanu, D.F., and Zador, A.M. (2016). High-Throughput Mapping of Single-Neuron Projections by Sequencing of Barcoded RNA. Neuron *91*, 975–987. https://doi.org/10.1016/j.neuron.2016.07.036.

6. Muñoz-Castañeda, R., Zingg, B., Matho, K.S., Chen, X., Wang, Q., Foster, N.N., Li, A., Narasimhan, A., Hirokawa, K.E., Huo, B., et al. (2021). Cellular anatomy of the mouse primary motor cortex. Nature *598*, 159–166. https://doi.org/10.1038/s41586-021-03970-w.

7. Peng, H., Xie, P., Liu, L., Kuang, X., Wang, Y., Qu, L., Gong, H., Jiang, S., Li, A., Ruan, Z., et al. (2021). Morphological diversity of single neurons in molecularly defined cell types. Nature *598*, 174–181. https://doi.org/10.1038/s41586-021-03941-1.

8. Christensen, A.J., Ott, T., and Kepecs, A. (2022). Cognition and the single neuron: How cell types construct the dynamic computations of frontal cortex. Curr. Opin. Neurobiol. *77*, 102630. https://doi.org/10.1016/j.conb.2022.102630.

9. Luo, L., Callaway, E.M., and Svoboda, K. (2008). Genetic dissection of neural circuits. Neuron *57*, 634–660. https://doi.org/10.1016/j.neuron.2008.01.002.

10. Luo, L., Callaway, E.M., and Svoboda, K. (2018). Genetic dissection of neural circuits: A decade of progress. Neuron *98*, 865. https://doi.org/10.1016/j.neuron.2018.05.004.

11. Ben-Simon, Y., Hooper, M., Narayan, S., Daigle, T.L., Dwivedi, D., Way, S.W., Oster, A., Stafford, D.A., Mich, J.K., Taormina, M.J., et al. (2025). A suite of enhancer AAVs and transgenic mouse lines for genetic access to cortical cell types. Cell *188*, 3045-3064.e23. https://doi.org/10.1016/j.cell.2025.05.002.

12. Wickersham, I.R., Finke, S., Conzelmann, K.-K., and Callaway, E.M. (2007). Retrograde neuronal tracing with a deletion-mutant rabies virus. Nat. Methods *4*, 47–49. https://doi.org/10.1038/nmeth999.

13. Ren, J., Friedmann, D., Xiong, J., Liu, C.D., Ferguson, B.R., Weerakkody, T., DeLoach, K.E., Ran, C., Pun, A., Sun, Y., et al. (2018). Anatomically defined and functionally distinct dorsal raphe serotonin sub-systems. Cell *175*, 472-487.e20. https://doi.org/10.1016/j.cell.2018.07.043.

14. Lerner, T.N., Shilyansky, C., Davidson, T.J., Evans, K.E., Beier, K.T., Zalocusky, K.A., Crow, A.K., Malenka, R.C., Luo, L., Tomer, R., et al. (2015). Intact-brain analyses reveal distinct information carried by SNc dopamine subcircuits. Cell *162*, 635–647. https://doi.org/10.1016/j.cell.2015.07.014.

15. Beier, K.T., Steinberg, E.E., DeLoach, K.E., Xie, S., Miyamichi, K., Schwarz, L., Gao, X.J., Kremer, E.J., Malenka, R.C., and Luo, L. (2015). Circuit architecture of VTA dopamine neurons revealed by systematic input-output mapping. Cell *162*, 622–634. https://doi.org/10.1016/j.cell.2015.07.015.

16. Lammel, S., Ion, D.I., Roeper, J., and Malenka, R.C. (2011). Projection-specific modulation of dopamine neuron synapses by aversive and rewarding stimuli. Neuron *70*, 855–862. https://doi.org/10.1016/j.neuron.2011.03.025.

17. Schofield, B.R., Schofield, R.M., Sorensen, K.A., and Motts, S.D. (2007). On the use of retrograde tracers for identification of axon collaterals with multiple fluorescent retrograde tracers. Neuroscience *146*, 773–783. https://doi.org/10.1016/j.neuroscience.2007.02.026.

18. Bouin, A., Wu, G., Koyuncu, O.O., Ye, Q., Kim, K.-Y., Wu, M.Y., Tong, L., Chen, L., Phan, S., Mackey, M.R., et al. (2024). New rabies viral resources for multi-scale neural circuit mapping. Mol. Psychiatry *29*, 1951–1967. https://doi.org/10.1038/s41380-024-02451-6.

19. Gongwer, M.W., Klune, C.B., Couto, J., Jin, B., Enos, A.S., Chen, R., Friedmann, D., and DeNardo, L.A. (2023). Brain-wide projections and differential encoding of prefrontal neuronal classes underlying learned and innate threat avoidance. J. Neurosci. *43*, 5810–5830. https://doi.org/10.1523/JNEUROSCI.0697-23.2023.

20. Schwarz, L.A., Miyamichi, K., Gao, X.J., Beier, K.T., Weissbourd, B., DeLoach, K.E., Ren, J., Ibanes, S., Malenka, R.C., Kremer, E.J., et al. (2015). Viral-genetic tracing of the input–output organization of a central noradrenaline circuit. Nature *524*, 88–92. https://doi.org/10.1038/nature14600.

21. Economo, M.N., Viswanathan, S., Tasic, B., Bas, E., Winnubst, J., Menon, V., Graybuck, L.T., Nguyen, T.N., Smith, K.A., Yao, Z., et al. (2018). Distinct descending motor cortex pathways and their roles in movement. Nature *563*, 79–84. https://doi.org/10.1038/s41586-018-0642-9.

22. Aransay, A., Rodríguez-López, C., García-Amado, M., Clascá, F., and Prensa, L. (2015). Long-range projection neurons of the mouse ventral tegmental area: a single-cell axon tracing analysis. Front Neuroanat *9*, 59. https://doi.org/10.3389/fnana.2015.00059.

23. Han, Y., Kebschull, J.M., Campbell, R.A.A., Cowan, D., Imhof, F., Zador, A.M., and Mrsic-Flogel, T.D. (2018). The logic of single-cell projections from visual cortex. Nature *556*, 51–56. https://doi.org/10.1038/nature26159.

24. Zheng, T., Yang, Z., Li, A., Lv, X., Zhou, Z., Wang, X., Qi, X., Li, S., Luo, Q., Gong, H., et al. (2013). Visualization of brain circuits using two-photon fluorescence micro-optical sectioning tomography. Opt. Express *21*, 9839–9850. https://doi.org/10.1364/OE.21.009839.

25. Zheng, T., Feng, Z., Wang, X., Jiang, T., Jin, R., Zhao, P., Luo, T., Gong, H., Luo, Q., and Yuan, J. (2019). Review of micro-optical sectioning tomography (MOST): technology and applications for whole-brain optical imaging [Invited]. Biomed. Opt. Express *10*, 4075–4096. https://doi.org/10.1364/BOE.10.004075.

26. Kim, Y., Yang, G.R., Pradhan, K., Venkataraju, K.U., Bota, M., García Del Molino, L.C., Fitzgerald, G., Ram, K., He, M., Levine, J.M., et al. (2017). Brain-wide maps reveal stereotyped cell-type-based cortical architecture and subcortical sexual dimorphism. Cell *171*, 456-469.e22. https://doi.org/10.1016/j.cell.2017.09.020.

27. Winnubst, J., Bas, E., Ferreira, T.A., Wu, Z., Economo, M.N., Edson, P., Arthur, B.J., Bruns, C., Rokicki, K., Schauder, D., et al. (2019). Reconstruction of 1,000 Projection Neurons Reveals New Cell Types and Organization of Long-Range Connectivity in the Mouse Brain. Cell *179*, 268-281.e13. https://doi.org/10.1016/j.cell.2019.07.042.

28. Daetwyler, S., and Fiolka, R.P. (2023). Light-sheets and smart microscopy, an exciting future is dawning. Commun. Biol. *6*, 502. https://doi.org/10.1038/s42003-023-04857-4.

29. Tavakoli, M.R., Lyudchik, J., Januszewski, M., Vistunou, V., Agudelo Dueñas, N., Vorlaufer, J., Sommer, C., Kreuzinger, C., Oliveira, B., Cenameri, A., et al. (2025). Light-microscopy-based connectomic reconstruction of mammalian brain tissue. Nature. https://doi.org/10.1038/s41586-025-08985-1.

30. Glaser, A., Chandrashekar, J., Vasquez, S., Arshadi, C., Ouellette, N., Jiang, X., Baka, J., Kovacs, G., Woodard, M., Seshamani, S., et al. (2024). Expansion-assisted selective plane illumination microscopy for nanoscale imaging of centimeter-scale tissues. https://doi.org/10.7554/elife.91979.2.

31. Gao, L., Liu, S., Gou, L., Hu, Y., Liu, Y., Deng, L., Ma, D., Wang, H., Yang, Q., Chen, Z., et al. (2022). Single-neuron projectome of mouse prefrontal cortex. Nat. Neurosci. *25*, 515–529. https://doi.org/10.1038/s41593-022-01041-5.

32. Kebschull, J.M., Garcia da Silva, P., and Zador, A.M. (2016). A New Defective Helper RNA to Produce Recombinant Sindbis Virus that Infects Neurons but does not Propagate. Front Neuroanat *10*, 56. https://doi.org/10.3389/fnana.2016.00056.

33. Chen, X., Sun, Y.-C., Zhan, H., Kebschull, J.M., Fischer, S., Matho, K., Huang, Z.J., Gillis, J., and Zador, A.M. (2019). High-throughput mapping of long-range neuronal projection using in situ sequencing. Cell *179*, 772-786.e19. https://doi.org/10.1016/j.cell.2019.09.023.

34. Chen, Y., Chen, X., Baserdem, B., Zhan, H., Li, Y., Davis, M.B., Kebschull, J.M., Zador, A.M., Koulakov, A.A., and Albeanu, D.F. (2022). High-throughput sequencing of single neuron projections reveals spatial organization in the olfactory cortex. Cell *185*, 4117-4134.e28. https://doi.org/10.1016/j.cell.2022.09.038.

35. Gergues, M.M., Han, K.J., Choi, H.S., Brown, B., Clausing, K.J., Turner, V.S., Vainchtein, I.D., Molofsky, A.V., and Kheirbek, M.A. (2020). Circuit and molecular architecture of a ventral hippocampal network. Nat Neurosci *23*, 1444–1452. https://doi.org/10.1038/s41593-020-0705-8.

36. Huang, L., Kebschull, J.M., Fürth, D., Musall, S., Kaufman, M.T., Churchland, A.K., and Zador, A.M. (2020). BRICseq Bridges Brain-wide Interregional Connectivity to Neural Activity and Gene Expression in Single Animals. Cell *183*, 2040. https://doi.org/10.1016/j.cell.2020.12.009.

37. Sun, Y.-C., Chen, X., Fischer, S., Lu, S., Zhan, H., Gillis, J., and Zador, A.M. (2021). Integrating barcoded neuroanatomy with spatial transcriptional profiling enables identification of gene correlates of projections. Nat Neurosci *24*, 873–885. https://doi.org/10.1038/s41593-021-00842-4.

38. Zeisler, Z.R., London, L., Janssen, W.G., Fredericks, J.M., Elorette, C., Fujimoto, A., Zhan, H., Russ, B.E., Clem, R.L., Hof, P.R., et al. (2023). Single basolateral amygdala neurons in macaques exhibit distinct connectional motifs with frontal cortex. Neuron *111*, 3307-3320.e5. https://doi.org/10.1016/j.neuron.2023.09.024.

39. Harris, J.A., Hirokawa, K.E., Sorensen, S.A., Gu, H., Mills, M., Ng, L.L., Bohn, P., Mortrud, M., Ouellette, B., Kidney, J., et al. (2014). Anatomical characterization of Cre driver mice for neural circuit mapping and manipulation. Front Neural Circuits *8*, 76. https://doi.org/10.3389/fncir.2014.00076.

40. Klingler, E., Tomasello, U., Prados, J., Kebschull, J.M., Contestabile, A., Galiñanes, G.L., Fièvre, S., Santinha, A., Platt, R., Huber, D., et al. (2021). Temporal controls over inter-areal cortical projection neuron fate diversity. Nature *599*, 453–457. https://doi.org/10.1038/s41586-021-04048-3.

41. Brichta, L., and Greengard, P. (2014). Molecular determinants of selective dopaminergic vulnerability in Parkinsonâ€™s disease: an update. Front. Neuroanat. *8*, 152. https://doi.org/10.3389/fnana.2014.00152.

42. Lammel, S., Lim, B.K., and Malenka, R.C. (2014). Reward and aversion in a heterogeneous midbrain dopamine system. Neuropharmacology *76 Pt B*, 351–359. https://doi.org/10.1016/j.neuropharm.2013.03.019.

43. Garritsen, O., van Battum, E.Y., Grossouw, L.M., and Pasterkamp, R.J. (2023). Development, wiring and function of dopamine neuron subtypes. Nat Rev Neurosci *24*, 134–152. https://doi.org/10.1038/s41583-022-00669-3.

44. Heymann, G., Jo, Y.S., Reichard, K.L., McFarland, N., Chavkin, C., Palmiter, R.D., Soden, M.E., and Zweifel, L.S. (2020). Synergy of distinct dopamine projection populations in behavioral reinforcement. Neuron *105*, 909-920.e5. https://doi.org/10.1016/j.neuron.2019.11.024.

45. Menegas, W., Akiti, K., Amo, R., Uchida, N., and Watabe-Uchida, M. (2018). Dopamine neurons projecting to the posterior striatum reinforce avoidance of threatening stimuli. Nat Neurosci *21*, 1421–1430. https://doi.org/10.1038/s41593-018-0222-1.

46. Mahadevia, D., Saha, R., Manganaro, A., Chuhma, N., Ziolkowski-Blake, A., Morgan, A.A., Dumitriu, D., Rayport, S., and Ansorge, M.S. (2021). Dopamine promotes aggression in mice via ventral tegmental area to lateral septum projections. Nat. Commun. *12*, 6796. https://doi.org/10.1038/s41467-021-27092-z.

47. Howe, M.W., and Dombeck, D.A. (2016). Rapid signalling in distinct dopaminergic axons during locomotion and reward. Nature *535*, 505–510. https://doi.org/10.1038/nature18942.

48. Dai, B., Zheng, B., Dai, X., Cui, X., Yin, L., Cai, J., Zhuo, Y., Tritsch, N.X., Zweifel, L.S., Li, Y., et al. (2025). Experience-dependent dopamine modulation of male aggression. Nature *639*, 430–437. https://doi.org/10.1038/s41586-024-08459-w.

49. Fallon, J.H., and Moore, R.Y. (1978). Catecholamine innervation of the basal forebrain. IV. Topography of the dopamine projection to the basal forebrain and neostriatum. J. Comp. Neurol. *180*, 545–580. https://doi.org/10.1002/cne.901800310.

50. Moore, R.Y., and Bloom, F.E. (1978). Central catecholamine neuron systems: anatomy and physiology of the dopamine systems. Annu. Rev. Neurosci. *1*, 129–169. https://doi.org/10.1146/annurev.ne.01.030178.001021.

51. Swanson, L.W. (1982). The projections of the ventral tegmental area and adjacent regions: A combined fluorescent retrograde tracer and immunofluorescence study in the rat. Brain Res. Bull. *9*, 321–353. https://doi.org/10.1016/0361-9230(82)90145-9.

52. Schultz, W., Dayan, P., and Montague, P.R. (1997). A neural substrate of prediction and reward. Science *275*, 1593–1599. https://doi.org/10.1126/science.275.5306.1593.

53. Hefti, F., Enz, A., and Melamed, E. (1985). Partial lesions of the nigrostriatal pathway in the rat. Acceleration of transmitter synthesis and release of surviving dopaminergic neurones by drugs. Neuropharmacology *24*, 19–23. https://doi.org/10.1016/0028-3908(85)90090-5.

54. Menegas, W., Bergan, J.F., Ogawa, S.K., Isogai, Y., Umadevi Venkataraju, K., Osten, P., Uchida, N., and Watabe-Uchida, M. (2015). Dopamine neurons projecting to the posterior striatum form an anatomically distinct subclass. Elife *4*. https://doi.org/10.7554/elife.10032.

55. Poulin, J.-F., Caronia, G., Hofer, C., Cui, Q., Helm, B., Ramakrishnan, C., Chan, C.S., Dombeck, D.A., Deisseroth, K., and Awatramani, R. (2018). Mapping projections of molecularly defined dopamine neuron subtypes using intersectional genetic approaches. Nat Neurosci *21*, 1260–1271. https://doi.org/10.1038/s41593-018-0203-4.

56. Pereira Luppi, M., Azcorra, M., Caronia-Brown, G., Poulin, J.-F., Gaertner, Z., Gatica, S., Moreno-Ramos, O.A., Nouri, N., Dubois, M., Ma, Y.C., et al. (2021). Sox6 expression distinguishes dorsally and ventrally biased dopamine neurons in the substantia nigra with distinctive properties and embryonic origins. Cell Rep. *37*, 109975. https://doi.org/10.1016/j.celrep.2021.109975.

57. Zeng, H. (2022). What is a cell type and how to define it? Cell *185*, 2739–2755. https://doi.org/10.1016/j.cell.2022.06.031.

58. Zhang, R., Kim, A.S., Fox, J.M., Nair, S., Basore, K., Klimstra, W.B., Rimkunas, R., Fong, R.H., Lin, H., Poddar, S., et al. (2018). Mxra8 is a receptor for multiple arthritogenic alphaviruses. Nature *557*, 570–574. https://doi.org/10.1038/s41586-018-0121-3.

59. Zimmerman, O., Holmes, A.C., Kafai, N.M., Adams, L.J., and Diamond, M.S. (2023). Entry receptors - the gateway to alphavirus infection. J. Clin. Invest. *133*. https://doi.org/10.1172/JCI165307.

60. Wickersham, I.R., Lyon, D.C., Barnard, R.J.O., Mori, T., Finke, S., Conzelmann, K.-K., Young, J.A.T., and Callaway, E.M. (2007). Monosynaptic restriction of transsynaptic tracing from single, genetically targeted neurons. Neuron *53*, 639–647. https://doi.org/10.1016/j.neuron.2007.01.033.

61. Yao, Z., van Velthoven, C.T.J., Kunst, M., Zhang, M., McMillen, D., Lee, C., Jung, W., Goldy, J., Abdelhak, A., Aitken, M., et al. (2023). A high-resolution transcriptomic and spatial atlas of cell types in the whole mouse brain. Nature *624*, 317–332. https://doi.org/10.1038/s41586-023-06812-z.

62. Kim, H., Qi, H., Washington, C., Liang, X., and Kebschull, J.M. (2025). MAPseq2: a sensitive and cost-effective barcoded connectomics method. bioRxiv, 2025.06.23.661165. https://doi.org/10.1101/2025.06.23.661165.

63. Chinta, S.J., and Andersen, J.K. (2005). Dopaminergic neurons. Int. J. Biochem. Cell Biol. *37*, 942–946. https://doi.org/10.1016/j.biocel.2004.09.009.

64. Bissonette, G.B., and Roesch, M.R. (2016). Development and function of the midbrain dopamine system: what we know and what we need to. Genes Brain Behav. *15*, 62–73. https://doi.org/10.1111/gbb.12257.

65. Azcorra, M., Gaertner, Z., Davidson, C., He, Q., Kim, H., Nagappan, S., Hayes, C.K., Ramakrishnan, C., Fenno, L., Kim, Y.S., et al. (2023). Unique functional responses differentially map onto genetic subtypes of dopamine neurons. Nat Neurosci *26*, 1762–1774. https://doi.org/10.1038/s41593-023-01401-9.

66. Mendonça, M.D., da Silva, J.A., Hernandez, L.F., Castela, I., Obeso, J., and Costa, R.M. (2024). Dopamine neuron activity encodes the length of upcoming contralateral movement sequences. Curr. Biol. *34*, 1034-1047.e4. https://doi.org/10.1016/j.cub.2024.01.067.

67. Dodson, P.D., Dreyer, J.K., Jennings, K.A., Syed, E.C.J., Wade-Martins, R., Cragg, S.J., Bolam, J.P., and Magill, P.J. (2016). Representation of spontaneous movement by dopaminergic neurons is cell-type selective and disrupted in parkinsonism. Proc. Natl. Acad. Sci. U. S. A. *113*, E2180-8. https://doi.org/10.1073/pnas.1515941113.

68. Juarez, B., and Han, M.-H. (2016). Diversity of dopaminergic neural circuits in response to drug exposure.

Neuropsychopharmacology *41*, 2424–2446. https://doi.org/10.1038/npp.2016.32.

69. Volkow, N.D., Fowler, J.S., Wang, G.-J., Swanson, J.M., and Telang, F. (2007). Dopamine in drug abuse and addiction: results of imaging studies and treatment implications. Arch. Neurol. *64*, 1575–1579. https://doi.org/10.1001/archneur.64.11.1575.

70. Chen, A.P.F., Chen, L., Kim, T.A., and Xiong, Q. (2021). Integrating the roles of midbrain dopamine circuits in behavior and neuropsychiatric disease. Biomedicines *9*, 647. https://doi.org/10.3390/biomedicines9060647.

71. Davis, K.L., Kahn, R.S., Ko, G., and Davidson, M. (1991). Dopamine in schizophrenia: a review and reconceptualization. Am. J. Psychiatry *148*, 1474–1486. https://doi.org/10.1176/ajp.148.11.1474.

72. Zhou, Z.D., Yi, L.X., Wang, D.Q., Lim, T.M., and Tan, E.K. (2023). Role of dopamine in the pathophysiology of Parkinson's disease. Transl. Neurodegener. *12*, 44. https://doi.org/10.1186/s40035-023-00378-6.

73. Dauer, W., and Przedborski, S. (2003). Parkinson's disease. Neuron *39*, 889–909. https://doi.org/10.1016/s0896-6273(03)00568-3.

74. D'Amelio, M., Puglisi-Allegra, S., and Mercuri, N. (2018). The role of dopaminergic midbrain in Alzheimer's disease: Translating basic science into clinical practice. Pharmacol. Res. *130*, 414–419. https://doi.org/10.1016/j.phrs.2018.01.016.

75. Nobili, A., Latagliata, E.C., Viscomi, M.T., Cavallucci, V., Cutuli, D., Giacovazzo, G., Krashia, P., Rizzo, F.R., Marino, R., Federici, M., et al. (2017). Dopamine neuronal loss contributes to memory and reward dysfunction in a model of Alzheimer's disease. Nat. Commun. *8*, 14727. https://doi.org/10.1038/ncomms14727.

76. Poulin, J.-F., Gaertner, Z., Moreno-Ramos, O.A., and Awatramani, R. (2020). Classification of midbrain dopamine neurons using single-cell gene expression profiling approaches. Trends Neurosci. *43*, 155–169. https://doi.org/10.1016/j.tins.2020.01.004.

77. Morales, M., and Margolis, E.B. (2017). Ventral tegmental area: cellular heterogeneity, connectivity and behaviour. Nat. Rev. Neurosci. *18*, 73–85. https://doi.org/10.1038/nrn.2016.165.

78. Fields, H.L., Hjelmstad, G.O., Margolis, E.B., and Nicola, S.M. (2007). Ventral tegmental area neurons in learned appetitive behavior and positive reinforcement. Annu. Rev. Neurosci. *30*, 289–316. https://doi.org/10.1146/annurev.neuro.30.051606.094341.

79. Lammel, S., Hetzel, A., Häckel, O., Jones, I., Liss, B., and Roeper, J. (2008). Unique properties of mesoprefrontal neurons within a dual mesocorticolimbic dopamine system. Neuron *57*, 760–773. https://doi.org/10.1016/j.neuron.2008.01.022.

80. Zhang, Z., Liu, Q., Wen, P., Zhang, J., Rao, X., Zhou, Z., Zhang, H., He, X., Li, J., Zhou, Z., et al. (2017). Activation of the dopaminergic pathway from VTA to the medial olfactory tubercle generates odor-preference and reward. Elife *6*. https://doi.org/10.7554/eLife.25423.

81. Lee, J.Y., Jun, H., Soma, S., Nakazono, T., Shiraiwa, K., Dasgupta, A., Nakagawa, T., Xie, J.L., Chavez, J., Romo, R., et al. (2021). Dopamine facilitates associative memory encoding in the entorhinal cortex. Nature *598*, 321–326. https://doi.org/10.1038/s41586-021-03948-8.

82. Stamatakis, A.M., Jennings, J.H., Ung, R.L., Blair, G.A., Weinberg, R.J., Neve, R.L., Boyce, F., Mattis, J., Ramakrishnan, C., Deisseroth, K., et al. (2013). A unique population of ventral tegmental area neurons inhibits

the lateral habenula to promote reward. Neuron *80*, 1039–1053. https://doi.org/10.1016/j.neuron.2013.08.023.

83. Tolve, M., Ulusoy, A., Patikas, N., Islam, K.U.S., Bodea, G.O., Öztürk, E., Broske, B., Mentani, A., Wagener, A., van Loo, K.M.J., et al. (2021). The transcription factor BCL11A defines distinct subsets of midbrain dopaminergic neurons. Cell Rep. *36*, 109697. https://doi.org/10.1016/j.celrep.2021.109697.

84. Foster, N.N., Barry, J., Korobkova, L., Garcia, L., Gao, L., Becerra, M., Sherafat, Y., Peng, B., Li, X., Choi, J.-H., et al. (2021). The mouse cortico-basal ganglia-thalamic network. Nature *598*, 188–194. https://doi.org/10.1038/s41586-021-03993-3.

85. Hintiryan, H., Foster, N.N., Bowman, I., Bay, M., Song, M.Y., Gou, L., Yamashita, S., Bienkowski, M.S., Zingg, B., Zhu, M., et al. (2016). The mouse cortico-striatal projectome. Nat. Neurosci. *19*, 1100–1114. https://doi.org/10.1038/nn.4332.

86. Hunnicutt, B.J., Jongbloets, B.C., Birdsong, W.T., Gertz, K.J., Zhong, H., and Mao, T. (2016). A comprehensive excitatory input map of the striatum reveals novel functional organization. Elife *5*. https://doi.org/10.7554/eLife.19103.

87. Mukamel, E.A., and Ngai, J. (2019). Perspectives on defining cell types in the brain. Curr. Opin. Neurobiol. *56*, 61–68. https://doi.org/10.1016/j.conb.2018.11.007.

88. Tasic, B., Menon, V., Nguyen, T.N., Kim, T.K., Jarsky, T., Yao, Z., Levi, B., Gray, L.T., Sorensen, S.A., Dolbeare, T., et al. (2016). Adult mouse cortical cell taxonomy revealed by single cell transcriptomics. Nat. Neurosci. *19*, 335–346. https://doi.org/10.1038/nn.4216.

89. Wu, J., Kung, J., Dong, J., Chang, L., Xie, C., Habib, A., Hawes, S., Yang, N., Chen, V., Liu, Z., et al. (2019). Distinct connectivity and functionality of aldehyde dehydrogenase 1a1-positive nigrostriatal dopaminergic neurons in motor learning. Cell Rep. *28*, 1167-1181.e7. https://doi.org/10.1016/j.celrep.2019.06.095.

90. Kramer, D.J., Risso, D., Kosillo, P., Ngai, J., and Bateup, H.S. (2018). Combinatorial expression of Grp and Neurod6 defines dopamine neuron populations with distinct projection patterns and disease vulnerability. eNeuro *5*. https://doi.org/10.1523/ENEURO.0152-18.2018.

91. Jaeger, C.B., Joh, T.H., and Reis, D.J. (1983). The effect of forebrain lesions in the neonatal rat: survival of midbrain dopaminergic neurons and the crossed nigrostriatal projection. J. Comp. Neurol. *218*, 74–90. https://doi.org/10.1002/cne.902180105.

92. Rodríguez-López, C., Clascá, F., and Prensa, L. (2017). The mesoaccumbens pathway: A retrograde labeling and single-cell axon tracing analysis in the mouse. Front. Neuroanat. *11*, 25. https://doi.org/10.3389/fnana.2017.00025.

93. Farassat, N., Costa, K.M., Stojanovic, S., Albert, S., Kovacheva, L., Shin, J., Egger, R., Somayaji, M., Duvarci, S., Schneider, G., et al. (2019). In vivo functional diversity of midbrain dopamine neurons within identified axonal projections. Elife *8*. https://doi.org/10.7554/eLife.48408.

94. Tsutsui-Kimura, I., Tian, Z.M., Amo, R., Zhuo, Y., Li, Y., Campbell, M.G., Uchida, N., and Watabe-Uchida, M. (2025). Dopamine in the tail of the striatum facilitates avoidance in threat-reward conflicts. Nat. Neurosci. *28*, 795–810. https://doi.org/10.1038/s41593-025-01902-9.

95. Dice, L.R. (1945). Measures of the amount of ecologic association between species. Ecology *26*, 297–302. https://doi.org/10.2307/1932409.

96. Richard, J.M., Stout, N., Acs, D., and Janak, P.H. (2018). Ventral pallidal encoding of reward-seeking behavior depends on the underlying associative structure. Elife *7*. https://doi.org/10.7554/eLife.33107.

97. Ottenheimer, D.J., Wang, K., Tong, X., Fraser, K.M., Richard, J.M., and Janak, P.H. (2020). Reward activity in ventral pallidum tracks satiety-sensitive preference and drives choice behavior. Sci. Adv. *6*, eabc9321. https://doi.org/10.1126/sciadv.abc9321.

98. Ottenheimer, D.J., Bari, B.A., Sutlief, E., Fraser, K.M., Kim, T.H., Richard, J.M., Cohen, J.Y., and Janak, P.H. (2020). A quantitative reward prediction error signal in the ventral pallidum. Nat. Neurosci. *23*, 1267–1276. https://doi.org/10.1038/s41593-020-0688-5.

99. Murata, K., Kanno, M., Ieki, N., Mori, K., and Yamaguchi, M. (2015). Mapping of learned odor-induced motivated behaviors in the mouse olfactory tubercle. J. Neurosci. *35*, 10581–10599. https://doi.org/10.1523/JNEUROSCI.0073-15.2015.

100. Ikemoto, S. (2007). Dopamine reward circuitry: two projection systems from the ventral midbrain to the nucleus accumbens-olfactory tubercle complex. Brain Res. Rev. *56*, 27–78. https://doi.org/10.1016/j.brainresrev.2007.05.004.

101. Tobler, P.N., Fiorillo, C.D., and Schultz, W. (2005). Adaptive coding of reward value by dopamine neurons. Science *307*, 1642–1645. https://doi.org/10.1126/science.1105370.

102. Jun, H., Lee, J.Y., Bleza, N.R., Ichii, A., Donohue, J.D., and Igarashi, K.M. (2024). Prefrontal and lateral entorhinal neurons co-dependently learn item-outcome rules. Nature *633*, 864–871. https://doi.org/10.1038/s41586-024-07868-1.

103. Vander Weele, C.M., Siciliano, C.A., Matthews, G.A., Namburi, P., Izadmehr, E.M., Espinel, I.C., Nieh, E.H., Schut, E.H.S., Padilla-Coreano, N., Burgos-Robles, A., et al. (2018). Dopamine enhances signal-to-noise ratio in cortical-brainstem encoding of aversive stimuli. Nature *563*, 397–401. https://doi.org/10.1038/s41586-018-0682-1.

104. Kienast, T., Hariri, A.R., Schlagenhauf, F., Wrase, J., Sterzer, P., Buchholz, H.G., Smolka, M.N., Gründer, G., Cumming, P., Kumakura, Y., et al. (2008). Dopamine in amygdala gates limbic processing of aversive stimuli in humans. Nat. Neurosci. *11*, 1381–1382. https://doi.org/10.1038/nn.2222.

105. Lutas, A., Kucukdereli, H., Alturkistani, O., Carty, C., Sugden, A.U., Fernando, K., Diaz, V., Flores-Maldonado, V., and Andermann, M.L. (2019). State-specific gating of salient cues by midbrain dopaminergic input to basal amygdala. Nat. Neurosci. *22*, 1820–1833. https://doi.org/10.1038/s41593-019-0506-0.

106. Tang, W., Kochubey, O., Kintscher, M., and Schneggenburger, R. (2020). A VTA to basal amygdala dopamine projection contributes to signal salient somatosensory events during fear learning. J. Neurosci. *40*, 3969–3980. https://doi.org/10.1523/JNEUROSCI.1796-19.2020.

107. Duvarci, S. (2024). Dopaminergic circuits controlling threat and safety learning. Trends Neurosci. *47*, 1014–1027. https://doi.org/10.1016/j.tins.2024.10.001.

108. Pacelli, C., Giguère, N., Bourque, M.-J., Lévesque, M., Slack, R.S., and Trudeau, L.-É. (2015). Elevated mitochondrial bioenergetics and axonal arborization size are key contributors to the vulnerability of dopamine neurons. Curr. Biol. *25*, 2349–2360. https://doi.org/10.1016/j.cub.2015.07.050.

109. Matsuda, W., Furuta, T., Nakamura, K.C., Hioki, H., Fujiyama, F., Arai, R., and Kaneko, T. (2009). Single

nigrostriatal dopaminergic neurons form widely spread and highly dense axonal arborizations in the neostriatum. J. Neurosci. *29*, 444–453. https://doi.org/10.1523/JNEUROSCI.4029-08.2009.

110. Giguère, N., Delignat-Lavaud, B., Herborg, F., Voisin, A., Li, Y., Jacquemet, V., Anand-Srivastava, M., Gether, U., Giros, B., and Trudeau, L.-É. (2019). Increased vulnerability of nigral dopamine neurons after expansion of their axonal arborization size through D2 dopamine receptor conditional knockout. PLoS Genet. *15*, e1008352. https://doi.org/10.1371/journal.pgen.1008352.

111. Seiler, J.L., Cosme, C.V., Sherathiya, V.N., Schaid, M.D., Bianco, J.M., Bridgemohan, A.S., and Lerner, T.N. (2022). Dopamine signaling in the dorsomedial striatum promotes compulsive behavior. Curr. Biol. *32*, 1175-1188.e5. https://doi.org/10.1016/j.cub.2022.01.055.

112. Pascoli, V., Terrier, J., Hiver, A., and Lüscher, C. (2015). Sufficiency of mesolimbic dopamine neuron stimulation for the progression to addiction. Neuron *88*, 1054–1066. https://doi.org/10.1016/j.neuron.2015.10.017.

113. Zhang, F., Gradinaru, V., Adamantidis, A.R., Durand, R., Airan, R.D., de Lecea, L., and Deisseroth, K. (2010). Optogenetic interrogation of neural circuits: technology for probing mammalian brain structures. Nat Protoc *5*, 439–456. https://doi.org/10.1038/nprot.2009.226.

114. Lavoie, A., and Liu, B.-H. (2020). Canine Adenovirus 2: A natural choice for brain circuit dissection. Front. Mol. Neurosci. *13*, 9. https://doi.org/10.3389/fnmol.2020.00009.

115. Peng, S., Yang, X., Meng, S., Liu, F., Lv, Y., Yang, H., Kong, Y., Xie, W., and Li, M. (2024). Dual circuits originating from the ventral hippocampus independently facilitate affective empathy. Cell Rep *43*, 114277. https://doi.org/10.1016/j.celrep.2024.114277.

116. Gradinaru, V., Zhang, F., Ramakrishnan, C., Mattis, J., Prakash, R., Diester, I., Goshen, I., Thompson, K.R., and Deisseroth, K. (2010). Molecular and cellular approaches for diversifying and extending optogenetics. Cell *141*, 154–165. https://doi.org/10.1016/j.cell.2010.02.037.

117. Lo, L., and Anderson, D.J. (2011). A Cre-dependent, anterograde transsynaptic viral tracer for mapping output pathways of genetically marked neurons. Neuron *72*, 938–950. https://doi.org/10.1016/j.neuron.2011.12.002.

118. Zingg, B., Chou, X.-L., Zhang, Z.-G., Mesik, L., Liang, F., Tao, H.W., and Zhang, L.I. (2017). AAV-Mediated Anterograde Transsynaptic Tagging: Mapping Corticocollicular Input-Defined Neural Pathways for Defense Behaviors. Neuron *93*, 33–47. https://doi.org/10.1016/j.neuron.2016.11.045.

119. Walther, W., and Stein, U. (1996). Cell type specific and inducible promoters for vectors in gene therapy as an approach for cell targeting. J. Mol. Med. *74*, 379–392. https://doi.org/10.1007/s001090050039.

120. Radhiyanti, P.T., Konno, A., Matsuzaki, Y., and Hirai, H. (2021). Comparative study of neuron-specific promoters in mouse brain transduced by intravenously administered AAV-PHP.eB. Neurosci. Lett. *756*, 135956. https://doi.org/10.1016/j.neulet.2021.135956.

121. Hughes, A.C., Pittman, B.G., Xu, B., Gammons, J.W., Webb, C.M., Nolen, H.G., Chapman, P., Bikoff, J.B., and Schwarz, L.A. (2024). A single-vector intersectional AAV strategy for interrogating cellular diversity and brain function. Nat. Neurosci. *27*, 1400–1410. https://doi.org/10.1038/s41593-024-01659-7.

122. Fenno, L.E., Mattis, J., Ramakrishnan, C., Hyun, M., Lee, S.Y., He, M., Tucciarone, J., Selimbeyoglu, A., Berndt, A., Grosenick, L., et al. (2014). Targeting cells with single vectors using multiple-feature Boolean logic. Nat. Methods *11*, 763–772. https://doi.org/10.1038/nmeth.2996.

123. Jeong, M., Choi, J.-H., Jang, H., Sohn, D.H., Wang, Q., Lee, J., Yao, L., Lee, E.J., Fan, J., Pratelli, M., et al. (2024). Viral vector-mediated transgene delivery with novel recombinase systems for targeting neuronal populations defined by multiple features. Neuron *112*, 56-72.e4. https://doi.org/10.1016/j.neuron.2023.09.038.

124. Guenthner, C.J., Miyamichi, K., Yang, H.H., Heller, H.C., and Luo, L. (2013). Permanent Genetic Access to Transiently Active Neurons via TRAP: Targeted Recombination in Active Populations. Neuron *78*, 773–784. https://doi.org/10.1016/j.neuron.2013.03.025.

125. Allen, W.E., DeNardo, L.A., Chen, M.Z., Liu, C.D., Loh, K.M., Fenno, L.E., Ramakrishnan, C., Deisseroth, K., and Luo, L. (2017). Thirst-associated preoptic neurons encode an aversive motivational drive. Science *357*, 1149–1155. https://doi.org/10.1126/science.aan6747.

126. DeNardo, L., and Luo, L. (2017). Genetic strategies to access activated neurons. Curr Opin Neurobiol *45*, 121–129. https://doi.org/10.1016/j.conb.2017.05.014.

127. Lee, D., Hyun, J.H., Jung, K., Hannan, P., and Kwon, H.-B. (2017). A calcium- and light-gated switch to induce gene expression in activated neurons. Nat Biotechnol *35*, 858–863. https://doi.org/10.1038/nbt.3902.

128. Wang, W., Wildes, C.P., Pattarabanjird, T., Sanchez, M.I., Glober, G.F., Matthews, G.A., Tye, K.M., and Ting, A.Y. (2017). A light- and calcium-gated transcription factor for imaging and manipulating activated neurons. Nat Biotechnol *35*, 864–871. https://doi.org/10.1038/nbt.3909.

129. Barykina, N.V., Karasev, M.M., Verkhusha, V.V., and Shcherbakova, D.M. (2022). Technologies for large-scale mapping of functional neural circuits active during a user-defined time window. Prog Neurobiol *216*, 102290. https://doi.org/10.1016/j.pneurobio.2022.102290.

130. Uyaniker, S., van der Spek, S.J.F., Reinders, N.R., Xiong, H., Li, K.W., Bossers, K., Smit, A.B., Verhaagen, J., and Kessels, H.W. (2019). The effects of Sindbis viral vectors on neuronal function. Front. Cell. Neurosci. *13*, 362. https://doi.org/10.3389/fncel.2019.00362.

131. Yuan, L., Chen, X., Zhan, H., Henry, G.L., and Zador, A.M. (2024). Massive multiplexing of spatially resolved single neuron projections with axonal BARseq. Nat. Commun. *15*, 8371. https://doi.org/10.1038/s41467-024-52756-x.

132. Gutierrez-Guerrero, A., Cosset, F.-L., and Verhoeyen, E. (2020). Lentiviral vector pseudotypes: Precious tools to improve gene modification of hematopoietic cells for research and gene therapy. Viruses *12*, 1016. https://doi.org/10.3390/v12091016.

133. Joglekar, A.V., and Sandoval, S. (2017). Pseudotyped Lentiviral vectors: One vector, many guises. Hum. Gene Ther. Methods *28*, 291–301. https://doi.org/10.1089/hgtb.2017.084.

134. Jin, L., Sullivan, H.A., Zhu, M., Lea, N.E., Lavin, T.K., Fu, X., Matsuyama, M., Hou, Y., Feng, G., and Wickersham, I.R. (2023). Third-generation rabies viral vectors allow nontoxic retrograde targeting of projection neurons with greatly increased efficiency. Cell Rep. Methods *3*, 100644. https://doi.org/10.1016/j.crmeth.2023.100644.

135. Beier, K.T., Gao, X.J., Xie, S., DeLoach, K.E., Malenka, R.C., and Luo, L. (2019). Topological organization of ventral tegmental area connectivity revealed by viral-genetic dissection of input-output relations. Cell Rep. *26*, 159-167.e6. https://doi.org/10.1016/j.celrep.2018.12.040.

136. Poulin, J.-F., Zou, J., Drouin-Ouellet, J., Kim, K.-Y.A., Cicchetti, F., and Awatramani, R.B. (2014). Defining

midbrain dopaminergic neuron diversity by single-cell gene expression profiling. Cell Rep. *9*, 930–943. https://doi.org/10.1016/j.celrep.2014.10.008.

137. La Manno, G., Gyllborg, D., Codeluppi, S., Nishimura, K., Salto, C., Zeisel, A., Borm, L.E., Stott, S.R.W., Toledo, E.M., Villaescusa, J.C., et al. (2016). Molecular diversity of midbrain development in mouse, human, and stem cells. Cell *167*, 566-580.e19. https://doi.org/10.1016/j.cell.2016.09.027.

138. Liu, L., Yun, Z., Manubens-Gil, L., Chen, H., Xiong, F., Dong, H., Zeng, H., Hawrylycz, M., Ascoli, G.A., and Peng, H. (2025). Connectivity of single neurons classifies cell subtypes in mouse brains. Nat. Methods *22*, 861–873. https://doi.org/10.1038/s41592-025-02621-6.

139. Zafiri, D., and Duvarci, S. (2022). Dopaminergic circuits underlying associative aversive learning. Front. Behav. Neurosci. *16*, 1041929. https://doi.org/10.3389/fnbeh.2022.1041929.

140. Weele, C.M.V., Siciliano, C.A., and Tye, K.M. (2019). Dopamine tunes prefrontal outputs to orchestrate aversive processing. Brain Res. *1713*, 16–31. https://doi.org/10.1016/j.brainres.2018.11.044.

141. Rosenkranz, J.A., and Grace, A.A. (2002). Dopamine-mediated modulation of odour-evoked amygdala potentials during pavlovian conditioning. Nature *417*, 282–287. https://doi.org/10.1038/417282a.

142. Liu, P., Gao, C., Wu, J., Wu, T., Zhang, Y., Liu, C., Sun, C., and Li, A. (2023). Negative valence encoding in the lateral entorhinal cortex during aversive olfactory learning. Cell Rep. *42*, 113204. https://doi.org/10.1016/j.celrep.2023.113204.

143. van Erp, A.M., and Miczek, K.A. (2000). Aggressive behavior, increased accumbal dopamine, and decreased cortical serotonin in rats. J. Neurosci. *20*, 9320–9325. https://doi.org/10.1523/jneurosci.20-24-09320.2000.

144. Shokry, I.M., Sinha, V., Da Silva, G., Park, S.-B., Callanan, J.J., and Tao, R. (2019). Comparison of electroencephalogram (EEG) response to MDPV versus the hallucinogenic drugs MK-801 and ketamine in rats. Exp. Neurol. *313*, 26–36. https://doi.org/10.1016/j.expneurol.2018.12.001.

145. Li, X., Xiong, L., and Li, Y. (2025). The role of the prefrontal cortex in modulating aggression in humans and rodents. Behav. Brain Res. *476*, 115285. https://doi.org/10.1016/j.bbr.2024.115285.

146. Bai, F., Huang, L., Deng, J., Long, Z., Hao, X., Chen, P., Wu, G., Wen, H., Deng, Q., Bao, X., et al. (2023). Prelimbic area to lateral hypothalamus circuit drives social aggression. iScience *26*, 107718. https://doi.org/10.1016/j.isci.2023.107718.

147. Bayless, D.W., Yang, T., Mason, M.M., Susanto, A.A.T., Lobdell, A., and Shah, N.M. (2019). Limbic neurons shape sex recognition and social behavior in sexually naive males. Cell *176*, 1190-1205.e20. https://doi.org/10.1016/j.cell.2018.12.041.

148. Padilla, S.L., Qiu, J., Soden, M.E., Sanz, E., Nestor, C.C., Barker, F.D., Quintana, A., Zweifel, L.S., Rønnekleiv, O.K., Kelly, M.J., et al. (2016). Agouti-related peptide neural circuits mediate adaptive behaviors in the starved state. Nat. Neurosci. *19*, 734–741. https://doi.org/10.1038/nn.4274.

149. Takahashi, A., Durand-de Cuttoli, R., Flanigan, M.E., Hasegawa, E., Tsunematsu, T., Aleyasin, H., Cherasse, Y., Miya, K., Okada, T., Keino-Masu, K., et al. (2022). Lateral habenula glutamatergic neurons projecting to the dorsal raphe nucleus promote aggressive arousal in mice. Nat. Commun. *13*, 4039. https://doi.org/10.1038/s41467-022-31728-z.

150. Gouveia, F.V., and Ibrahim, G.M. (2022). Habenula as a neural substrate for aggressive behavior. Front. Psychiatry *13*, 817302. https://doi.org/10.3389/fpsyt.2022.817302.

151. Vandenberghe, L.H., Xiao, R., Lock, M., Lin, J., Korn, M., and Wilson, J.M. (2010). Efficient serotype-dependent release of functional vector into the culture medium during adeno-associated virus manufacturing. Hum Gene Ther *21*, 1251–1257. https://doi.org/10.1089/hum.2010.107.

152. Kebschull, J.M., and Zador, A.M. (2015). Sources of PCR-induced distortions in high-throughput sequencing data sets. Nucleic Acids Res *43*, e143. https://doi.org/10.1093/nar/gkv717.

153. Langmead, B., Trapnell, C., Pop, M., and Salzberg, S.L. (2009). Ultrafast and memory-efficient alignment of short DNA sequences to the human genome. Genome Biol *10*, R25. https://doi.org/10.1186/gb-2009-10-3-r25.

154. Zeisel, A., Muñoz-Manchado, A.B., Codeluppi, S., Lönnerberg, P., La Manno, G., Juréus, A., Marques, S., Munguba, H., He, L., Betsholtz, C., et al. (2015). Brain structure. Cell types in the mouse cortex and hippocampus revealed by single-cell RNA-seq. Science *347*, 1138–1142. https://doi.org/10.1126/science.aaa1934.

155. Kimes, P.K., Liu, Y., Neil Hayes, D., and Marron, J.S. (2017). Statistical significance for hierarchical clustering. Biometrics *73*, 811–821. https://doi.org/10.1111/biom.12647.

156. Rose, P.P., Hanna, S.L., Spiridigliozzi, A., Wannissorn, N., Beiting, D.P., Ross, S.R., Hardy, R.W., Bambina, S.A., Heise, M.T., and Cherry, S. (2011). Natural resistance-associated macrophage protein is a cellular receptor for sindbis virus in both insect and mammalian hosts. Cell Host Microbe *10*, 97–104. https://doi.org/10.1016/j.chom.2011.06.009.

157. Ma, H., Kim, A.S., Kafai, N.M., Earnest, J.T., Shah, A.P., Case, J.B., Basore, K., Gilliland, T.C., Sun, C., Nelson, C.A., et al. (2020). LDLRAD3 is a receptor for Venezuelan equine encephalitis virus. Nature *588*, 308–314. https://doi.org/10.1038/s41586-020-2915-3.

158. Clark, L.E., Clark, S.A., Lin, C., Liu, J., Coscia, A., Nabel, K.G., Yang, P., Neel, D.V., Lee, H., Brusic, V., et al. (2022). VLDLR and ApoER2 are receptors for multiple alphaviruses. Nature *602*, 475–480. https://doi.org/10.1038/s41586-021-04326-0.

SUPPLEMENTAL FIGURES

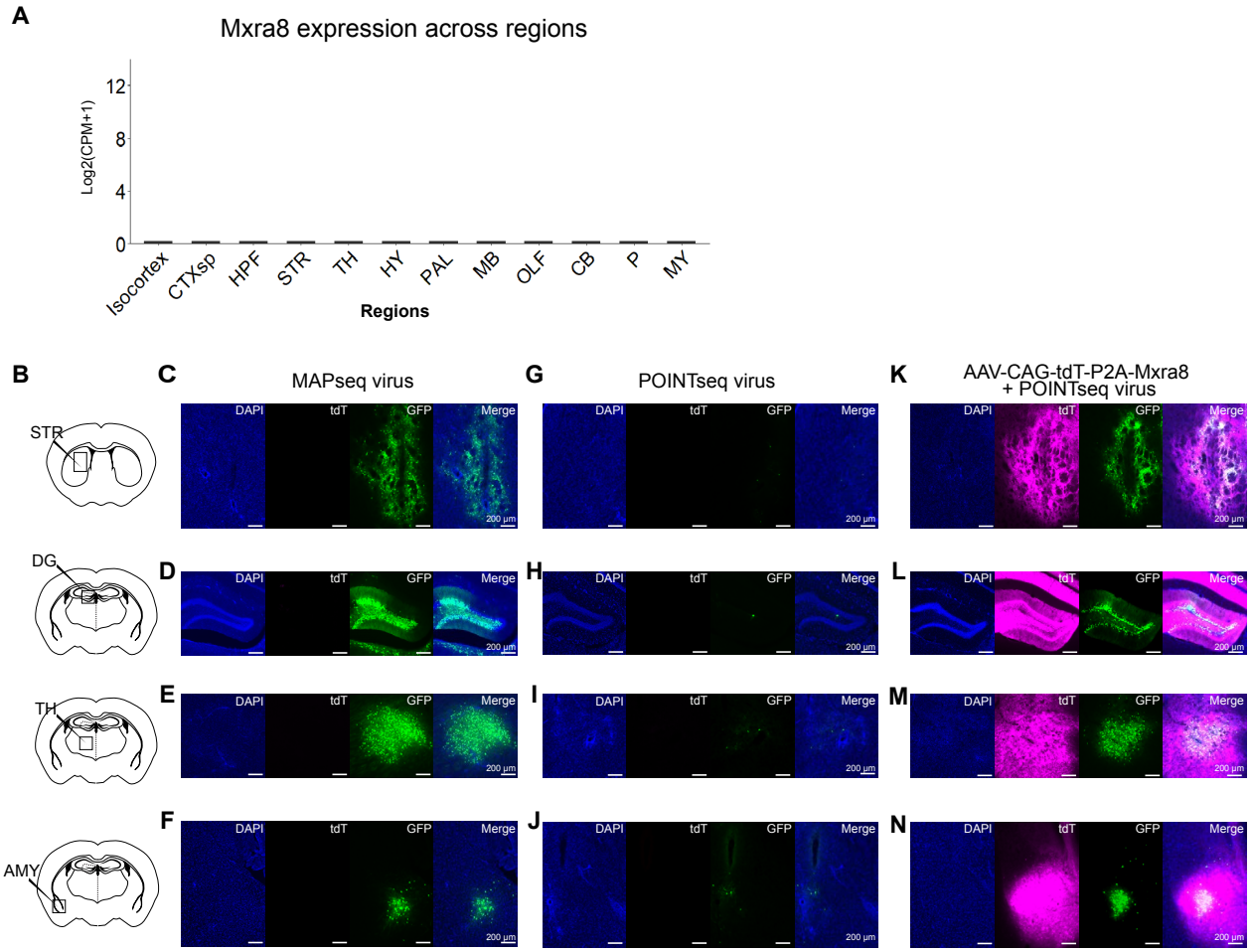

Figure S1. Mxra8 is not endogenously expressed throughout the mouse brain, and POINTseq virus infects neurons in the Mxra8-dependent manner across multiple brain regions.

(A) Expression of Mxra8 across regions of the mouse brain. Counts per million mapped reads (CPM) values were adapted from Allen Brain Cell Atlas scRNAseq datasets for the entire mouse brain. The plots display a central line, box, and whiskers representing the median, interquartile range (IQR), and data points within ±1.5× IQR. CTXsp: cortical subplate, HPF: hippocampal formation, STR: striatum, TH: Thalamus, HY: hypothalamus, PAL: pallidum, MB: midbrain, OLF: olfactory areas, CB: cerebellum, P: pons, MY: medulla.

(B) Mxra8-dependent POINTseq virus infection was assessed across brain regions including striatum (STR), dentate gyrus (DG), thalamus (TH), and amygdala (AMY).

(C-F) MAPseq virus efficiently infects these regions.

(G-J) Without exogenous Mxra8 expression, POINTseq virus rarely infects cells in these regions.

(K-N) With exogenous Mxra8 expression, POINTseq virus infects many cells in these regions. POINTseq virus was injected 18 days after the AAV injection.

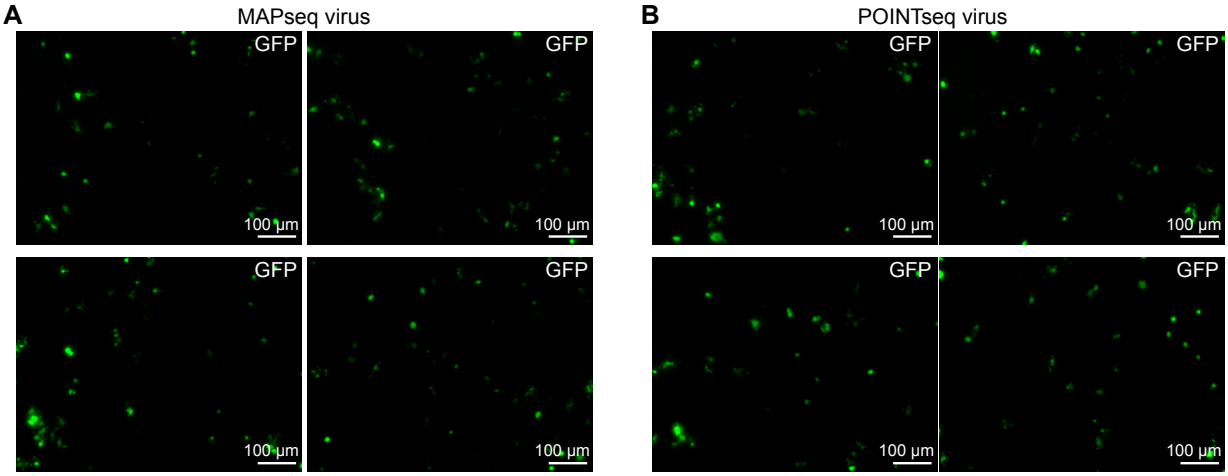

Figure S2. Confirmation of the propagation-incompetency of the POINTseq virus.
In a plaque assay, neither MAPseq (A) nor POINTseq virus (B) produce plaques.

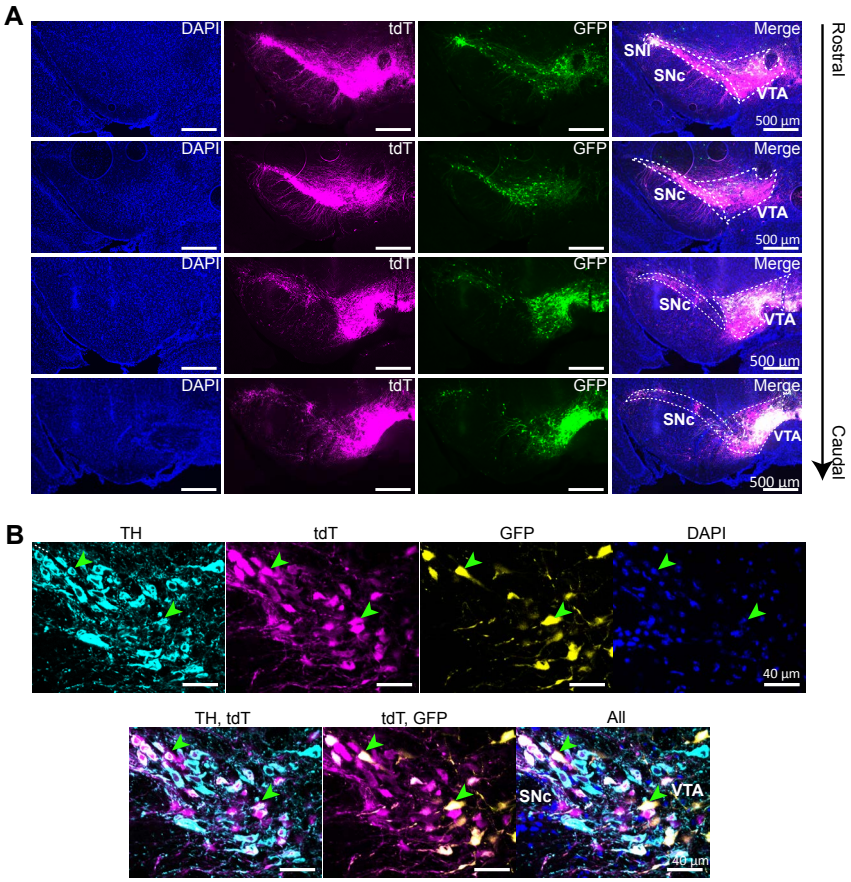

Figure S3. POINTseq virus specifically infects dopamine neurons in the VTA and SNc of DAT-Cre mice.
(A) The POINTseq virus specifically infects tdT+ (DAT^+) neurons spanning the VTA and SNc along the rostral–caudal axis.
(B) POINTseq virus infects DA neurons which are TH+ and tdT+ (DAT+). Green arrowheads indicate example cells of the infected cells which are GFP+, TH+, and tdT+.

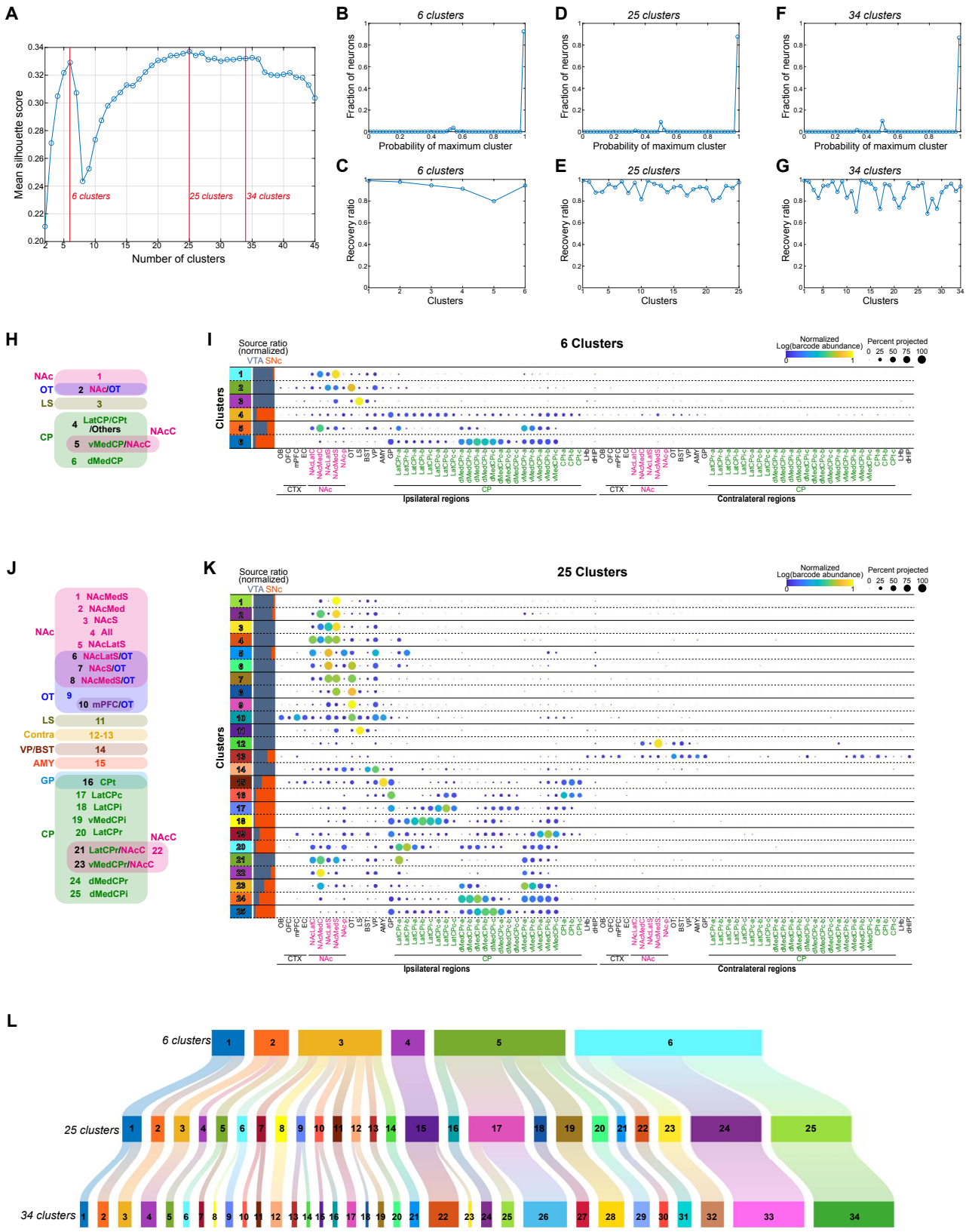

Figure S4. Hierarchical clustering of dopamine neurons at different cluster resolutions.

(A) Mean silhouette score (blue) and number of clusters (orange) according to the preset cluster number, where non-significant preset clusters were merged based on the *p* values (STAR methods). 6, 25, and 34 cluster

resolutions are selected for further analysis and comparisons.
(B-G) Random forest-based analysis for the 6, 25, and 34 cluster resolutions. (B, D, F) Distribution of probabilities that individual neurons were assigned to their maximum (most frequently assigned) cluster. At the 6, 25, and 34 cluster resolutions, 92.5% (3,526/3,813), 87.7% (3,343/3,813), and 86.7% (3,307/3,813) of neurons, respectively, were assigned to their maximum cluster with a probability greater than 98%. (C, E, G) Fraction of neurons whose maximum cluster is assigned to their original cluster. The average recovery ratios were 92.8%, 91.9%, and 89.2% for the 6, 25, and 34 cluster resolutions, respectively.
(H, I) Characterization of each cluster based on primary target regions (H) and a dot plot showing the mean projection patterns and the fraction of neurons projecting to each target region (I) at the 6 cluster resolution.
(J, K) Characterization of each cluster based on primary target regions (J) and a dot plot showing the mean projection patterns and the fraction of neurons projecting to each target region (K) at the 25 cluster resolution.
(L) Hierarchical relationship of clusters between the 6, 25, and 34 cluster resolutions.

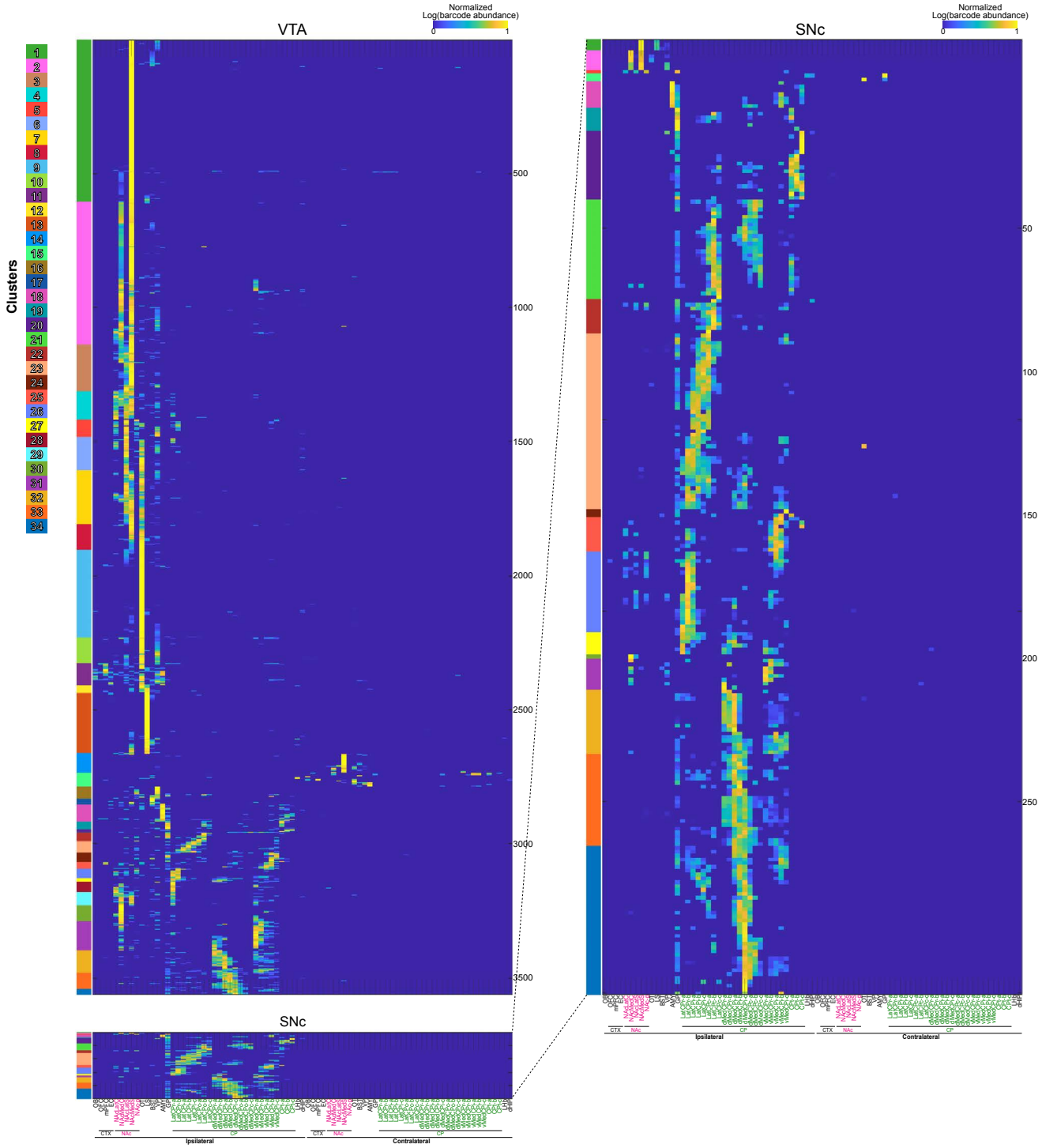

Figure S5. Projection matrices for VTA and SNc DA neurons, separately plotted from the combined matrix shown in Figure 3D.

Known dinstinct populations

A) Neurons (SNc) projecting to CP, but not to NAc or mPFC (Lammel et al., 2008)
B) Neurons (VTA) projecting to mPFC, but not to CP, NAcLatS, or NAcC (Lammel et al., 2008)
C) Neurons (VTA) projecting to NAcLatS or NAcC, but not to CP or mPFC (Lammel et al., 2008)
D) Neurons (VTA) projecting to NAc, but not to LS (Mahadevia et al., 2021)
E) Neurons (VTA) projecting to LS, but not to NAc (Mahadevia et al., 2021)
F) Neurons (VTA) projecting to NAcLat, and possibly to NAcC, MedCP, or LatCP, but not to NAcMedS, VP, LS, BST, or mPFC (Beier, 2015)
G) Neurons (VTA) projecting to NAcMed, and possibly to NAcC, MedCP, VP, or LS, but not to NAcLatS, DLS, BST, or mPFC (Beier, 2015)
H) Neurons (SNc) projecting to LatCP, with minimal projections to other CP subregions (Lerner et al., 2015)
I) Neurons (SNc) projecting to MedCP, with minimal projections to other CP subregions (Lerner et al., 2015)
J) Neurons (SNc, specifically SNL) primarily projecting to CPt and a small projection to LatCPc, with rare projections to other CP subregions, AMY, or LHb (Menegas et al., 2015; Menegas et al., 2018)
K) Aldh1a1+ neurons (SNc) projecting to CPr, LatCPi, dMedCPi, and LatCPc, with minimal projections to other CP subregions (Poulin et al., 2018; Wu et al., 2019)
L) Aldh1a1+ neurons (VTA) projecting to NAcMedS, OT, or LS, with minimal projections to NAcLatS and CP (Poulin et al., 2018)
M) Vglut2+ neurons (SNc) projecting to CPt, with minimal projections to other CP subregions (Poulin et al., 2018, Nat Neurosci)
N) Vglut2+ neurons (VTA) projecting to NAcMedS, OT, AMY, LS, BST, mPFC, or ET, with minimal projections to NAcLatS and CP (Poulin et al., 2018)
O) Calb1+ neurons (SNc) projecting to MedCPr, vMedCPi, vMedCPc, and CPt, with minimal projections to other CP subregions (Poulin et al., 2018)
P) Sox6+ neurons (VTA) projecting to NAcLatS or NAcC, but not to NAcMedS (Poulin et al., 2018)
Q) Cck+ neurons* (VTA) projecting to NAc, OT, LS, AMY, mPFC, ET, BST, vMedCPr, and vMedCPi, with minimal projections to other CP subregions (Poulin et al., 2018)
R) Cck+ neurons* (VTA) projecting to NAcMedS or AMY, but not much to NAcC or NAcLatS (Heymann et al., 2020)
S) Crhr1+ neurons (VTA) projecting to NAcC, with minimal projections to NAcS (Heymann et al., 2020)
T) Grp+/Neurod6- neurons (VTA/SNc) projecting to NAc, MedCP, mPFC, BLA, or LS, with minimal projections to LatCP (Kramer et al. 2018)
U) Neurod6+ neurons (VTA) projecting to NAcMedS or OT, with minimal projections to NAcLatS and CP (Kramer et al., 2021)
V) Bcl11a+ neurons (SNc) projecting to MedCP or TailCP, with minimal projections to other CP subregions (Tolve et al., 2021)
W) Bcl11a+ neurons (VTA) projecting to LS, OT, or NAcLatS, but not to NAcMedS, NAcC, AMY, LHb, or mPFC (Tolve et al., 2021)

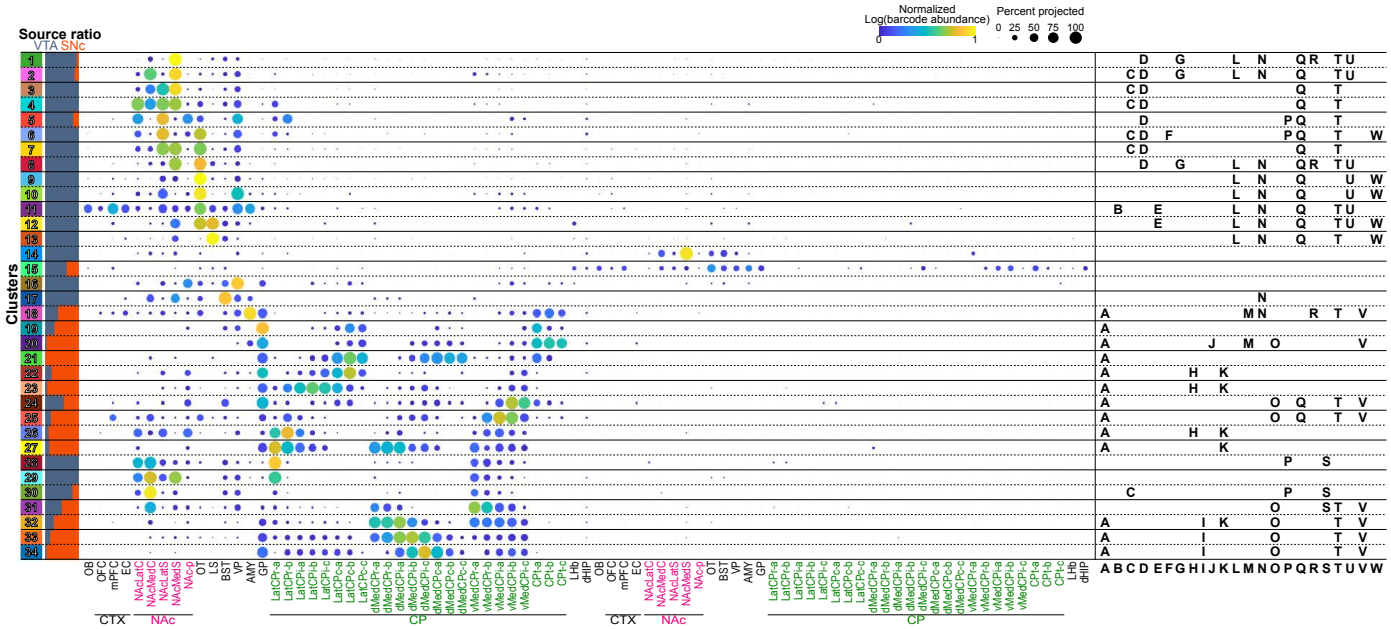

Figure S6. Comparison of POINTseq-defined clusters with previously reported VTA and SNc DA neuron populations.

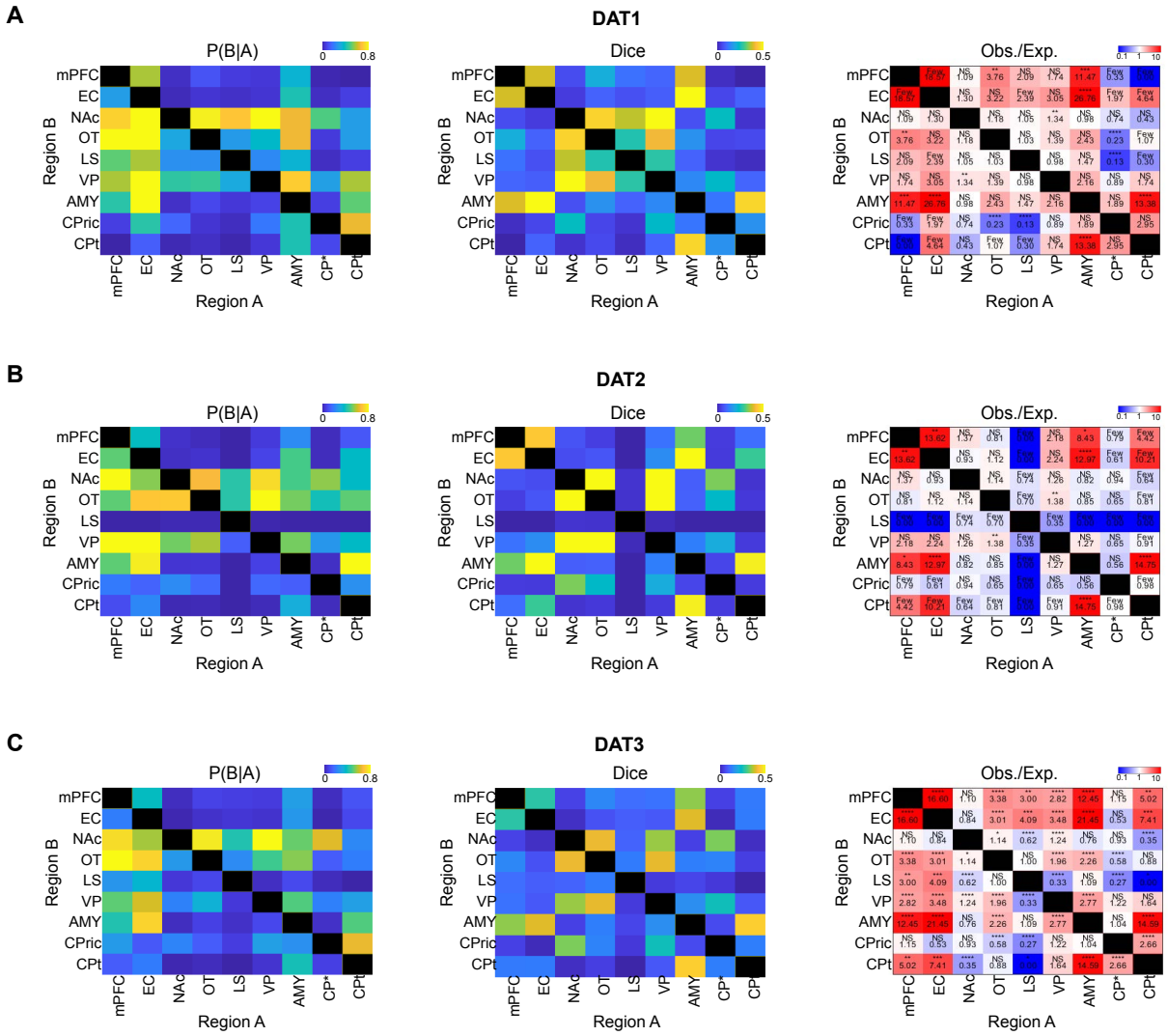

Figure S7. Co-innervation analysis of Figure 4 performed separately for individual mice.
(A–C) Conditional probability, Dice score, and over- or under-representation analyses for individual DAT-Cre mice: mouse 1 (A), mouse 2 (B), and mouse 3 (C). All three show patterns consistent with the tendencies observed in Figure 4. For over- or under-representation, binomial test with Bonferroni correction was applied (∗p < 0.05, ∗∗p < 0.01, ∗∗p < 0.001, ∗∗∗∗p < 0.0001, NS: non-significant).

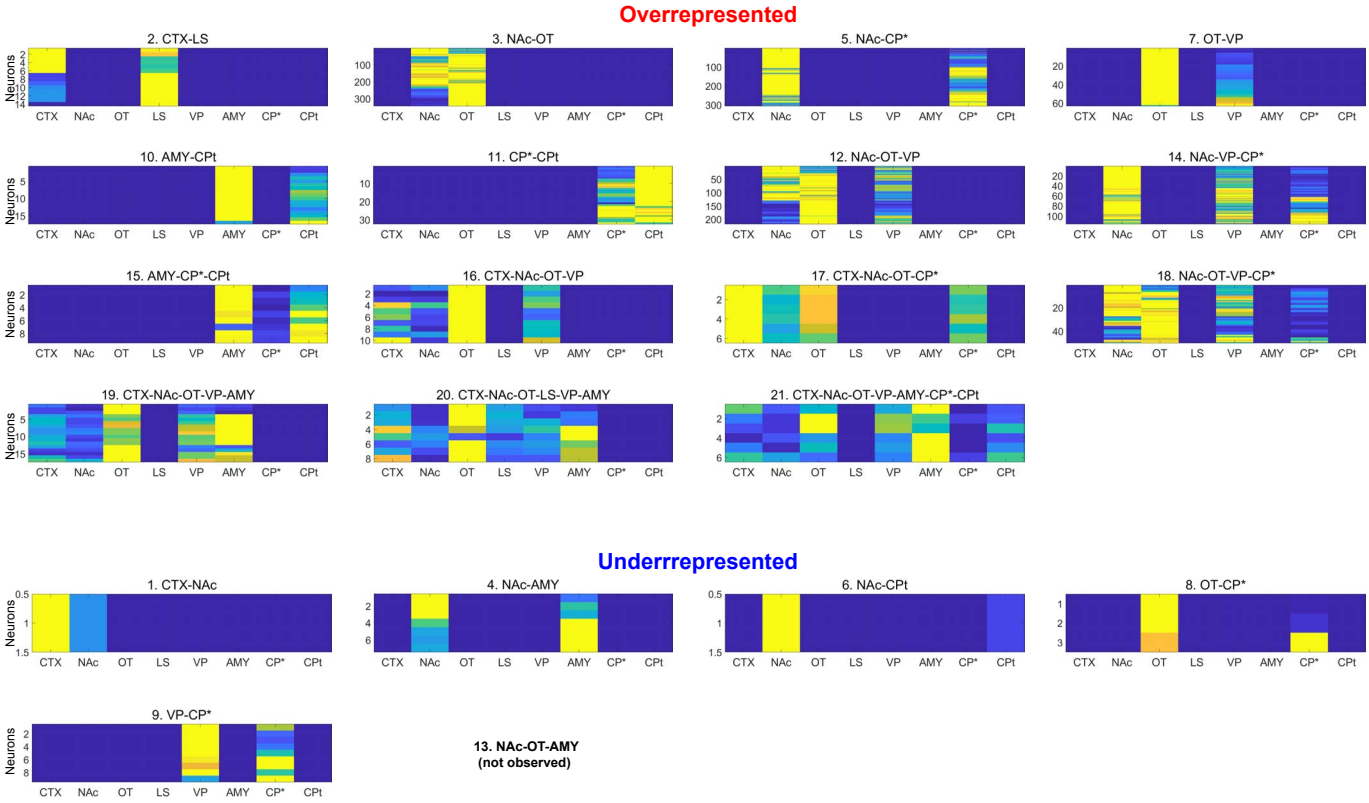

Figure S8. Quantification of projection strengths of individual neurons that constitute the significantly over- or under-represented motifs shown in Figure 4H.

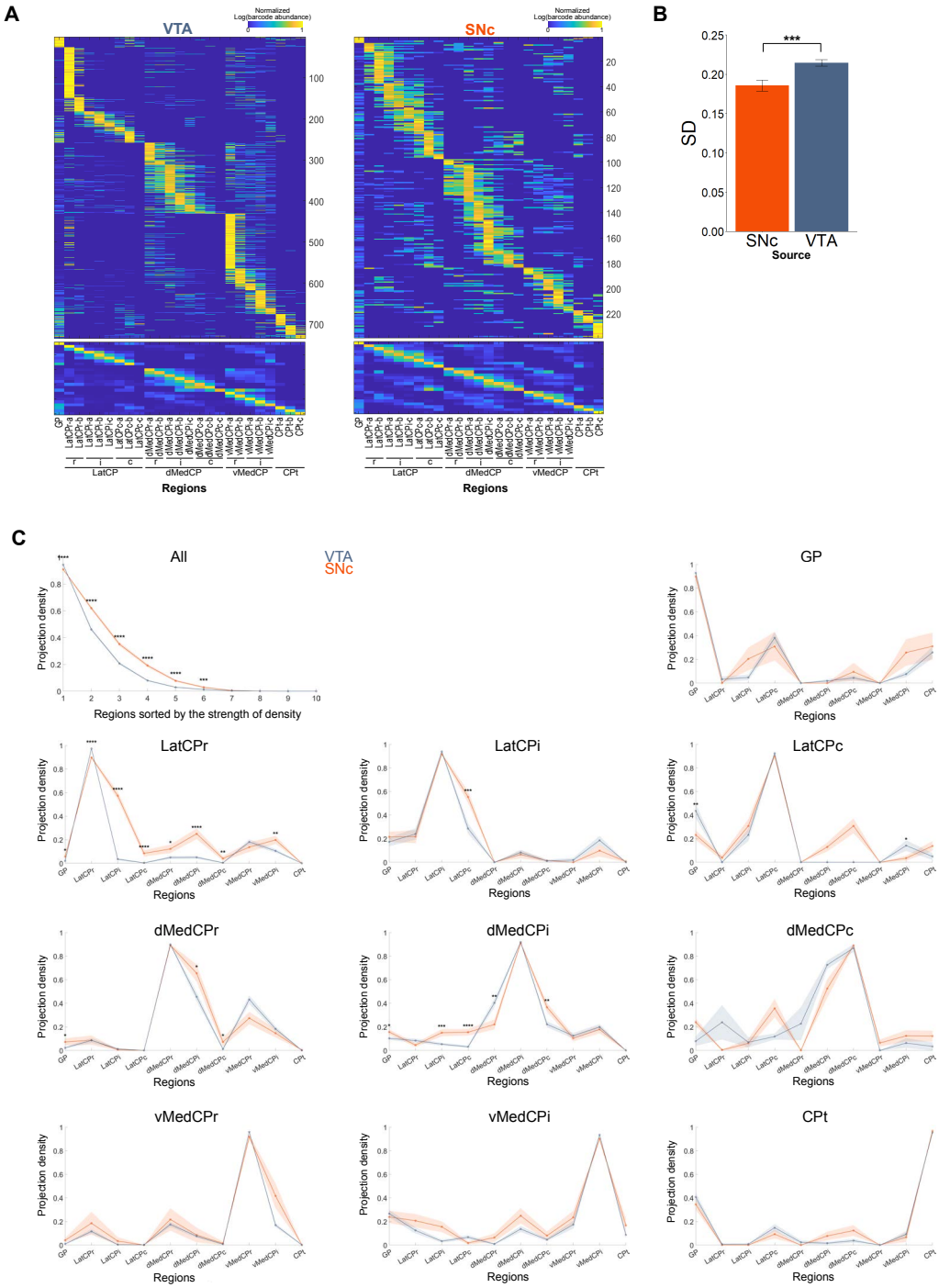

Figure S9. SNc neurons display broader and evener projection strength than VTA neurons.

(A) Projection densities (projection strength normalized by region size) were calculated for each neuron (top) and averaged density values grouped by the region of maximal projection density were plotted (bottom).

(B) SNc neurons exhibited lower standard deviations of projection densities than VTA neurons, indicating more even projections across GP and CP subregions.

(C) Projection densities around each neuron's main target gradually declined in SNc neurons, particularly in the caudal direction, while VTA neurons showed sharp decreases, especially when targeting CPr subregions (two-way ANOVA, source x projection density, Bonferroni post-hoc test, $*p < 0.05$, $**p < 0.01$, $***p < 0.001$, $****p < 0.0001$).

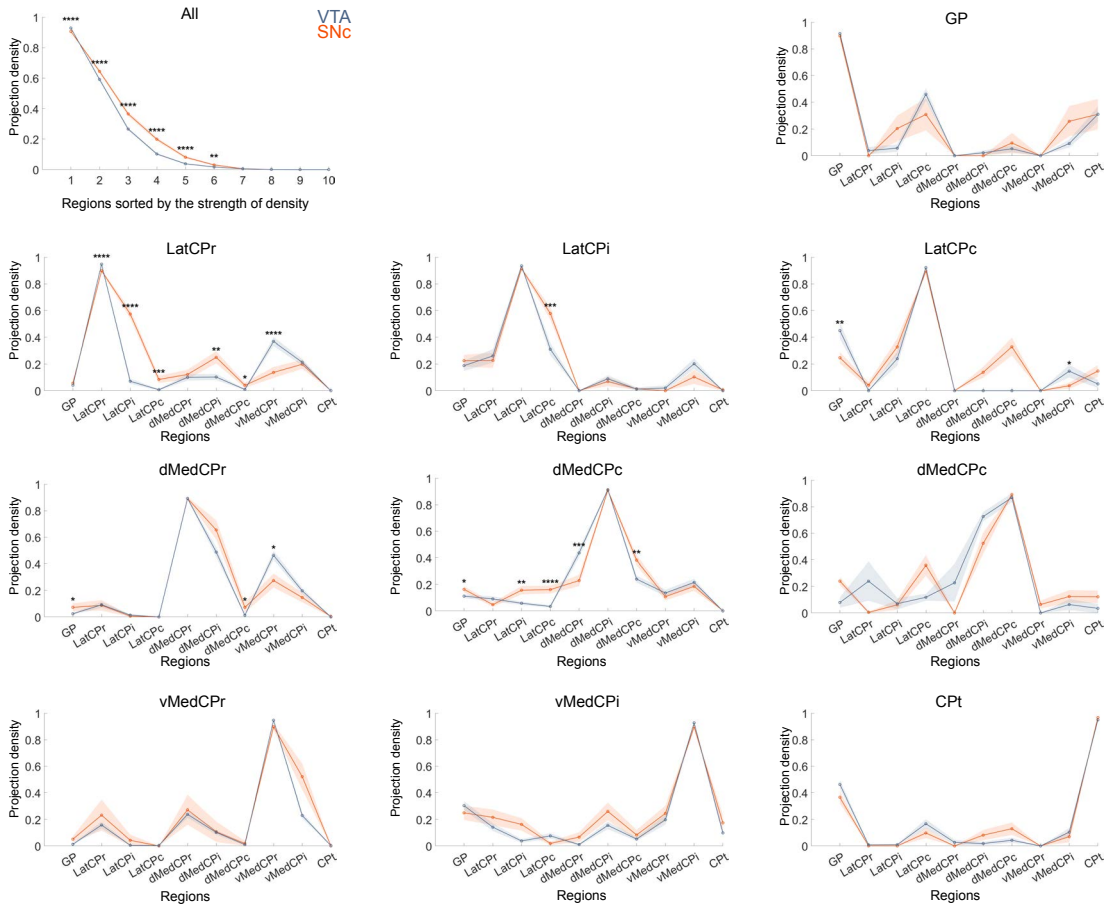

Figure S10. Neurons projecting to at least two targets show similar projection strength patterns as in Figure S9.

Differences in projection density distribution between SNc and VTA neurons remained consistent when restricting the analysis to neurons projecting to at least two regions (two-way ANOVA, source x projection density, Bonferroni post-hoc test, $*p < 0.05$, $**p < 0.01$, $***p < 0.001$, $****p < 0.0001$).

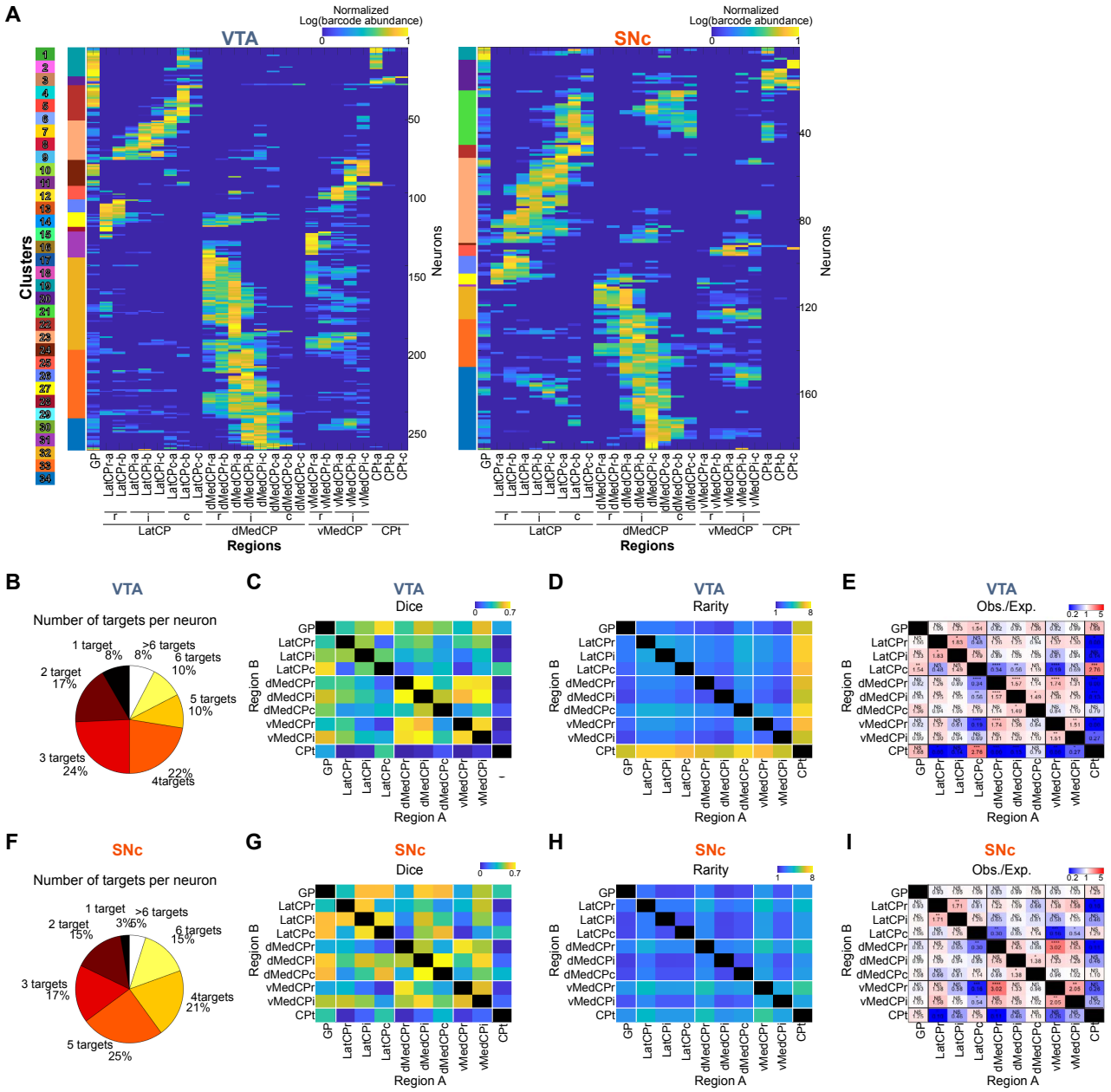

Figure S11. Among neurons exclusively projecting to the GP and CP, SNc neurons still exhibit broader projection patterns, while rarity scores become comparable between SNc and VTA neurons.

(A) Projection matrices of neurons exclusively projecting to the GP and CP, filtered from Figure 5A (276 VTA neurons, 185 SNc neurons).

(B–C, F–G) VTA neurons exhibited fewer projection targets and lower co-innervation abundance than SNc neurons, although the differences were reduced compared to the full dataset.

(D, H) Rarity scores of VTA neuron co-innervations were generally reduced under this filter, except for CPt-involving combinations.

(E, I) Most co-innervations of VTA and SNc neurons became similarly explained by the random binomial model (binomial test with Bonferroni correction, $*p < 0.05$, $**p < 0.01$, $**p < 0.001$, $****p < 0.0001$, NS: non-significant).

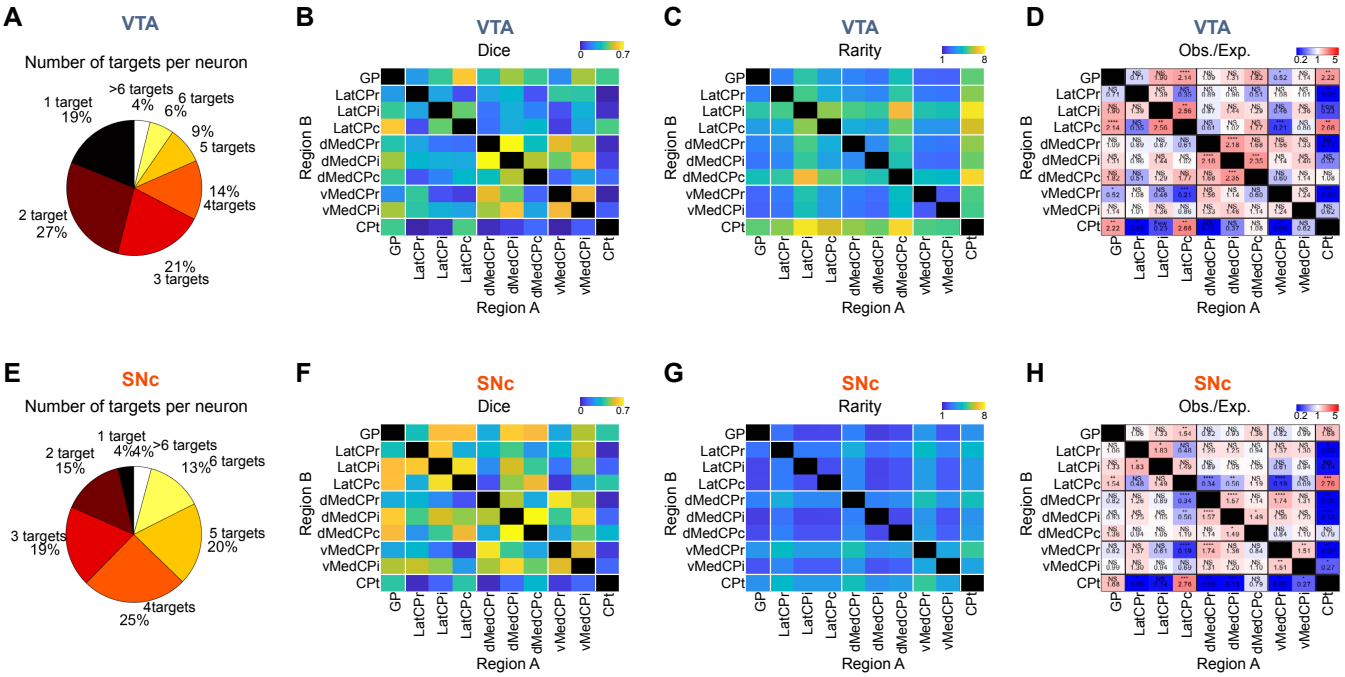

(from Fig. 5B, 5H-5J)

Figure S12. Number of targets and co-innervation analysis of Figure 5, performed with subsampled neurons of VTA matching the number of SNc neurons.

(A-H) The results of number of targets (A, E), Dice score (B, F), rarity score (C, G), and over- or under-representation (D, H) remain similar to those of Figure 5. For over- or under-representation, binomial test with Bonferroni correction was applied (∗p < 0.05, ∗∗p < 0.01, ∗∗p < 0.001, ∗∗∗∗p < 0.0001, NS: non-significant).

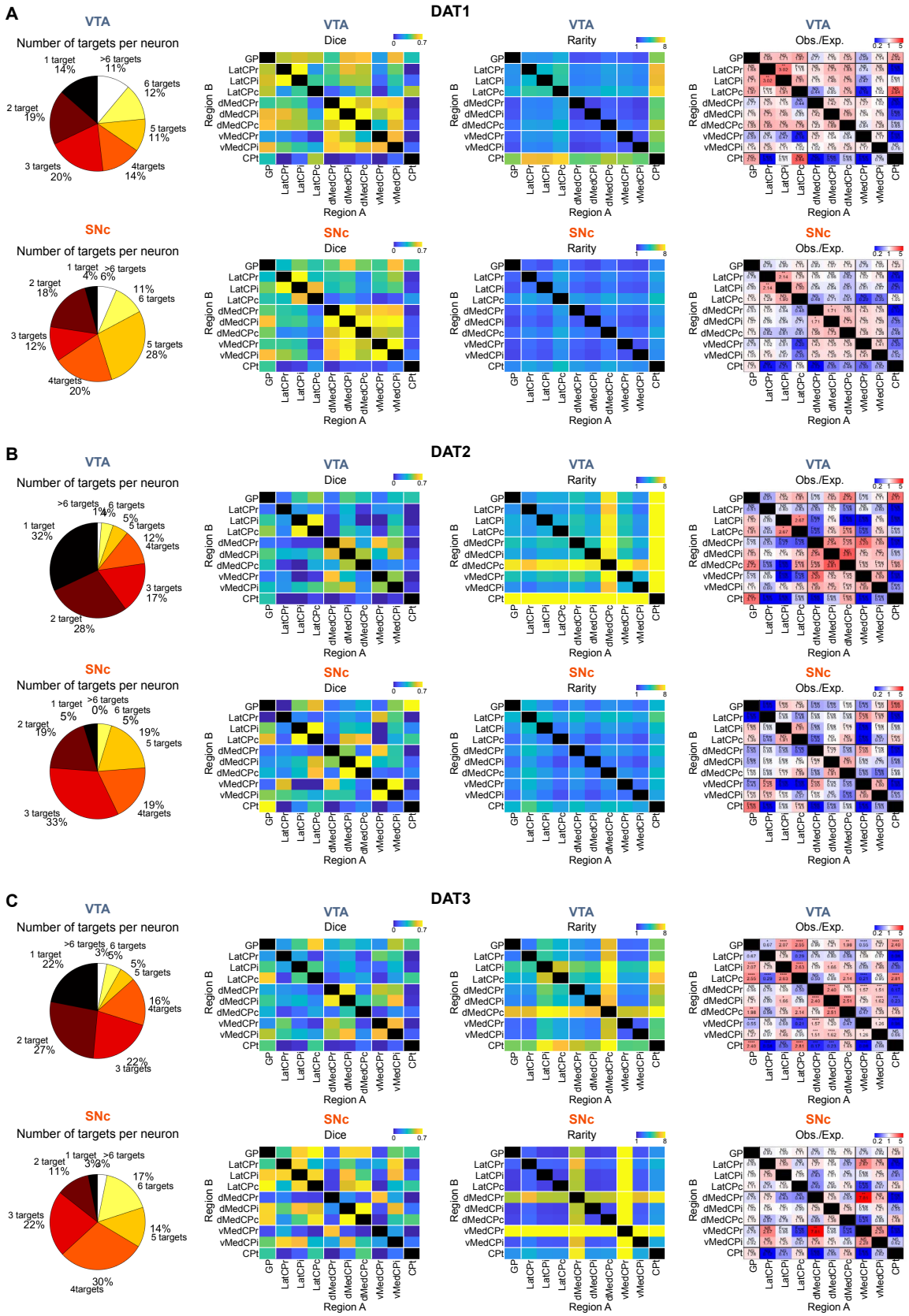

Figure S13. Number of targets and results of the co-innervation analysis performed separately for individual mice using the same methods as in Figure 5.

(A–C) Number of targets per neuron, Dice score, rarity score, and over- or under-representation analyses for

individual DAT-Cre mice: mouse 1 (A), mouse 2 (B), and mouse 3 (C). Despite high rarity of SNc neurons of the third mouse in the MedCPr regions, all three hold the tendencies observed in Figure 5. Binomial test with Bonferroni correction, $*p < 0.05$, $**p < 0.01$, $**p < 0.001$, $****p < 0.0001$, NS: non-significant.

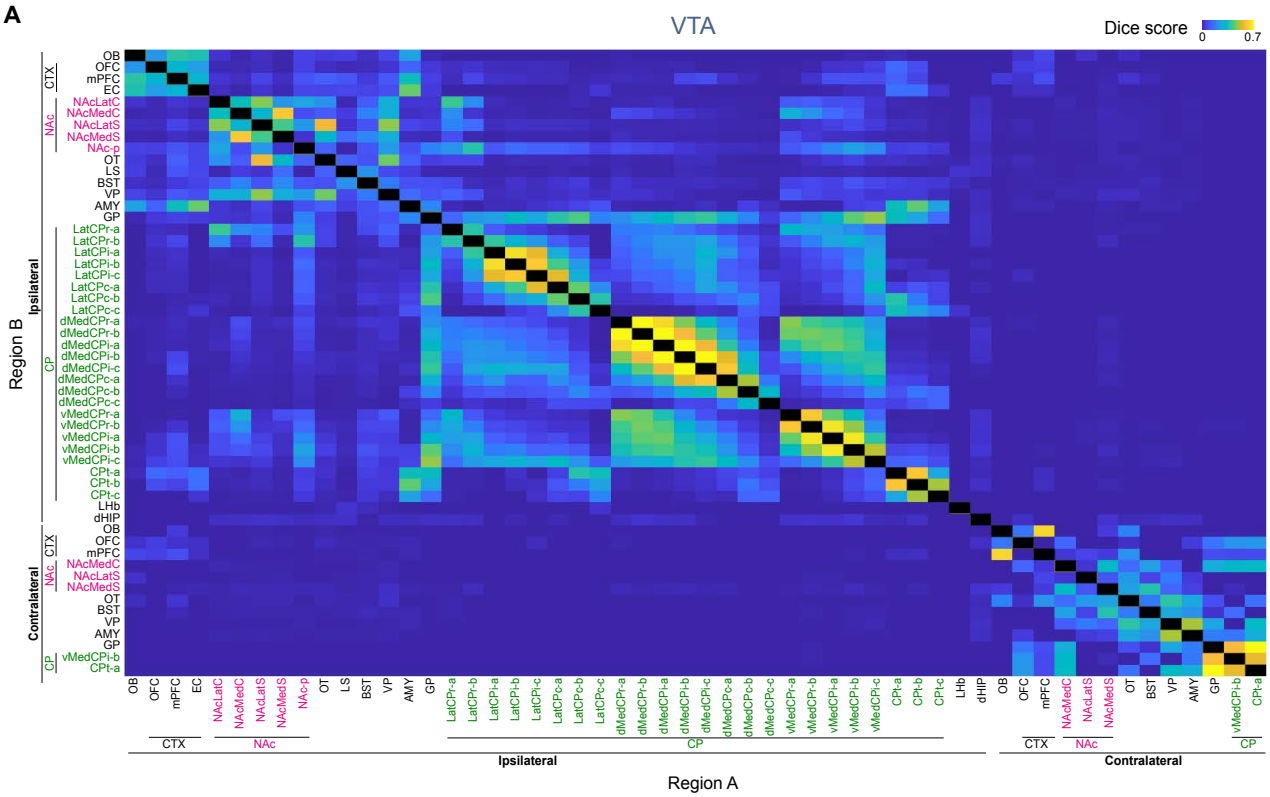

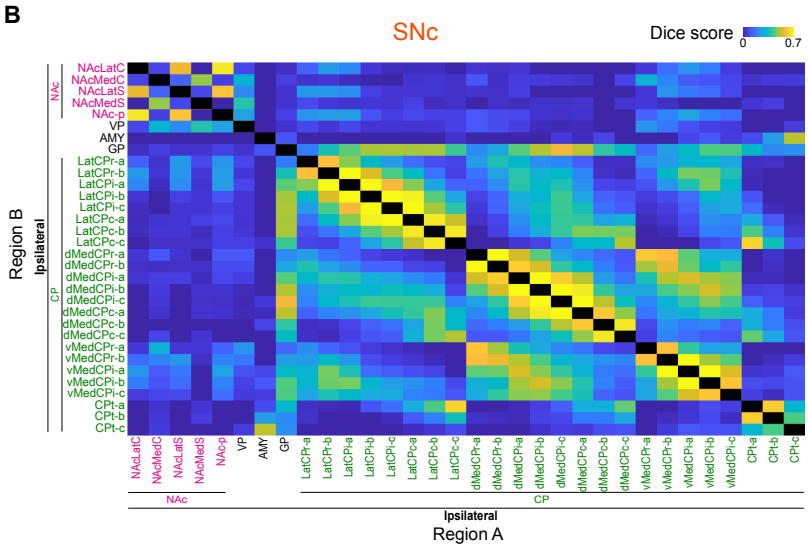

Figure S14. Co-innervation analysis using Dice scores at maximal regional resolution.
(A) Dice scores of VTA DA neurons across 41 ipsilateral and 13 contralateral target regions.
(B) Dice scores of SNc DA neurons across 32 ipsilateral target regions.

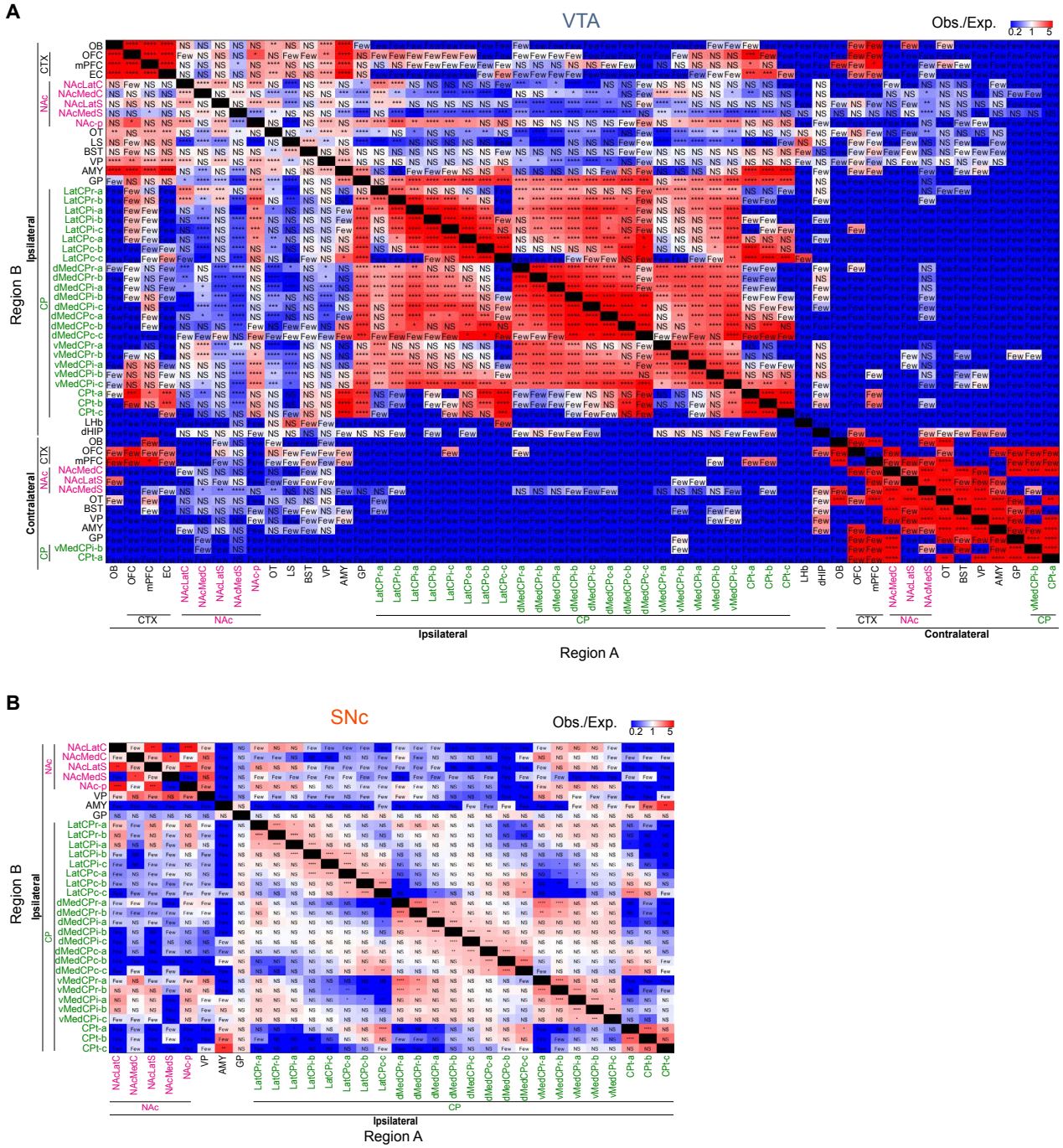

Figure S15. Over- or under-represented co-innervations at maximal regional resolution.

(A) Over- or under-represented co-innervations of VTA neurons across 41 ipsilateral and 13 contralateral regions. "Few" indicates the maximum of observed and expected neurons for this combination was fewer than 5.

(B) Over- or under-represented co-innervations of SNc neurons across 32 ipsilateral regions (binomial test with Bonferroni correction, $*p < 0.05$, $**p < 0.01$, $**p < 0.001$, $****p < 0.0001$, NS: non-significant).

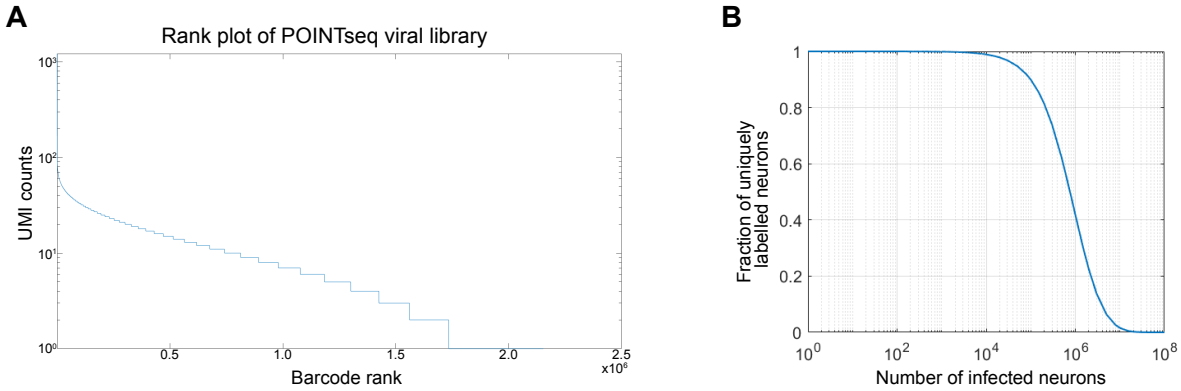

Figure S16. Diversity of POINTseq virus

(A) Rank plot of the POINTseq viral barcode library by UMI counts, consisting of 2.2×10^6 unique barcodes. (B) Estimated fraction of uniquely labeled neurons based on the filtered barcode distribution, excluding barcodes with fewer than 3 UMI counts.

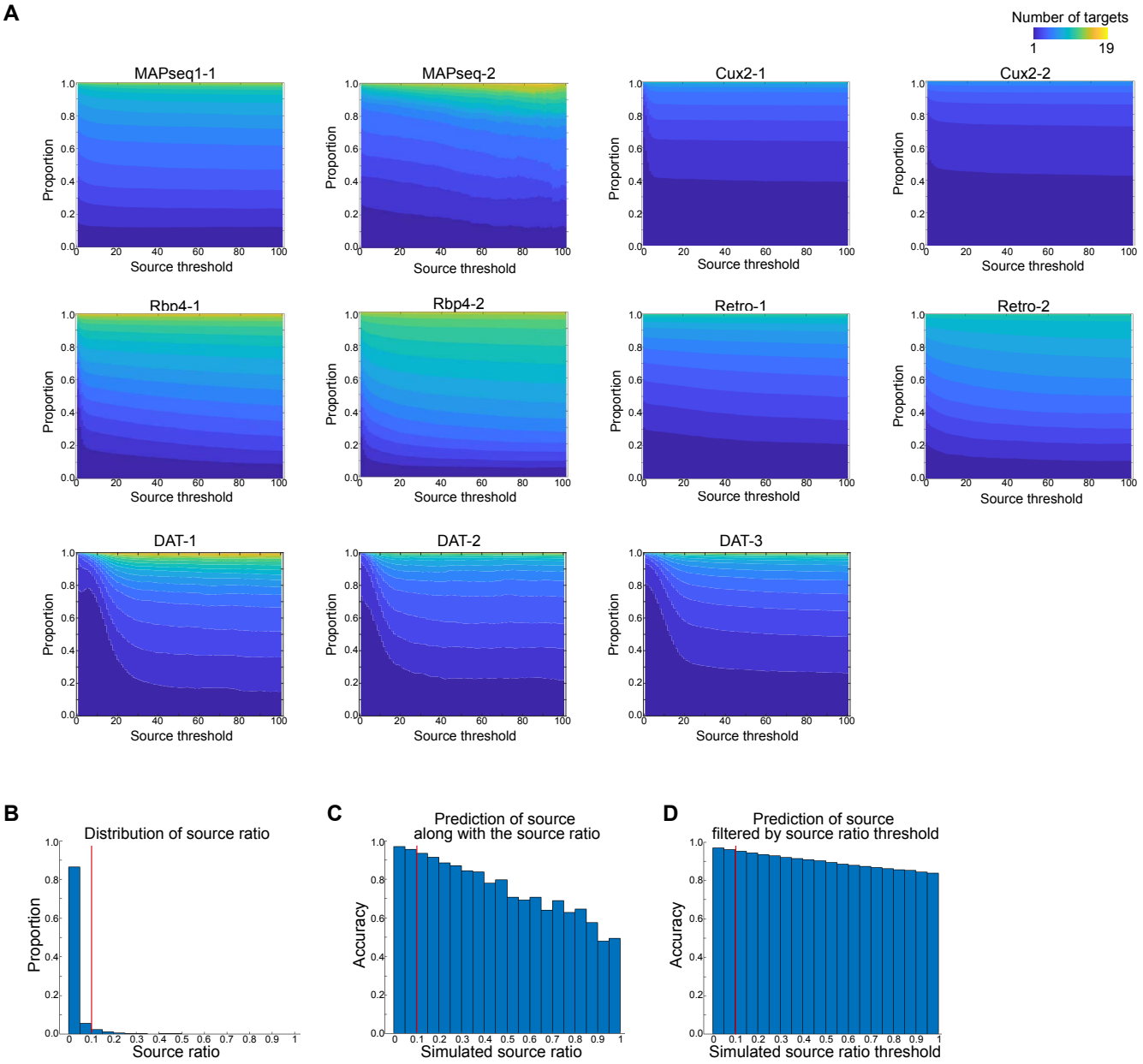

Figure S17. Determination of source parameters.

(A) Proportion of number of targets per neurons according to varying source UMI thresholds. MAPseq-1 and MAPseq-2 mice were adapted from a previous published data.[62] The number of targets stabilize beyond a specific range.

(B-D) Parameters related to source determination between VTA and SNc.

(B) Distribution of source ratios (lower UMI/higher UMI between VTA and SNc).

(C) Accuracy of source prediction across source ratio bins, estimated by simulations from a model consisting of true source and false source.

(D) Accuracy of source prediction in the simulations filtered by varying source thresholds.

Bin width is 0.05 and the red line indicates the chosen threshold (0.1) for source ratio.

Table S1. Abbreviations of brain regions.

Injection	Major domain	Abbreviation	Full description
MOp	Isocortex	MOs-r	Secondary motor cortex, rostral
		SS	Supplementary somatosensory cortex
		MOp	Primary motor area
	Striatum	STR-r	Striatum, rostral
		STR-i	Striatum, intermediate
		STR-c	Striatum, caudal
	Thalamus	TH-mr	Thalamus, medial, rostral
		TH-lr	Thalamus, lateral, rostral
		TH-mc	Thalamus, medial, caudal
		TH-lc	Thalamus, lateral, caudal
	Midbrain	MRN	Midbrain reticular nucleus
		SC	Superior colliculus
	Hindbrain	PG	Pontine gray
		MY-l	Medulla, lateral
		MY-m	Medulla, medial
VTA/SNc	Olfactory areas	OB	Olfactory bulb
	Isocortex	OFC	Orbital area
		mPFC	Medial prefrontal area
		EC	Entorhinal area
	Striatum	NAcLatC	Nucleus accumbens core, lateral
		NAcMedC	Nucleus accumbens core, medial
		NAcLatS	Nucleus accumbens shell, lateral
		NAcMedS	Nucleus accumbens shell, medial
		NAc-p	Nucleus accumbens, posterior
		LatCP-a	Lateral CP, in CP AP axis 0-0.3 mm
		LatCP-b	Lateral CP, in CP AP axis 0.3-0.6 mm
		LatCP-c	Lateral CP, in CP AP axis 0.6-0.9 mm
		LatCP-d	Lateral CP, in CP AP axis 0.9-1.2 mm
		LatCP-e	Lateral CP, in CP AP axis 1.2-1.5 mm
		LatCP-f	Lateral CP, in CP AP axis 1.5-1.8 mm
		LatCP-g	Lateral CP, in CP AP axis 1.8-2.1 mm
		LatCP-h	Lateral CP, in CP AP axis 2.1-2.4 mm
		dMedCP-a	Dorsomedial CP, in CP AP axis 0-0.3 mm
		dMedCP-b	Dorsomedial CP, in CP AP axis 0.3-0.6 mm
		dMedCP-c	Dorsomedial CP, in CP AP axis 0.6-0.9 mm
		dMedCP-d	Dorsomedial CP, in CP AP axis 0.9-1.2 mm
		dMedCP-e	Dorsomedial CP, in CP AP axis 1.2-1.5 mm
		dMedCP-f	Dorsomedial CP, in CP AP axis 1.5-1.8 mm
		dMedCP-g	Dorsomedial CP, in CP AP axis 1.8-2.1 mm
		dMedCP-h	Dorsomedial CP, in CP AP axis 2.1-2.4 mm
		vMedCP-a	Ventromedial CP, in CP AP axis 0-0.3 mm
		vMedCP-b	Ventromedial CP, in CP AP axis 0.3-0.6 mm
		vMedCP-c	Ventromedial CP, in CP AP axis 0.6-0.9 mm
		vMedCP-d	Ventromedial CP, in CP AP axis 0.9-1.2 mm
		vMedCP-e	Ventromedial CP, in CP AP axis 1.2-1.5 mm
		CPt-a	Tail CP, in CP AP axis 2.4-2.7 mm
		CPt-b	Tail CP, in CP AP axis 2.7-3.0 mm
		CPt-c	Tail CP, in CP AP axis 3.0-3.3 mm
	Cerebral nuclei	GP	Globus pallidus
		VP	Ventral pallidum
		LS	Lateral septal nucleus
		BST	Bed nucleus of the stria terminalis
		OT	Olfactory tubercle
	Thalamus	LHb	Lateral habenula
	Hipocampal formation	dHIP	Dorsal hippocampus
	Amygdala	AMY	Amygdala
	Midbrain	SNc	Substantia nigra pars compacta
		VTA	Ventral tegmental area
		DRN	Dorsal raphe nucleus
	Hindbrain	PRNr	Pontine reticular nucleus, rostral

Ip: Ipsilateral, Con: Contralateral